RAMAN SPECTROSCOPIC STUDIES OF BONE BIOMECHANICAL FUNCTION AND DEVELOPMENT IN ANIMAL MODELS

by

Kathryn A. Dooley

A dissertation submitted in partial fulfillment
of the requirements for the degree of
Doctor of Philosophy
(Chemistry)
in The University of Michigan
2011

Doctoral Committee:

Professor Michael D. Morris, Chair
Professor Raoul Kopelman
Professor Laurie K. McCauley
Assistant Professor Kevin J. Kubarych

ACKNOWLEDGMENTS

This dissertation is the culmination of five years of research and collaboration with many talented colleagues. I am indebted to every one of you who encouraged and supported me along the way. First and foremost, I want to thank my advisor and advocate, Michael Morris. I genuinely appreciate his enthusiasm, patience, and incredible wit. His vast scientific knowledge and his willingness to share it made him an excellent mentor. He was also generous in allowing me to attend numerous conferences. Working in his lab was truly an enjoyable experience!

I want to express my gratitude to my committee members: Raoul Kopelman, Kevin Kubarych, and Laurie McCauley. Thank you for your time and your suggestions which enabled me to improve my thesis. I also want to thank my lab mates for their friendship—work is so much better when you enjoy the people you work with. Thanks especially to Kurt Golcuk and Matt Schulmerich for my introduction to Raman spectroscopy and data processing methods.

My research could not have been completed without specimens from collaborators. Thanks to Jordan McCormack, David Fyhrie, Peter Muir, Adriane Joo, Ophir Klein, Jeff Meganck, and Steve Goldstein for your help. Also thanks to Brad Clay, whose enthusiasm and generosity resulted in an abundance of fused silica slides and the opportunity to attend the SPIE Geometrical Optics course. I want to acknowledge Jamie

Saville and Nancy Kerner for giving me the opportunity to participate in the WISE chemistry camp each summer—I'm thankful I was a part of such a great program. I'm also grateful for funding received from NIH training grants (Cellular Biotechnology Training Program and Regenerative Sciences) and travel assistance through Rackham Graduate School, Pfizer, and Eastman Chemical Company.

To Team Analyt and the Killajoules: I have so many great memories with all of you! You don't know how overjoyed I was when, during the first week of grad school, I found people who liked playing board games! From game nights to softball, you made the whole grad school experience a lot of fun.

Finally, I'm incredibly grateful to my family for their support, encouragement, humor, love, and confidence in me. I love you all!

TABLE OF CONTENTS

ACKNOWLEDGMENTS ii

LIST OF FIGURES viii

LIST OF TABLES x

LIST OF APPENDICES xi

ABSTRACT xii

CHAPTER I - INTRODUCTION TO RAMAN SPECTROSCOPY OF BONE 1

1 Dissertation overview 1

2 Composition, structure, and function of bone 2

3 Investigation of bone composition and chemical structure 11

4 Raman spectroscopy 13

5 Raman spectroscopy of bone 15

CHAPTER II - RAMAN MICROSPECTROSCOPIC IMAGING OF EQUINE BONE 39

1 Chapter overview 39

2 Stress mapping of undamaged, strained, and failed regions of bone using Raman spectroscopy 40

2.1 Introduction 40

2.2 Materials and methods 42

2.3 Results 45
2.4 Discussion 48
2.5 Conclusion 54
3 Composition mapping in model for extreme athlete 55
3.1 Introduction 55
3.2 Materials and methods 58
3.3 Results 61
3.4 Discussion 62
3.5 Conclusion 64
4 Chapter summary 64
CHAPTER III – THE ROLE OF SPROUTY2 ON BONE COMPOSITION IN NORMAL BONE DEVELOPMENT 83
1 Introduction 83
2 Materials and methods 85
3 Results 87
4 Discussion 89
5 Conclusion 92
CHAPTER IV – COMPARISON OF MOLECULAR ORIENTATION IN FEMORAL CORTICAL BONE FROM WILD-TYPE AND BRITTLE MICE USING POLARIZED RAMAN SPECTROSCOPY 100
1 Introduction 100
2 Materials and methods 103
3 Results 107

4 Discussion....108
5 Conclusion....111
CHAPTER V - FIBER-OPTIC RAMAN SPECTROSCOPIC PROBES AND SOFTWARE....122
1 Chapter overview....122
2 Improvements in transcutaneous bone Raman spectroscopy....122
2.1 Introduction....122
2.2 Materials and methods....125
2.3 Results....130
2.4 Discussion....131
2.5 Conclusion....133
3 Mathematical correction for coupling errors in fiber-optic spectroscopy....134
3.1 Introduction....134
3.2 Materials and methods....136
3.3 Results....139
3.4 Discussion....141
3.5 Conclusion....144
4 Chapter summary....144
CHAPTER VI - CONCLUSIONS....160
APPENDICES....164
Matlab Processing Code....164
Matlab Code for 3-D Plots....175

List of Publications 177

LIST OF FIGURES

Figure 1.1	Hierarchical structure of bone	21
Figure 1.2	Structure of an unmineralized collagen fibril	22
Figure 1.3	Mineralization of a collagen fibril	23
Figure 1.4	Energy level diagram	24
Figure 1.5	Diagnostic window	25
Figure 1.6	Representative Raman spectrum of bone	26
Figure 2.1	Double-notch specimens	66
Figure 2.2	Representative Raman bone spectrum and phosphate center of gravity	67
Figure 2.3	Raman images of stress for specimen 1	68
Figure 2.4	Raman images of stress for specimen 2	69
Figure 2.5	Raman images of stress for specimen 3	70
Figure 2.6	Stress profile generated from a finite element model of the double-notch four-point bending specimen	71
Figure 2.7	Irregular fracture process	72
Figure 2.8	Subchondral bone slice through distal end of Mc-III joint	73
Figure 2.9	Overall averages of band ratios for the racehorse and nonathletic specimens	74
Figure 2.10	Amide III spectral region and corresponding second derivative	75
Figure 3.1	Cross-section of left tibia	93

Figure 3.2	Overall group differences between Spry2$^{-/-}$ and WT mice	94
Figure 3.3	Raman spectra of Spry2$^{-/-}$ and WT mice	95
Figure 3.4	Group differences (Spry2$^{-/-}$ vs. WT) at mid-cortex	96
Figure 4.1	Orientation of amide I carbonyl bonds	113
Figure 4.2	Raman microprobe used for polarization measurements	114
Figure 4.3	Average phosphate ν_1 depolarization ratio for all specimens	115
Figure 4.4	Average phosphate ν_1 depolarization ratio for 13-week-old specimens	116
Figure 4.5	Average amide I depolarization ratio for all specimens	117
Figure 5.1	SORS model	146
Figure 5.2	Experimental apparatus for SORS measurements	147
Figure 5.3	Transcutaneous Raman spectra of canine tibia	148
Figure 5.4	Comparison of three probe geometries for transcutaneous murine measurements	149
Figure 5.5	Fiber coupling	150
Figure 5.6	Extent of overlap	151
Figure 5.7	Method comparison	152
Figure 5.8	Teflon fiber 20	153
Figure 5.9	Teflon fiber 35	154
Figure 5.10	Least squares discrepancy	155

LIST OF TABLES

Table 2.1	Average stress values and standard deviations for all regions of double-notch specimens	76
Table 2.2	Average height ratios and standard deviations for all regions of racehorse and nonathletic specimens	77
Table 4.1	Average depolarization ratios for WT and Brtl specimens	118

LIST OF APPENDICES

Appendix I	Matlab Processing Code	164
Appendix II	Matlab Code for 3-D Plots	175
Appendix III	List of Publications	177

ABSTRACT

RAMAN SPECTROSCOPIC STUDIES OF BONE BIOMECHANICAL FUNCTION AND DEVELOPMENT IN ANIMAL MODELS

by

Kathryn A. Dooley

Chair: Michael D. Morris

Raman spectroscopy is a versatile technique for studying multiple aspects of bone health. Raman bands are sensitive to the composition and structural orientation of the material and to external mechanical forces. Through examination of bone tissue from various animal models, this dissertation demonstrates the ability of Raman spectroscopy to advance knowledge of bone biomechanical function and normal bone development. Stress was measured in an equine model for the early stages of bone fracture by analyzing band shifts in phosphate ν_1, the most prominent mineral band in bone. Stresses were significantly higher in strained and failed regions than in control regions, and the pattern of stresses as calculated with Raman imaging was in agreement with the predicted stresses from a linear finite element analysis model of the fracture specimen. In an equine model for an extreme athlete, the third metacarpal bone from a racehorse was found to have an increased mineral-to-matrix ratio, an indicator of tissue mineralization,

compared to a specimen from a nonathletic horse. Raman spectroscopy was also applied to evaluate bone tissue from genetically-modified mice in which the Sprouty2 gene, a gene which regulates normal bone development, was deleted. Based on observed differences in the collagen cross-link and mineral-to-matrix band ratios, Spry2 appears to regulate cross-link formation and accrual of mineral during normal bone development. Another genetically-modified mouse examined was the Brittle mouse, a model for osteogenesis imperfecta type IV. In this model, an amino acid point substitution prevents proper folding of the collagen triple helix. Polarized Raman spectroscopy was used to assess the orientations of bone mineral and collagen fibrils in Brittle and wild-type mice. Surprisingly, no significant differences between genotypes were detected. Finally, improvements to ex vivo, through-the-skin bone measurements on animal tissue are presented, along with an experimental study detailing the improvements to fiber spectra obtained by applying software corrections to coupling errors that arise in collection with fiber bundles.

CHAPTER I

INTRODUCTION TO RAMAN SPECTROSCOPY OF BONE

1 Dissertation overview

The ability to use Raman spectroscopy on intact, fresh tissue is a big advantage. Raman spectra can be recorded on bones from different animal models, providing compositional and structural information about adaptations to bone diseases, mechanical stimuli, and pharmaceutical interventions. In this dissertation, the majority of the work has focused on examining bone tissue from various animal models in order to understand normal bone development and biomechanical function.

Background information about bone structure and function and an introduction to Raman spectroscopy and its application to bone will be presented in **Chapter I**. **Chapter II** discusses two animal models, one which is a model for the early stages of bone fracture and the other which is a model for an extreme athlete, and the insight that Raman microspectroscopic imaging can provide. Raman images have been used to map stress distributions in the bone fracture model and various composition parameters in the athlete model. Raman spectroscopy has been applied to genetically-modified mice in Chapters III and IV. In **Chapter III**, we studied mice in which the Sprouty2 gene, a gene which regulates normal bone development, was deleted. Composition differences between this

loss-of-function model and wild-type mice were examined. Brittle (Brtl) mouse studies are outlined in **Chapter IV**. The collagen in the Brtl mouse model is disordered, and so polarized Raman measurements were implemented to obtain orientation information about the mineral and collagen components of bone in this model. Finally, research using our fiber-based Raman systems, in which light is directed to and from the specimen with fiber-optic cables rather than through a microscope, is addressed in **Chapter V**. Improvements to ex vivo, through-the-skin bone measurements on animal tissue is presented, along with an experimental study detailing the improvements to fiber spectra obtained by applying software corrections to coupling errors that arise when collecting with fiber bundles. **Chapter VI** will provide an overall summary and future directions of this research.

2 Composition, structure, and function of bone

All humans rely on their bones to transmit forces from one part of the body to another[1, 2] during activities such as exercise, stretching, lifting objects, and rolling over in bed. We also depend upon the skeletal system to protect vital organs from potentially damaging mechanical forces. Hence, the primary function of bone is to sustain these loads without too much deformation.[3, 4] The unique composition and structure of bone is essential for this function, and together they provide bone with its mechanical integrity.

2.1 Composition

Bone is a complex composite material consisting of an inorganic mineral that resembles hydroxyapatite, an organic component which is predominately type I collagen,

and water. The weight percent of inorganic mineral is ~65%, while the organic content is ~25% and water is the remaining 10%.[5] Bone mineral is a carbonated hydroxyapatite. The unit cell of pure hydroxyapatite contains $Ca_{10}(PO_4)_6(OH)_2$, but in bone various ionic substitutions take place,[5, 6] including the common substitution of carbonate (CO_3^{2-}) for phosphate (PO_4^{3-}).[7] Bone mineral contains about 5-7% carbonate.[8] The organic component, also known as the matrix, is approximately 90% type I collagen and 10% noncollagenous proteins including osteocalcin, osteonectin, bone sialoprotein, serum proteins, and proteoglycans. The function of all noncollagenous proteins is not entirely known, although most are likely involved in the initiation and control of the mineralization process.[9] The repeating amino-acid sequence of collagens is glycine-X-Y, where X and Y can be any amino acid, but about a third of the total are proline and hydroxyproline.[10] Lysine and hydroxylysine residues are also common and play an important role in collagen cross-linking.[11]

2.2 Structure

Bone has a hierarchical structure[12] as outlined in Figure 1.1. On a microscopic to macroscopic scale, various types of organization exist for different bones and different species. For example, cows grow quickly and their bone structure is more disorganized.[3] In this section, the hierarchical structure of the femur will be outlined, as it is the most commonly studied long bone and one frequently examined in this lab.

In order to understand bone structure on the nanoscale, it is important to understand the structure of type I collagen, as it forms the organic framework of bones. A type I collagen molecule consists of three polypeptide chains. The amino acid sequence of two of the chains, called α1(I), are identical and the sequence of the third

chain, called α2(I), is different. The triplet-repeating regions of the chains fold together to form a triple helix, which is a predominant structural feature of all types of collagen.[13] Glycine at every third residue position is essential for triple-helix formation because it is the only amino acid without a side chain. Glycine can fit in the center of the triple helix, while the side chains of other amino acids are directed outwards.[10] Proline stabilizes the triple helix because its ring structure prevents rotation about the peptide bond [-C(=O)NH-] and hydroxyproline can stabilize the triple helix through inductive effects of its OH-group.[13, 14]

A collagen molecule is about 300 nm long and 1.5 nm in diameter, and is the basic building block for the larger collagen fibril.[15] The fibril diameter is ~50 nm in the rat femur[16] but varies with anatomical site and species.[17] During fibrillogenesis, collagen molecules arrange themselves in a staggered parallel array.[18] A gap zone exists (~40 nm) between the end of one collagen molecule and the beginning of the next, and collagen molecules in adjacent rows are staggered by 67 nm, as shown in Figure 1.2. Thus, the end regions of the molecules overlap and these sites are where enzymatic cross-linking occurs.[15, 19] Lysyl oxidase is an enzyme that deaminates lysine and hydroxylysine residues in the telopeptide regions of the collagen molecule, which are the non-helical regions at both ends of the molecule. Deamination forms an aldehyde [-C(=O)H] group. The aldehydes react with opposing amine groups ($-NH_2$) from lysine or hydroxylysine residues of adjacent molecules to form intrafibril cross-links.[20-22] These cross-links, also known as immature or divalent because the cross-links connect two collagen molecules within the same fibril, are reducible. Over time they mature into trivalent, non-reducible

cross-links, forming a cyclic ring system that links a third collagen molecule from a different fibril. The resulting trivalent, interfibril cross-links are more stable.[22]

On a nanoscopic scale, collagen molecules and fibrils form the structural framework into which the mineral is deposited. Landis and colleagues[23, 24] visualized bone and tendon mineral using electron microscopy and showed that mineral was initially deposited both within the gap zones of the collagen fibril and also in the overlap regions of the fibrils. The mineral crystal has a plate-like shape.[23-25] The size of bone mineral crystals is approximately 57 x 27 x 7 nm.[26] Their length and width can vary somewhat,[15, 26-28] but their thickness is more uniform (~2 – 10 nm). As the mineral grows, it can fuse with nearby crystals and form platelets that stack parallel to one another within the collagen fibril (see Figure 1.3). The longest dimension of the crystals (same as the c-axis in carbonated apatites) is aligned along the long axis of the collagen fibrils.[23-25, 29]

On a microscopic scale, the mineralized collagen fibrils are arranged parallel to each other to form collagen fibers[30] that are ~1-10 μm in diameter.[31] These fibers then arrange in layers known as lamellae. Each lamella is ~3-7 μm thick.[32] The classical view is that collagen fibers are oriented in one direction within an individual lamella, although it is more likely that multiple domains exist within a lamella and the orientation is the same within a domain.[4] Subsequent arrangement of lamellae into higher order structures depends on bone type.[33] In the tibia and femur, individual lamella make up the structure of osteons. An osteon is formed when a blood vessel gets incorporated into the bone and lamellae center themselves around the blood vessel, forming circular layers. An osteon is 200-250 μm in diameter and runs approximately parallel to the long axis of the bone.[32] Different lamellar structures have been found in osteons, including alternating lamellae

where collagen fibers in one layer were at right angles to the collagen fibers in the next layer.[34] In the same study, lamellae with a "twisted plywood" structure were observed, meaning the collagen fibers in a layer were offset at an angle from the previous layer. Ascenzi and Bonucci[35] used polarized light to study lamellar structures they termed circumferential, longitudinal, and alternating.

On the macroscopic scale, bone is classified into two types: cancellous bone and cortical bone. Cancellous or trabecular bone has a porosity between 75-95% and consists of an interconnected system of plates and struts that are about 200 μm thick. Cancellous bone is found in the ends of long bones like the tibia and femur. Cortical bone makes up the surface of bones and forms a shell about 1-5 mm thick around cancellous bone.[36] It is dense, with only ~5-10% porosity.[3] Osteonal units are found in cortical bone but not usually in cancellous bone because they usually don't fit inside an individual trabecular strut.[3]

2.3 Function

A primary function of bones is resisting deformation under load. Bone accomplishes this through the interaction of its composition, hierarchical structure, and macroscopic structural properties, including size and shape. The combination of these features allows bone to function properly under the mechanical loads it normally experiences.

2.3.1 *Mineral contribution*

The mineral in bone provides tensile strength and mechanical stiffness.[37, 38] The presence of too much mineral can make the material brittle and lead to decreased bone

toughness.[39, 40] In addition to the quantity of mineral, the mineral crystallinity, a measure of the size and stoichiometry of the crystals, is also important to the mechanical properties of bone. Yerramshetty and Akkus[41] found in human cadaveric femora under tensile loading that bone strength and stiffness increased with increasing crystallinity.

2.3.2 *Collagen contribution*

Collagen is responsible for bone toughness,[38, 40, 42, 43] which is the energy required to cause bone failure or fracture, independent of bone size or geometry.[3] Toughness can also be defined as the amount of stress necessary at a crack tip to cause crack propagation.[43] The quantity of collagen, orientation of fibers, and state of cross-linking all affect bone mechanical properties. For example, collagen denaturation by heating led to a direct decrease in bone toughness and strength but did not affect the mineral and bone stiffness.[42] A more important case is osteogenesis imperfecta (OI), a disease caused by genetic mutations in the amount or quality of type I collagen. In OI, the mechanical properties of collagen are compromised[44] and patients often have skeletal deformities and a higher fracture risk.[45]

The orientation of collagen fibers can affect the mechanical properties. In osteonal bone in which collagen fibers in adjacent lamellae were approximately oriented along the long axis of the osteon (and subsequently the long axis of the bone), bone tensile strength was enhanced.[46-48] In osteons with alternating lamellae (where collagen fibers were oriented at approximately right angles), the bone withstood higher compressive strengths.[49] In osteons with a twisted plywood lamellar structure, the anisotropy of individual lamellae was demonstrated.[50] However, the overall arrangement of the collagen fibers into the plywood structure served to create approximate isotropic

microhardness. It was hypothesized that isotropy may allow lamellar bone to better withstand a variety of mechanical forces, as opposed to just tensile or compressive loads.

The state of collagen cross-linking also affects mechanical properties. Enzymatic cross-links (those formed through the action of the enzyme lysyl oxidase) provide mechanical strength to the collagen fiber, but non-enzymatic cross-links that occur through collagen reaction with glucose can render the fiber too stiff.[22] In a study on age-related changes in bone collagenous matrix, the decreased strength and toughness of bone during aging was associated with an increase in the concentration of pentosidine, a non-enzymatic glycation cross-link.[51] It has also been suggested that intrafibrillar cross-links may be more important to bone strength and toughness than interfibrillar cross-links.[43]

2.3.3 *Water contribution*

Solid-state NMR studies have provided evidence that an ordered layer of water molecules exists on the surface of the mineral crystals in unmodified bone[52] but not in deproteinated bone,[53] suggesting that water is necessary for mechanically coupling the mineral and collagenous matrix and cushioning the bone against mechanical stress. It was also shown that water occupies vacancies created by substitutions and defects in the crystal lattice, perhaps by stabilizing the mineral structure through hydrogen bonding between surrounding ions.[53] In another NMR study, the effects of aging on water distribution in bone were correlated directly with mechanical properties. Water molecules that were bonded to collagen and mineral decreased with age and were correlated with decreased bone strength and toughness.[54] Other studies have examined

the role of water on mechanical properties and structure by using dehydrated bone specimens.[55, 56]

2.3.4 *Bone as a composite*

Although the mechanical contributions of mineral, collagen, and water have been discussed separately, bone is really a composite material whose behavior is different from the behavior of its individual components.[38] The strength and resistance to fracture of bone depends not only on the presence of these different constituents, but also on their organization and interaction with one another within bone's hierarchical structure.[40, 57-59] For example, in a mouse model for osteogenesis imperfecta (oim mouse),[60] a defect in the collagen molecules affected the size and arrangement of the mineral.[58] Electron microscopy was used to examine mineralizing tendon from the oim mouse, and images showed that the mineral crystals in this mouse were bigger and less well-aligned with respect to the collagen fibrils than in wild-type mice.

Bone strength also depends on macroscopic structural properties such as the size and geometry.[57] For example, even with decreased bone mineral density, the strength of bone can be maintained or even improved through compensatory mechanisms that increase the size and cross-sectional area of the bone.[61]

2.3.5 *Bone is a dynamic tissue*

Superficially, bone seems to be an unchanging tissue that provides structural support, but actually bone is a dynamic material that responds to metabolic activity, pharmaceutical interventions, and mechanical stimuli. The metabolic activity of bone can change with age or disease. Activity changes affect the cell-mediated processes of

bone modeling and remodeling that regulate bone formation and resorption.[62, 63] For example, a common metabolic bone disorder is osteoporosis, which occurs when the rate of bone resorption is greater than the rate of bone formation. Osteoporosis can affect the structural geometry of bones most dramatically via the thinning of trabecular struts[36, 64] and can also change the composition. Changes may include a decrease in the mineral content and an increase in the mineral crystal size.[65-68]

Pharmaceutical interventions for osteoporosis can slow or even reverse some of these changes, including macroscopic structural changes such as the thickening of trabecular bone or less dramatic bone loss.[69, 70] Drug therapy can also affect composition. Pharmaceuticals known as antiresorptive agents inhibit bone resorption and tend to cause an increase in the mineral content and crystal size.[65, 71-73] Anabolic agents promote bone formation and tend to cause a decrease in the mineral content and crystal size.[74-77]

Mechanical stimuli can also affect the structural and compositional properties of bone. For example, in athletes who play tennis, their dominant arm has a larger bone mass and area than their non-dominant arm.[78, 79] In another exercise study, mice that ran on a treadmill had greater tibial strength, but showed no increase in tibial cross-sectional size or shape. Rather, compositional changes were observed.[80, 81]

Bone is a dynamic tissue that adapts to various stimuli in order to maintain its mechanical integrity. Bone accomplishes this through changes in the amount or structure of its chemical constituents. This may affect the way the constituents associate with each other, and in turn affect the different levels of bone organization, from the nanostructure to the macrostructure. The composition of bone is one of the main research focus areas in our lab.

3 Investigation of bone composition and chemical structure

X-ray scattering, nuclear magnetic resonance spectroscopy, and infrared spectroscopy are the predominant techniques that have been utilized to study the composition and structure of bone. X-ray scattering methods provide information about the crystallographic structure of mineralized materials. Powder x-ray diffraction has been used to examine lattice imperfection (caused by ionic substitutions) of bone mineral in terms of crystal size and lattice strains.[6] Small-angle x-ray scattering (SAXS) provides information on the mineral structure in terms of average thickness, size and shape, orientation, and degree of alignment of the crystals.[82] SAXS has been used to study the thickness and alignment of mineral in human trabecular and cortical bone.[82, 83] Mineral crystals were aligned parallel to trabeculae,[82] and trabecular bone contained significantly thicker mineral crystals than cortical bone, although the cortex was more mineralized.[83] SAXS has also been employed for investigating mineralization in oim mice.[84] Mineral crystals in oim/oim mice were thinner and less well aligned when compared to their heterozygous oim/+ counterparts.

Nuclear magnetic resonance (NMR) spectroscopy is another method used to investigate bone composition and structure.[85] With ^{31}P NMR, the presence of minor phosphate components in bone mineral, specifically acid phosphate (HPO_4^{2-}), have been observed.[86, 87] Two-dimensional ^{1}H-^{31}P heteronuclear correlation NMR can detect the proton spectrum of bone mineral and substantially suppress interfering proton signals from bone matrix and water. The technique has been used to observe the presence of hydroxide ions (OH^-) in bone mineral.[88] Recently, isotropic chemical shifts in ^{43}Ca NMR were used to estimate the calcium-oxygen bond distance in bone mineral.[89]

Infrared (IR) spectroscopy is also commonly employed to study the chemical makeup of bone. Researchers using IR have studied both normal and diseased bone tissues, including osteoporotic changes to the amount and/or quality of the mineral and collagenous matrix.[65, 90-93] IR parameters that represent collagen maturity and mineral content and composition were shown to have higher values when the risk for low impact fracture was higher.[94]

Other techniques can be used to investigate bone, including gas and liquid chromatography and Raman spectroscopy. Gas chromatography has been utilized to examine the effect of dietary lipids on the fatty acid composition in jawbones of rats[95] and to correlate fatty acid composition with biomechanical properties in mouse femurs.[96] High performance liquid chromatography has been used to detect age and gender effects on the amount of enzymatic and non-enzymatic collagen cross-links in human femurs.[97] Raman spectroscopy has also been applied to bone. Raman is a vibrational spectroscopy technique like IR. IR measures light absorption whereas Raman measures light scattering, but both methods provide similar, complementary information because they both probe molecular vibrations of the sample. Raman spectroscopy has been used to detect relative composition differences in a mouse model for force-induced craniosynostosis (premature fusing of the skull).[98] It has also been employed for noninvasive measurements of bone through the skin.[99, 100]

Some of the methods listed are used to examine only one phase of the bone. For example, x-ray scattering methods are used to study the inorganic mineral content of bone, whereas chromatographic techniques are used to study the organic content of bone. On the other hand, NMR, IR, and Raman spectroscopies report on both the inorganic

mineral and organic matrix. In general, sample preparation is more tedious for NMR and IR. NMR has typically been used on powdered bone, although ongoing NMR experiments in our lab have reported spectra from intact bone specimens. With IR, water absorbs in the infrared region of the spectrum, so bone samples are typically fixed, embedded, and sliced into thin sections. Water is a weak Raman scatterer, which enables the examination of thick, fresh tissue specimens. Raman spectroscopy is an excellent tool for examining both the inorganic and organic constituents in fresh, intact bone tissue with minimal sample preparation.

4 Raman spectroscopy

Raman spectroscopy is an inelastic scattering technique in which an energy exchange between incident light and molecules in the sample induce molecular vibrations.[101-104] When light is incident on a sample, it can be transmitted, absorbed, or scattered. In the process of scattering, the oscillating electric field of the incoming excitation light causes the electron cloud of a covalent bond to oscillate and distort from its equilibrium position. In the energy level diagram of Figure 1.4, this process is represented as promotion of an electron into a virtual excited state, which is really just a distortion of the electron cloud of the bond. It can be considered to be an electronic energy level whose energy is dependent on the energy of the excitation light. This induced dipole in turn causes light to be emitted. The majority of electrons are scattered at the same energy and frequency as the incident light, called Rayleigh or elastic scattering. If instead, an energy exchange occurs between the incident photons and the sample molecules, then the frequency of the scattered light is altered from the frequency

of the incident light. This process induces molecular vibrations and is called Raman scattering. In Stokes Raman scattering, energy is transferred from the incident photon to the molecule, and the resulting scattered photon has a lower energy than the incident photon. In anti-Stokes Raman scattering, energy is transferred from the molecule to the incident photon, and the scattered photon has a higher energy than the incident photon. Anti-Stokes Raman scattering requires that molecules initially be in higher vibrational levels, which requires higher temperatures. At room temperature, Stokes Raman scattering predominates because most molecules are in the ground vibrational state. The term Raman scattering generally refers to Stokes Raman scattering, unless specified otherwise.

The difference in energy between the excitation light and scattered light corresponds to a vibrational frequency of the molecule. Each molecular species has its own set of molecular vibrations, and thus its Raman spectrum will consist of a set of characteristic bands that correspond to vibrational frequencies of that molecule. For a band to appear in the Raman spectrum, there must be a change in the polarizability of a bond when the excitation light is incident on the molecule. Polarizability is a measure of the ease of distortion of the electron cloud of a chemical bond in an external electric field. In general, this means that the vibrations of non-polar bonds produce stronger Raman intensities than polar bonds because their electron cloud is delocalized, making it more easily distorted by the incoming light. Symmetric stretches are typically more intense in Raman spectra, whereas asymmetric stretches tend to be stronger in the IR. The intensity of Raman bands is proportional to the number of molecules or ions interrogated so the technique can be used for quantitative analysis.

A Raman spectrum is typically displayed as scattered light intensity versus the change in optical frequency relative to the optical frequency of incident light. This change in frequency is called the Raman shift and is measured in wavenumbers (cm^{-1}), the reciprocal of the wavelength in centimeters. Raman shifts are independent of the excitation wavelength.[105]

Raman spectra are good molecular fingerprints and provide information about the composition of the sample simply by the presence of bands in the Raman spectrum. Raman bands are also sensitive to the local environment, and changes in peak position, intensities, and widths of those bands also report on mechanical stress, temperature, and the structure of a material, including the mineral crystallite size and protein secondary structure, as discussed in the next section.

5 Raman spectroscopy of bone

In the application of Raman spectroscopy to the study of bone (or biological specimens in general), it is important to choose a proper excitation wavelength to minimize fluorescence. Tissue fluoresces and fluorescence quantum efficiency is typically 10^6 times or more higher than the quantum efficiency of Raman scattering. Hence, fluorescence bands can easily obscure Raman bands in the sample spectrum. Working in the "diagnostic window" can mitigate this problem. The diagnostic window is a wavelength region of the electromagnetic spectrum from ~600 nm to ~1100 nm where the absorption of tissue components, including water and hemoglobin, is at a minimum (see Figure 1.5).[106, 107] In this region incident photons are not energetic enough to excite fluorescence of most molecules. The excitation wavelengths used in this

dissertation are the readily available laser diode wavelengths of 785 and 830 nm that minimize fluorescence.

A representative Raman spectrum of bone is shown in Figure 1.6. Bands of the inorganic mineral are highlighted in orange and bands of the organic matrix are highlighted in green. The most prominent bands in the bone spectrum are from the mineral, with the most intense band arising from the phosphate ν_1 symmetric stretch (P-O stretch) at ~959 cm^{-1}. The multiple crystallographic sites occupied by phosphate in the mineral lattice are all close in frequency, resulting in a band that is broader but quite intense. Other phosphate bands include the O-P-O bending modes of phosphate ν_2 and ν_4 which appear at ~432 and ~579 cm^{-1}, respectively. Another mineral band is the carbonate ν_1 symmetric stretch (C-O stretch) at 1070 cm^{-1}. Important matrix bands include the C-C stretches of proline and hydroxyproline (Pro, Hyp) at 855 and 875 cm^{-1}, which are specific to collagen, and the CH_2 scissoring mode at ~1450 cm^{-1}, which is a general marker for protein content. The vibrations of the collagen backbone include amide III (C-N stretches and N-H bends) and amide I (C=O stretch). The maxima of these bands are ~1250 cm^{-1} for amide III and ~1660 cm^{-1} for amide I.

Because the amide bands are backbone vibrations, they report on the secondary structure of collagen.[108-113] Amide I and amide III are broad envelopes whose intensity profile results from several overlapped component bands. Curve-fitting the amide region resolves the envelope into individual component bands that are correlated with a particular structural feature. For example, in IR studies of the triple-helical collagen model peptide $(Gly\text{-}Pro\text{-}Pro)_{10}$, the amide I contour was fit with three bands with peak maxima at 1629, 1645, and 1667 cm^{-1}. These bands corresponded with the C=O groups

of proline (after glycine), glycine, and proline (before glycine) residues, respectively.[114] Protein secondary structure is determined by hydrogen bonding between peptide groups,[111] and so any changes to hydrogen bonding, such as dehydration, may cause changes in the intensity and frequency of amide component bands.[115]

Four commonly used Raman metrics of bone tissue include the mineral-to-matrix ratio, the carbonate-to-phosphate ratio, the collagen cross-link ratio, and crystallinity. The first three parameters are band ratios, which can be calculated using either the heights or the areas of the bands. We have found that the height ratios often give more accurate and reliable results than area ratios because the height values are less susceptible to errors from baselining.[116]

The mineral-to-matrix ratio can be calculated as phosphate ν_1-to-amide I or phosphate ν_1-to-Pro/Hyp. The use of Pro/Hyp may give more accurate results because its stretching frequency and intensity are less sensitive to changes in the secondary structure of collagen than are the amide vibrations.[117] The mineral-to-matrix ratio is a marker for mineral content and it positively correlates with ash weight.[92, 118] Ash weight measures the degree of mineralization in the bone tissue and is obtained by heating bone to extreme temperatures (~800° C) to evaporate the water and destroy organics.[3] In general, aging is associated with an increase in mineral content,[119, 120] which is reflected as an increase in the mineral-to-matrix ratio.[121-123]

The carbonate-to-phosphate ratio is calculated as carbonate ν_1-to-phosphate ν_1. The ratio is a measure of the amount of carbonate substitution in the apatitic lattice, and has been validated by chemical measurements of the carbonate content.[124, 125] During aging, carbonate substitution typically increases in the bone mineral[126] which is reflected

in a larger carbonate-to-phosphate ratio.[122, 123, 127] Closely related to this parameter is the crystallinity, which is calculated by the spectral band width[128, 129] or inverse band width[127, 130] of the phosphate ν_1 band. It is a measure of the stoichiometric perfection of the crystal apatitic lattice and also the crystal size. Crystallinity is correlated with the amount of carbonate substitution and also with powder x-ray diffraction measurements that measure the length of the mineral crystals along their c-axis.[127, 130-132] Crystallinity increases with more perfect crystals (i.e. less substitution) and larger crystals. Carbonate substitution results in a reduction in crystallinity and has been shown to cause broadening of the phosphate ν_1 band.[124, 127, 133, 134] With aging, the crystallinity increases (as measured by a decrease in the phosphate ν_1 band width) despite increased carbonate substitution, likely because the crystals are getting longer.[135]

The collagen cross-link ratio is typically calculated using the ratio of amide I sub-bands at ~1665 and ~1685 cm^{-1}. The cross-link ratio is a measure of the maturity of the collagen fibrils and extent of mature cross-linking. These two components have been correlated with specific types of cross-links.[136] The component at 1665 cm^{-1} corresponds to pyridinoline cross-linked peptides. Pyridinoline is a mature, trivalent, non-reducible cross-link. The component at 1685 cm^{-1} corresponds to dehydrodihydroxylysinonorleucine, which is an immature, divalent, reducible cross-link. In general, the 1685 cm^{-1} component decreases with age and collagen maturity, while the 1665 cm^{-1} component increases, probably because the immature, divalent cross-links mature into trivalent cross-links.[136] The ratio has been confusingly reported in the literature as either the 1665-to-1685 or 1685-to-1665 intensity ratio. The cross-link ratio can also be reported as the intensity ratio of the 1240 and 1270 cm^{-1} bands of amide III.[137]

It is important to understand that the collagen cross-link ratio does not measure cross-links directly, but rather measures perturbations to the secondary structure of the collagen.

Most of the bone Raman metrics were initially adapted from those used in the bone IR literature. IR metrics should be applicable when analyzing Raman spectra provided there are no overlapping bands. However, validations of these bone quality parameters had initially only been performed for IR spectra. Most of the Raman metrics have recently been validated. Raman measurements of crystallinity have been correlated with x-ray diffraction measurements of the crystal length,[127, 130] and Raman carbonate-to-phosphate ratios have been correlated with chemical measures of the carbonate content.[125] While the Raman mineral-to-matrix ratio has not been correlated with ash weight, it has recently been shown to have a strong positive correlation with the validated IR mineral-to-matrix ratio.[138] There has been no correlation of the Raman collagen cross-link ratio with direct biochemical characterization of cross-links, although the same bands that are validated for use in the IR are used to calculate the Raman collagen cross-link ratio.

The Raman metrics discussed above report on composition and nanostructure contributions to bone quality. Quality encompasses composition and architectural properties of the bone tissue and its ability to resist excessive deformation and fracture. These bone quality metrics may be altered in mechanically compromised tissue, and Raman spectroscopy can detect these changes. For example, in biopsies matched for age and bone volume fraction, the Raman-measured carbonate-to-phosphate ratio was significantly higher (~20%) in women who suffered an osteoporotic fracture than in

women who did not suffer a fracture.[139] In a Raman study on the mechanical deformation of bone tissue, shear bands were found at the edges of a mechanical indent and cross-links were assumed to be ruptured. In this region, visible changes in the frequency of amide bands were observed.[137] Clearly, Raman spectroscopy provides a wealth of information on bone health and quality and is a valuable technique for studying the mineral and organic phases of normal and compromised bone tissue.

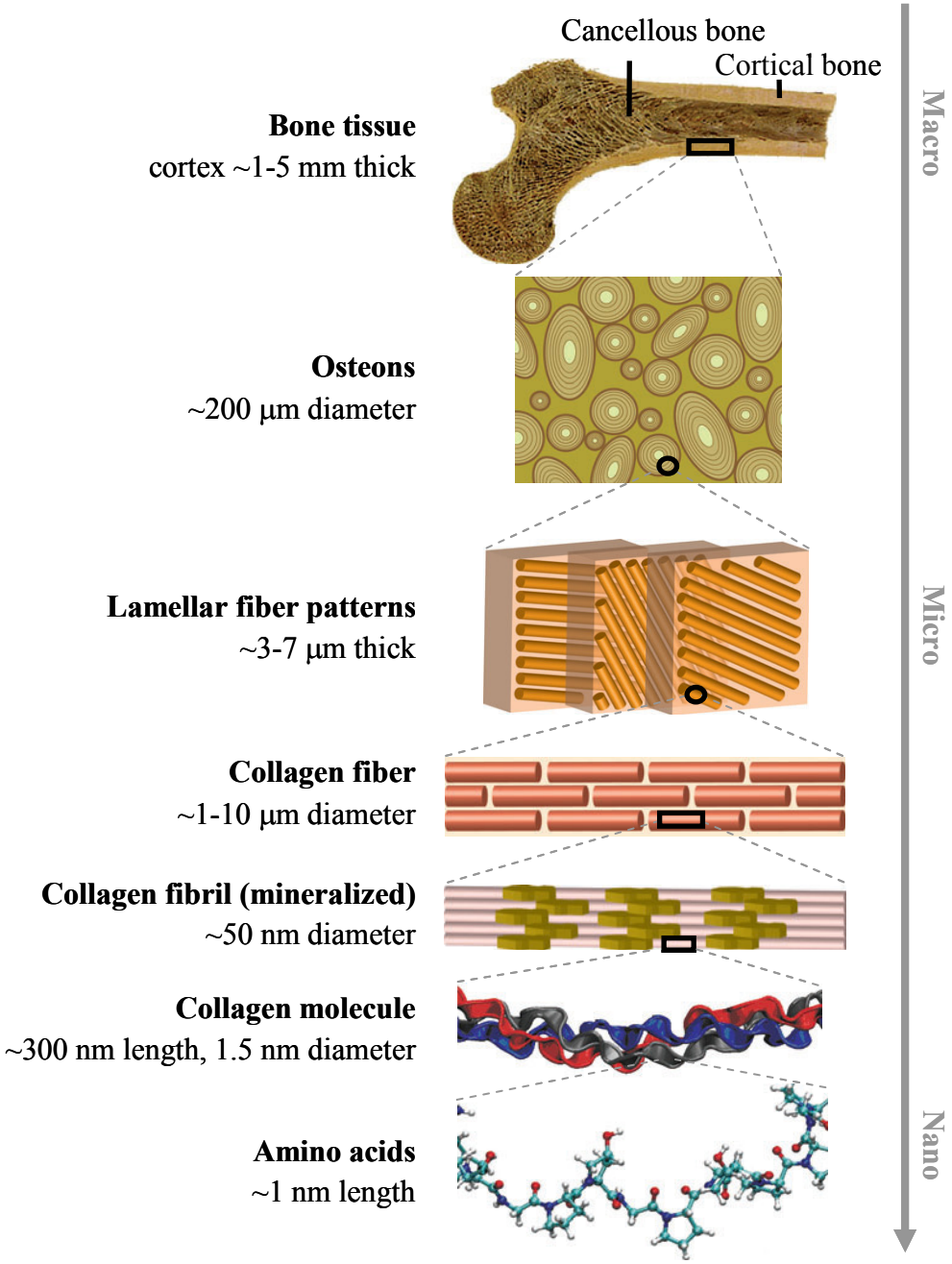

Figure 1.1. Hierarchical structure of bone. On a macroscale, bone is arranged into either cortical or cancellous bone. Cortical bone is composed of osteons, which consist of layers of collagen fibers known as lamellae. Each fiber is composed of a group of fibrils. The mineralized collagen fibril is the basic building block of bone. It is composed of a staggered array of collagen molecules formed from three chains of amino acids. Adapted from *Annu. Rev. Mater. Res.*, **40**, M.E. Launey, M.J. Buehler, and R.O. Ritchie, "On the mechanistic origins of toughness in bone," 25-53, 2010, with permission from Annual Reviews, Inc.

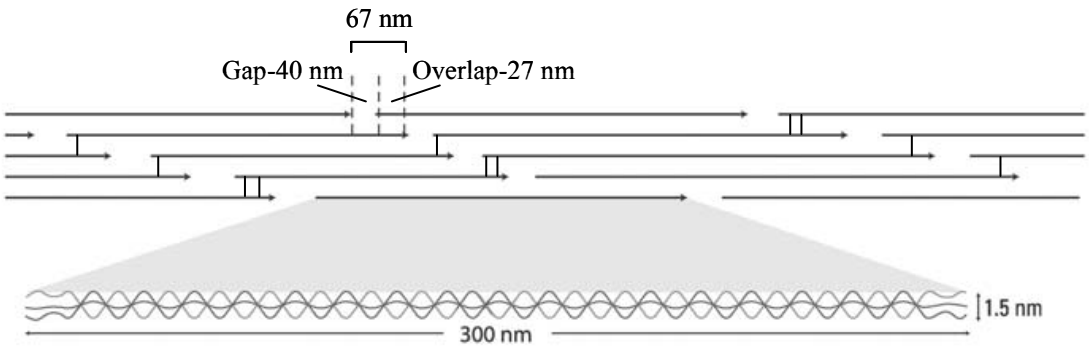

Figure 1.2. Structure of an unmineralized collagen fibril. Collagen molecules (arrows) are arranged head to tail and are offset by 67 nm from collagen molecules in adjacent rows. An individual collagen molecule is approximately 300 nm in length and 1.5 nm in diameter. Intrafibril cross-links occur in the overlap regions. Adapted from *Collagen Primer in Structure, Processing, and Assembly*, **247**, D.E. Birk and P. Bruckner**,** "Collagen suprastructures," 185-205, 2005, with permission from Springer Science+Business Media.

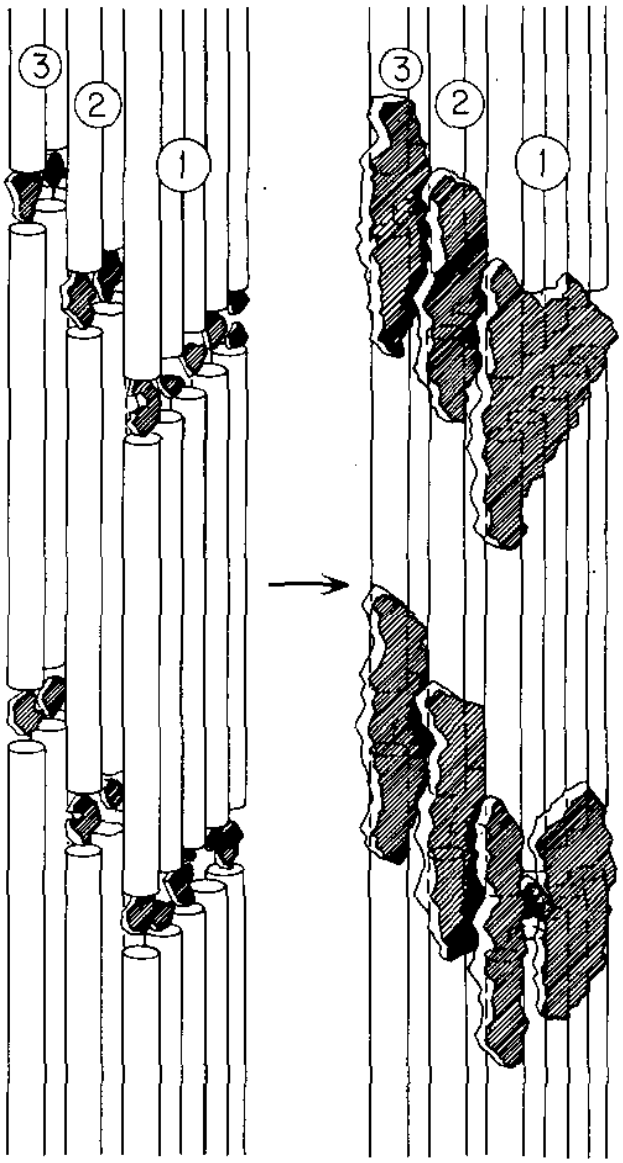

Figure 1.3. Mineralization of a collagen fibril. Three layers of triple helical collagen molecules (cylinders) are shown. The packing of collagen molecules in three dimensions occurs such that gap zones are aligned and create extensive channels throughout the fibril. On the left, early deposition of mineral crystals occurs within the gap zones. Nucleation events within the overlap zones are not shown. Crystals are oriented such that their crystallographic c-axes lie parallel to the long axes of the collagen molecules. On the right, crystal growth may cause smaller crystals to fuse and lead to thin parallel plate-like sheets of mineral. Reprinted from *J. Struct. Biol.*, **110**, W.J. Landis et al., "Mineral and organic matrix interaction in normally calcifying tendon visualized in three dimensions by high-voltage electron microscopic tomography and graphic image reconstruction," 39-54, 1993, with permission from Elsevier.

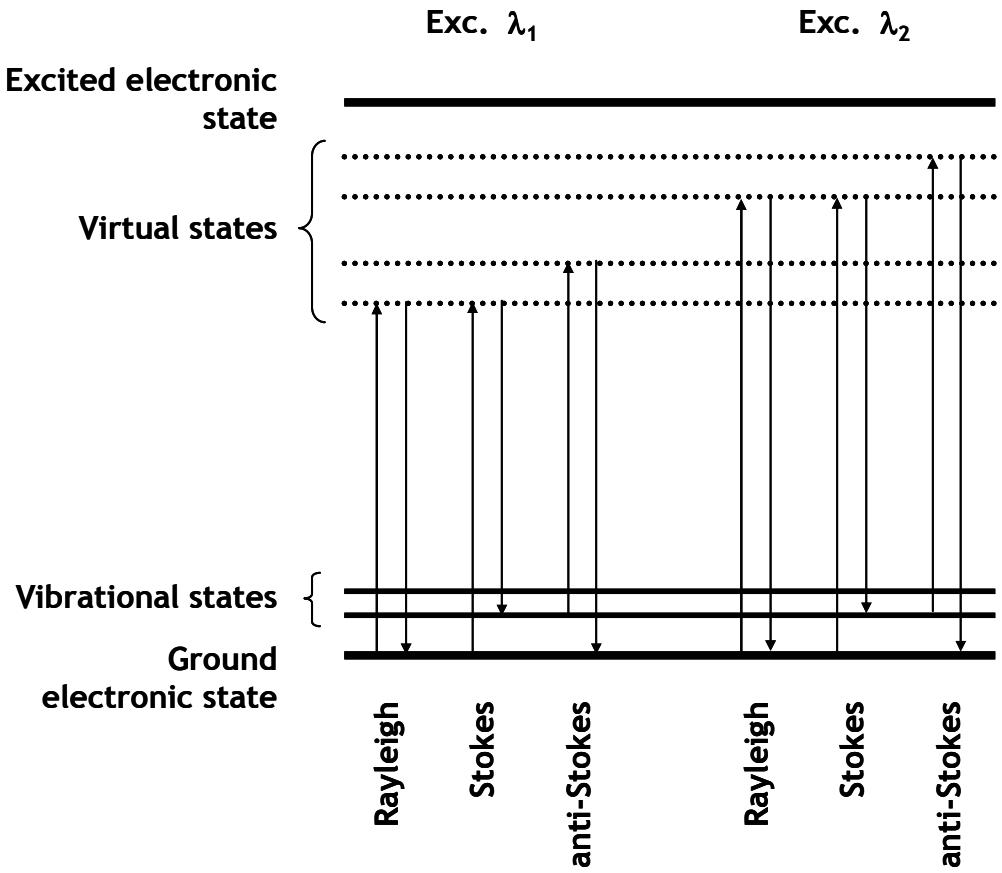

Figure 1.4. Energy level diagram. The processes for Rayleigh, Stokes, and anti-Stokes Raman scattering are shown for two different excitation wavelengths, where excitation wavelength 2 is at a higher energy. The laser determines the energy of the virtual state.

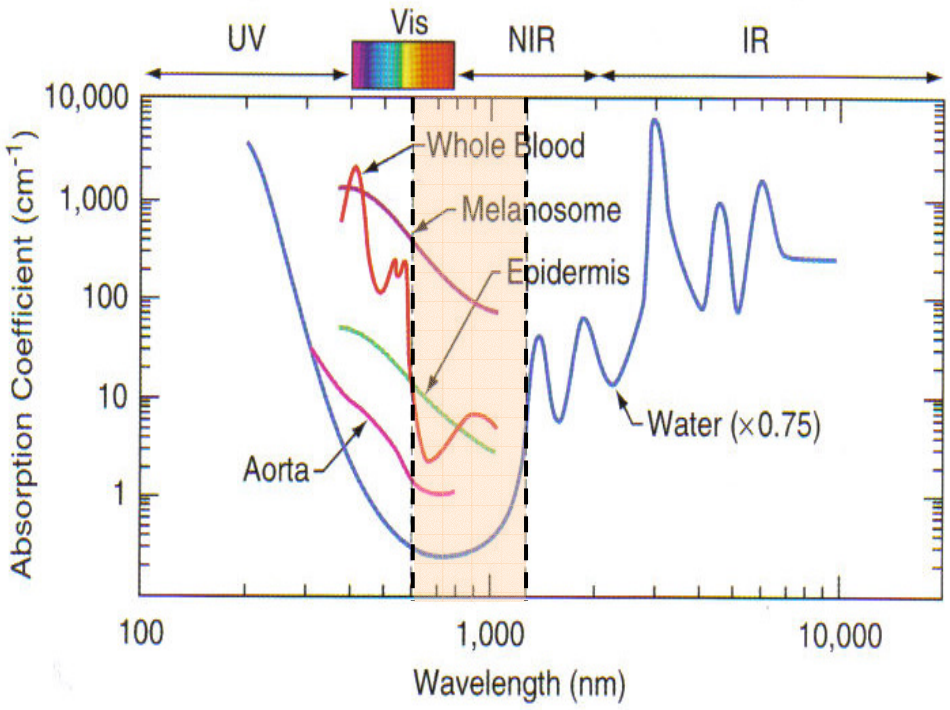

Figure 1.5. Diagnostic window. The absorption of tissue components is at a minimum between 600-1100 nm. Reprinted from *Biomedical Photonics Handbook*, **1**, J. Mobley and T. Vo-Dinh, "Optical properties of tissue," 2:1-2:76, 2003, with permission from Taylor & Francis Group LLC.

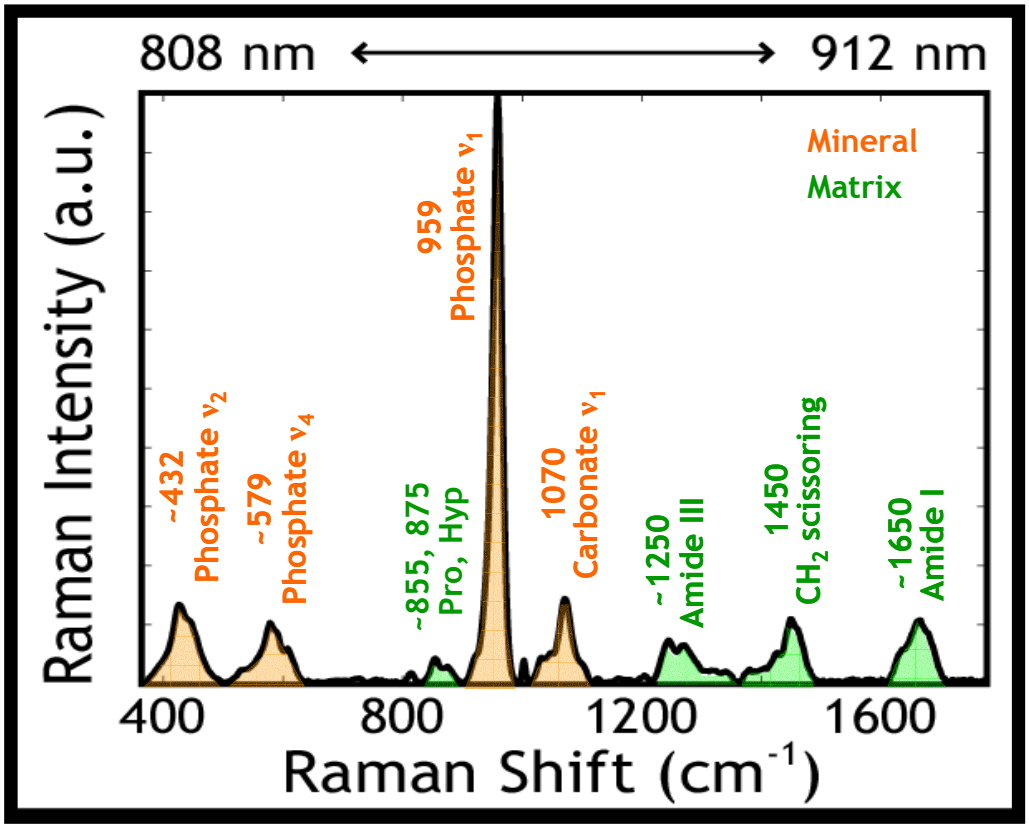

Common Raman metrics

mineral-to-matrix

(959-to-Pro,Hyp or 959-to-amide I) measure of mineral content

carbonate-to-phosphate

(1070-to-959) measure of carbonate substitution in apatitic lattice

crystallinity

(inverse width 959) measure of crystal size and/or perfection

collagen cross-link

(1685-to-1665) measure of collagen fibril maturity

Figure 1.6. Representative Raman spectrum of bone. Mineral and matrix bands are highlighted in orange and green, respectively. Some common metrics that can be calculated from the Raman spectrum of bone are shown.

References

1. A. Hoshino and W. Wallace, "Impact-absorbing properties of the human knee," *J. Bone Joint Surg. Br.* **69-B**(5), 807-811 (1987).

2. H. Shaaban, G. Giakas, M. Bolton, R. Williams, L. R. Scheker, and V. C. Lees, "The distal radioulnar joint as a load-bearing mechanism: A biomechanical study," *J. Hand Surg.* **29**(1), 85-95 (2004).

3. R. B. Martin, D. B. Burr, and N. A. Sharkey, *Skeletal Tissue Mechanics*, Springer-Verlag, New York (1998).

4. J. D. Currey, *Bones: Structure and Mechanics*, Princeton University Press, Princeton (2002).

5. S. V. Dorozhkin and M. Epple, "Biological and medical significance of calcium phosphates," *Angew. Chem. Int. Ed.* **41**(17), 3130-3146 (2002).

6. R. G. Handschin and W. B. Stern, "X-ray diffraction studies on the lattice perfection of human bone apatite (crista iliaca)," *Bone* **16**(4), S355-S363 (1995).

7. R. Astala and M. J. Stott, "First principles investigation of mineral component of bone: CO_3 substitutions in hydroxyapatite," *Chem. Mater.* **17**(16), 4125-4133 (2005).

8. R. Zapanta LeGeros, "Apatites in biological systems," *Prog. Cryst. Growth Charact.* **4**(1-2), 1-45 (1981).

9. P. G. Robey and A. L. Boskey, "The composition of bone," in *Primer on the Metabolic Bone Diseases and Disorders of Mineral Metabolism*, C. J. Rosen, Ed., pp. 32-38, American Society for Bone and Mineral Research, Washington, D.C (2008).

10. G. Bou-Gharios and B. d. Crombrugghe, "Type I collagen structure, synthesis, and regulation," in *Principles of Bone Biology*, J. P. Bilezikian, L. G. Raisz, and G. A. Rodan, Eds., pp. 285-318, Academic Press, San Diego (2002).

11. L. Knott and A. J. Bailey, "Collagen cross-links in mineralizing tissues: A review of their chemistry, function, and clinical relevance," *Bone* **22**(3), 181-187 (1998).

12. M. E. Launey, M. J. Buehler, and R. O. Ritchie, "On the mechanistic origins of toughness in bone," *Annu. Rev. Mater. Res.* **40**(1), 25-53 (2010).

13. E. J. Kucharz, *The Collagens: Biochemistry and Pathophysiology*, Springer-Verlag, New York (1992).

14. J. Engel and H. P. Bachinger, "Structure, stability and folding of the collagen triple helix," in *Collagen Primer in Structure, Processing and Assembly*, J. Brinckmann, H. Notbohm, and P. K. Muller, Eds., pp. 7-33, Springer-Verlag, Berlin Heidelberg (2005).

15. H. A. Lowenstam and S. Weiner, *On Biomineralization*, Oxford University Press, Inc., New York (1989).

16. M. Tzaphlidou and P. Berillis, "Collagen fibril diameter in relation to bone site. A quantitative ultrastructural study," *Micron* **36**(7-8), 703-705 (2005).

17. D. A. D. Parry, G. R. G. Barnes, and A. S. Craig, "A comparison of the size distribution of collagen fibrils in connective tissues as a function of age and a possible relation between fibril size distribution and mechanical properties," *Proc. R. Soc. B* **203**(1152), 305-321 (1978).

18. D. E. Birk and P. Bruckner, "Collagen suprastructures," in *Collagen Primer in Structure, Processing and Assembly*, J. Brinckmann, H. Notbohm, and P. K. Muller, Eds., pp. 185-205, Springer-Verlag, Berlin Heidelberg (2005).

19. D. R. Eyre, M. A. Paz, and P. M. Gallop, "Cross-linking in collagen and elastin," *Annu. Rev. Biochem.* **53**(1), 717-748 (1984).

20. S. P. Robins and J. D. Brady, "Collagen cross-linking and metabolism," in *Principles of Bone Biology*, J. P. Bilezikian, L. G. Raisz, and G. A. Rodan, Eds., pp. 319-334, Academic Press, San Diego (2002).

21. D. R. Eyre and J.-J. Wu, "Collagen cross-links," in *Collagen Primer in Structure, Processing and Assembly*, J. Brinckmann, H. Notbohm, and P. K. Muller, Eds., pp. 207-229, Springer-Verlag, Berlin Heidelberg (2005).

22. N. C. Avery and A. J. Bailey, "Restraining cross-links responsible for the mechanical properties of collagen fibers: Natural and artificial," in *Collagen Structure and Mechanics*, P. Fratzl, Ed., pp. 81-110, Springer Science+Business Media, LLC, New York (2008).

23. J. Moradian-Oldak, S. Weiner, L. Addadi, W. J. Landis, and W. Traub, "Electron imaging and diffraction study of individual crystals of bone, mineralized tendon and synthetic carbonate apatite," *Connect. Tissue Res.* **25**(3-4), 219-228 (1991).

24. W. J. Landis, M. J. Song, A. Leith, L. McEwen, and B. F. McEwen, "Mineral and organic matrix interaction in normally calcifying tendon visualized in three dimensions by high-voltage electron microscopic tomography and graphic image reconstruction," *J. Struct. Biol.* **110**(1), 39-54 (1993).

25. W. J. Landis, "Tomographic imaging of collagen-mineral interaction: Implications for osteogenesis imperfecta," *Connect. Tissue Res.* **31**(4), 287-290 (1995).

26. M. A. Rubin, I. Jasiuk, J. Taylor, J. Rubin, T. Ganey, and R. P. Apkarian, "TEM analysis of the nanostructure of normal and osteoporotic human trabecular bone," *Bone* **33**(3), 270-282 (2003).

27. S. J. Eppell, W. Tong, J. Lawrence Katz, L. Kuhn, and M. J. Glimcher, "Shape and size of isolated bone mineralites measured using atomic force microscopy," *J. Orthop. Res.* **19**(6), 1027-1034 (2001).

28. S. Weiner and P. Price, "Disaggregation of bone into crystals," *Calcif. Tissue Int.* **39**(6), 365-375 (1986).

29. S. Weiner and W. Traub, "Organization of hydroxyapatite crystals within collagen fibrils," *FEBS Letters* **206**(2), 262-266 (1986).

30. W. Zhang, S. S. Liao, and F. Z. Cui, "Hierarchical self-assembly of nano-fibrils in mineralized collagen," *Chem. Mater.* **15**(16), 3221-3226 (2003).

31. S. C. Cowin and S. B. Doty, *Tissue Mechanics*, Springer Science+Business Media, LLC, New York (2007).

32. J. Y. Rho, L. Kuhn-Spearing, and P. Zioupos, "Mechanical properties and the hierarchical structure of bone," *Med. Eng. Phys.* **20**(2), 92-102 (1998).

33. J. D. Currey, *The Mechanical Adaptations of Bones*, Princeton University Press, Princeton (1984).

34. M. Giraud-Guille, "Twisted plywood architecture of collagen fibrils in human compact bone osteons," *Calcif. Tissue Int.* **42**(3), 167-180 (1988).

35. A. Ascenzi and E. Bonucci, "The compressive properties of single osteons," *Anat. Rec.* **161**(3), 377-391 (1968).

36. F. W. Wehrli, H. K. Song, P. K. Saha, and A. C. Wright, "Quantitative MRI for the assessment of bone structure and function," *NMR Biomed.* **19**(7), 731-764 (2006).

37. J. D. Currey, "The mechanical consequences of variation in the mineral content of bone," *J. Biomech.* **2**(1), 1-11 (1969).

38. A. Burstein, J. Zika, K. Heiple, and L. Klein, "Contribution of collagen and mineral to the elastic-plastic properties of bone," *J. Bone Joint Surg. Am.* **57**(7), 956-961 (1975).

39. J. D. Currey, K. Brear, and P. Zioupos, "The effects of ageing and changes in mineral content in degrading the toughness of human femora," *J. Biomech.* **29**(2), 257-260 (1996).

40. D. B. Burr, "Bone material properties and mineral matrix contributions to fracture risk or age in women and men," *J. Musculoskel. Neuron. Interact.* **2**(3), 201-204 (2002).

41. J. S. Yerramshetty and O. Akkus, "The associations between mineral crystallinity and the mechanical properties of human cortical bone," *Bone* **42**(3), 476-482 (2008).

42. X. D. Wang, R. A. Bank, J. M. TeKoppele, and C. M. Agrawal, "The role of collagen in determining bone mechanical properties," *J. Orthop. Res.* **19**(6), 1021-1026 (2001).

43. D. B. Burr, "The contribution of the organic matrix to bone's material properties," *Bone* **31**(1), 8-11 (2002).

44. A. Gautieri, S. Uzel, S. Vesentini, A. Redaelli, and M. J. Buehler, "Molecular and mesoscale mechanisms of osteogenesis imperfecta disease in collagen fibrils," *Biophys. J.* **97**(3), 857-865 (2009).

45. A. Forlino and J. C. Marini, "Osteogenesis imperfecta: Prospects for molecular therapeutics," *Mol. Genet. Metab.* **71**(1-2), 225-232 (2000).

46. A. Ascenzi and E. Bonucci, "The tensile properties of single osteons," *Anat. Rec.* **158**(4), 375-386 (1967).

47. R. B. Martin and J. Ishida, "The relative effects of collagen fiber orientation, porosity, density, and mineralization on bone strength," *J. Biomech.* **22**(5), 419-426 (1989).

48. J. G. Ramasamy and O. Akkus, "Local variations in the micromechanical properties of mouse femur: The involvement of collagen fiber orientation and mineralization," *J. Biomech.* **40**(4), 910-918 (2007).

49. F. G. Evans and R. Vincentelli, "Relations of the compressive properties of human cortical bone to histological structure and calcification," *J. Biomech.* **7**(1), 1-10 (1974).

50. V. Ziv, H. D. Wagner, and S. Weiner, "Microstructure-microhardness relations in parallel-fibered and lamellar bone," *Bone* **18**(5), 417-428 (1996).

51. X. Wang, X. Shen, X. Li, and C. Mauli Agrawal, "Age-related changes in the collagen network and toughness of bone," *Bone* **31**(1), 1-7 (2002).

52. E. E. Wilson, A. Awonusi, M. D. Morris, D. H. Kohn, M. M. Tecklenburg, and L. W. Beck, "Highly ordered interstitial water observed in bone by nuclear magnetic resonance," *J. Bone Miner. Res.* **20**(4), 625-634 (2005).

53. E. E. Wilson, A. Awonusi, M. D. Morris, D. H. Kohn, M. M. J. Tecklenburg, and L. W. Beck, "Three structural roles for water in bone observed by solid-state NMR," *Biophys. J.* **90**(10), 3722-3731 (2006).

54. J. S. Nyman, Q. Ni, D. P. Nicolella, and X. Wang, "Measurements of mobile and bound water by nuclear magnetic resonance correlate with mechanical properties of bone," *Bone* **42**(1), 193-199 (2008).

55. J. S. Nyman, A. Roy, X. Shen, R. L. Acuna, J. H. Tyler, and X. Wang, "The influence of water removal on the strength and toughness of cortical bone," *J. Biomech.* **39**(5), 931-938 (2006).

56. P. Zhu, J. Xu, N. Sahar, M. D. Morris, D. H. Kohn, and A. Ramamoorthy, "Time-resolved dehydration-induced structural changes in an intact bovine cortical bone revealed by solid-state NMR spectroscopy," *J. Am. Chem. Soc.* **131**(47), 17064-17065 (2009).

57. B. Martin, "Aging and strength of bone as a structural material," *Calcif. Tissue Int.* **53**(Suppl. 1), S34-S40 (1993).

58. W. J. Landis, "The strength of a calcified tissue depends in part on the molecular structure and organization of its constituent mineral crystals in their organic matrix," *Bone* **16**(5), 533-544 (1995).

59. M. J. Buehler, "Molecular nanomechanics of nascent bone: fibrillar toughening by mineralization," *Nanotechnology* **18**(29), 295102 (2007).

60. S. D. Chipman, H. O. Sweet, D. J. McBride, M. T. Davisson, S. C. Marks, A. R. Shuldiner, R. J. Wenstrup, D. W. Rowe, and J. R. Shapiro, "Defective proα2(I) collagen synthesis in a recessive mutation in mice: A model of human osteogenesis imperfecta," *Proc. Natl. Acad. Sci. USA* **90**(5), 1701-1705 (1993).

61. T. Hirano, D. B. Burr, R. L. Cain, and J. M. Hock, "Changes in geometry and cortical porosity in adult, ovary-intact rabbits after 5 months treatment with LY333334 (hPTH 1-34)," *Calcif. Tissue Int.* **66**(6), 456-460 (2000).

62. J. A. Buckwalter, M. J. Glimcher, R. R. Cooper, and R. Recker, "Bone biology," *J. Bone Joint Surg. Am.* **77**(8), 1256-1275 (1995).

63. T. J. Martin and E. Seeman, "New mechanisms and targets in the treatment of bone fragility," *Clin. Sci.* **112**(2), 77-91 (2007).

64. C. Bono and T. Einhorn, "Overview of osteoporosis: pathophysiology and determinants of bone strength," *Eur. Spine J.* **12**(Suppl. 2), S90-S96 (2003).

65. D. Faibish, S. M. Ott, and A. L. Boskey, "Mineral changes in osteoporosis," *Clin. Orthop. Rel. Res.* **443**(1), 28-38 (2006).

66. R. Mendelsohn, E. P. Paschalis, P. J. Sherman, and A. L. Boskey, "IR microscopic imaging of pathological states and fracture healing of bone," *Appl. Spectrosc.* **54**(8), 1183-1191 (2000).

67. S. J. Gadeleta, A. L. Boskey, E. Paschalis, C. Carlson, F. Menschik, T. Baldini, M. Peterson, and C. M. Rimnac, "A physical, chemical, and mechanical study of lumbar vertebrae from normal, ovariectomized, and nandrolone decanoate-treated cynomolgus monkeys (macaca fascicularis)," *Bone* **27**(4), 541-550 (2000).

68. A. L. Boskey, E. DiCarlo, E. Paschalis, P. West, and R. Mendelsohn, "Comparison of mineral quality and quantity in iliac crest biopsies from high- and low-turnover osteoporosis: an FT-IR microspectroscopic investigation," *Osteoporos. Int.* **16**(12), 2031-2038 (2005).

69. H. Fleisch, "Bisphosphonates in osteoporosis," *Eur. Spine J.* **12**(Suppl. 2), S142-S146 (2003).

70. S. Ferrari, "Comparing and contrasting the effects of strontium ranelate and other osteoporosis drugs on microarchitecture," *Osteoporos. Int.* **21**(Suppl. 2), 437-442 (2010).

71. M.-C. Monier-Faugere, Z. Geng, E. P. Paschalis, Q. Qi, I. Arnala, F. Bauss, A. Boskey, and H. Malluche, "Intermittent and continuous administration of the bisphosphonate ibandronate in ovariohysterectomized beagle dogs: Effects on bone morphometry and mineral properties," *J. Bone Miner. Res.* **14**(10), 1768-1778 (1999).

72. E. P. Paschalis, A. L. Boskey, M. Kassem, and E. F. Eriksen, "Effect of hormone replacement therapy on bone quality in early postmenopausal women," *J. Bone Miner. Res.* **18**(6), 955-959 (2003).

73. H. Ouyang, P. J. Sherman, E. P. Paschalis, A. L. Boskey, and R. Mendelsohn, "Fourier transform infrared microscopic imaging: Effects of estrogen and estrogen deficiency on fracture healing in rat femurs," *Appl. Spectrosc.* **58**(1), 1-9 (2004).

74. R. Y. Huang, L. M. Miller, C. S. Carlson, and M. R. Chance, "Characterization of bone mineral composition in the proximal tibia of cynomolgus monkeys: effect of ovariectomy and nandrolone decanoate treatment," *Bone* **30**(3), 492-497 (2002).

75. R. Y. Huang, L. M. Miller, C. S. Carlson, and M. R. Chance, "In situ chemistry of osteoporosis revealed by synchrotron infrared microspectroscopy," *Bone* **33**(4), 514-521 (2003).

76. E. P. Paschalis, D. B. Burr, R. Mendelsohn, J. M. Hock, and A. L. Boskey, "Bone mineral and collagen quality in humeri of ovariectomized cynomolgus monkeys given rhPTH(1-34) for 18 months," *J. Bone Miner. Res.* **18**(4), 769-775 (2003).

77. E. P. Paschalis, E. V. Glass, D. W. Donley, and E. F. Eriksen, "Bone mineral and collagen quality in iliac crest biopsies of patients given teriparatide: New results from the fracture prevention trial," *J. Clin. Endocrinol. Metab.* **90**(8), 4644-4649 (2005).

78. J. A. L. Calbet, J. S. Moysi, C. Dorado, and L. P. Rodríguez, "Bone mineral content and density in professional tennis players," *Calcif. Tissue Int.* **62**(6), 491-496 (1998).

79. J. Sanchis-Moysi, C. Dorado, H. Olmedillas, J. A. Serrano-Sanchez, and J. A. L. Calbet, "Bone mass in prepubertal tennis players," *Int. J. Sports Med.* **31**(6), 416-420 (2010).

80. D. H. Kohn, N. D. Sahar, J. M. Wallace, K. Golcuk, and M. D. Morris, "Exercise alters mineral and matrix composition in the absence of adding new bone," *Cells Tissues Organs* **189**(1-4), 33-37 (2009).

81. J. Wallace, K. Golcuk, M. Morris, and D. Kohn, "Inbred strain-specific effects of exercise in wild type and biglycan deficient mice," *Ann. Biomed. Eng.* **38**(4), 1607-1617 (2010).

82. S. Rinnerthaler, P. Roschger, H. F. Jakob, A. Nader, K. Klaushofer, and P. Fratzl, "Scanning small angle X-ray scattering analysis of human bone sections," *Calcif. Tissue Int.* **64**(5), 422-429 (1999).

83. N. P. Camacho, S. Rinnerthaler, E. P. Paschalis, R. Mendelsohn, A. L. Boskey, and P. Fratzl, "Complementary information on bone ultrastructure from scanning small angle X-ray scattering and Fourier-transform infrared microspectroscopy," *Bone* **25**(3), 287-293 (1999).

84. P. Fratzl, O. Paris, K. Klaushofer, and W. J. Landis, "Bone mineralization in an osteogenesis imperfecta mouse model studied by small-angle X-ray scattering," *J. Clin. Invest.* **97**(2), 396-402 (1996).

85. W. Kolodziejski, "Solid-state NMR studies of bone," in *New Techniques in Solid-State NMR*, J. Klinowski, Ed., pp. 235-270, Springer-Verlag, Berlin Heidelberg (2005).

86. Y. Wu, M. J. Glimcher, C. Rey, and J. L. Ackerman, "A unique protonated phosphate group in bone mineral not present in synthetic calcium phosphates: Identification by phosphorus-31 solid state NMR spectroscopy," *J. Mol. Biol.* **244**(4), 423-435 (1994).

87. L. T. Kuhn, Y. Wu, C. Rey, L. C. Gerstenfeld, M. D. Grynpas, J. L. Ackerman, H.-M. Kim, and M. J. Glimcher, "Structure, composition, and maturation of newly deposited calcium-phosphate crystals in chicken osteoblast cell cultures," *J. Bone Miner. Res.* **15**(7), 1301-1309 (2000).

88. G. Cho, Y. Wu, and J. L. Ackerman, "Detection of hydroxyl ions in bone mineral by solid-state NMR spectroscopy," *Science* **300**(5622), 1123-1127 (2003).

89. D. Laurencin, A. Wong, W. Chrzanowski, J. C. Knowles, D. Qiu, D. M. Pickup, R. J. Newport, Z. Gan, M. J. Duer, and M. E. Smith, "Probing the calcium and sodium local environment in bones and teeth using multinuclear solid state NMR and X-ray absorption spectroscopy," *Phys. Chem. Chem. Phys.* **12**(5), 1081-1091 (2010).

90. A. Carden and M. D. Morris, "Application of vibrational spectroscopy to the study of mineralized tissues (review)," *J. Biomed. Opt.* **5**(3), 259-268 (2000).

91. A. L. Boskey and R. Mendelsohn, "Infrared spectroscopic characterization of mineralized tissues," *Vib. Spectrosc.* **38**(1-2), 107-114 (2005).

92. A. Boskey and R. Mendelsohn, "Infrared analysis of bone in health and disease," *J. Biomed. Opt.* **10**(3), 031102 (2005).

93. M. D. Morris, M. V. Schulmerich, K. A. Dooley, and K. A. Esmonde-White, "Vibrational spectroscopic imaging of hard tissues," in *Infrared and Raman Spectroscopic Imaging*, R. Salzer and H. W. Siesler, Eds., pp. 149-171, Wiley-VCH Verlag GmbH & Co. KGaA, Weinham (2009).

94. S. Gourion-Arsiquaud, D. Faibish, E. Myers, L. Spevak, J. Compston, A. Hodsman, E. Shane, R. R. Recker, E. R. Boskey, and A. L. Boskey, "Use of FTIR spectroscopic imaging to identify parameters associated with fragility fracture," *J. Bone Miner. Res.* **24**(9), 1565-1571 (2009).

95. S. Q. Alam, P. P. Kokkinos, and B. S. Alam, "Fatty acid composition and arachidonic acid concentrations in alveolar bone of rats fed diets with different lipids," *Calcif. Tissue Int.* **53**(5), 330-332 (1993).

96. B. Y. Y. Lau, W. E. Ward, J. X. Kang, and D. W. L. Ma, "Femur EPA and DHA are correlated with femur biomechanical strength in young fat-1 mice," *J. Nutr. Biochem.* **20**(6), 453-461 (2009).

97. J. S. Nyman, A. Roy, R. L. Acuna, H. J. Gayle, M. J. Reyes, J. H. Tyler, D. D. Dean, and X. Wang, "Age-related effect on the concentration of collagen crosslinks in human osteonal and interstitial bone tissue," *Bone* **39**(6), 1210-1217 (2006).

98. C. P. Tarnowski, M. A. Ignelzi, W. E. I. Wang, J. M. Taboas, S. A. Goldstein, and M. D. Morris, "Earliest mineral and matrix changes in force-induced musculoskeletal

disease as revealed by Raman microspectroscopic imaging," *J. Bone Miner. Res.* **19**(1), 64-71 (2004).

99. M. V. Schulmerich, K. A. Dooley, M. D. Morris, T. M. Vanasse, and S. A. Goldstein, "Transcutaneous fiber optic Raman spectroscopy of bone using annular illumination and a circular array of collection fibers," *J. Biomed. Opt.* **11**(6), 060502 (2006).

100. P. Matousek, E. R. C. Draper, A. E. Goodship, I. P. Clark, K. L. Ronayne, and A. W. Parker, "Noninvasive Raman spectroscopy of human tissue in vivo," *Appl. Spectrosc.* **60**(7), 758-763 (2006).

101. M. J. Pelletier, "Introduction to applied Raman spectroscopy," in *Analytical Applications of Raman Spectroscopy*, M. J. Pelletier, Ed., pp. 1-52, Blackwell Science Ltd, Oxford (1999).

102. R. L. McCreery, *Raman Spectroscopy for Chemical Analysis*, John Wiley & Sons, Inc., New York (2000).

103. D. A. Long, *The Raman Effect*, John Wiley & Sons Ltd, West Sussex (2002).

104. E. Smith and G. Dent, *Modern Raman Spectroscopy - A Practical Approach*, John Wiley & Sons Ltd, West Sussex (2005).

105. E. B. Hanlon, R. Manoharan, T. W. Koo, K. E. Shafer, J. T. Motz, M. Fitzmaurice, J. R. Kramer, I. Itzkan, R. R. Dasari, and M. S. Feld, "Prospects for in vivo Raman spectroscopy," *Phys. Med. Biol.* **45**(2), R1-R59 (2000).

106. R. R. Anderson and J. A. Parrish, "The optics of human skin," *J. Invest. Dermatol.* **77**(1), 13-19 (1981).

107. J. Mobley and T. Vo-Dinh, "Optical properties of tissue," in *Biomedical Photonics Handbook*, T. Vo-Dinh, Ed., pp. 2:1-2:75, CRC Press, Boca Raton (2003).

108. B. G. Frushour and J. L. Koenig, "Raman scattering of collagen, gelatin, and elastin," *Biopolymers* **14**(2), 379-391 (1975).

109. Z. H. Chi, X. G. Chen, J. S. W. Holtz, and S. A. Asher, "UV resonance Raman-selective amide vibrational enhancement: Quantitative methodology for determining protein secondary structure," *Biochemistry* **37**(9), 2854-2864 (1998).

110. S. U. Sane, S. M. Cramer, and T. M. Przybycien, "A holistic approach to protein secondary structure characterization using amide I band Raman spectroscopy," *Anal. Biochem.* **269**(2), 255-272 (1999).

111. J. T. Pelton and L. R. McLean, "Spectroscopic methods for analysis of protein secondary structure," *Anal. Biochem.* **277**(2), 167-176 (2000).

112. N. C. Maiti, M. M. Apetri, M. G. Zagorski, P. R. Carey, and V. E. Anderson, "Raman spectroscopic characterization of secondary structure in natively unfolded proteins: α-synuclein," *J. Am. Chem. Soc.* **126**(8), 2399-2408 (2004).

113. S. Krimm, "Vibrational analysis of conformation in peptides, polypeptides, and proteins," *Biopolymers* **22**(1), 217-225 (1983).

114. M. A. Bryan, J. W. Brauner, G. Anderle, C. R. Flach, B. Brodsky, and R. Mendelsohn, "FTIR studies of collagen model peptides: Complementary experimental and simulation approaches to conformation and unfolding," *J. Am. Chem. Soc.* **129**(25), 7877-7884 (2007).

115. R. K. Nalla, M. Balooch, J. W. Ager III, J. J. Kruzic, J. H. Kinney, and R. O. Ritchie, "Effects of polar solvents on the fracture resistance of dentin: Role of water hydration," *Acta. Biomater.* **1**(1), 31-43 (2005).

116. M. V. Schulmerich, K. A. Dooley, T. M. Vanasse, S. A. Goldstein, and M. D. Morris, "Subsurface and transcutaneous Raman spectroscopy and mapping using concentric illumination rings and collection with a circular fiber-optic array," *Appl. Spectrosc.* **61**(7), 671-678 (2007).

117. N. J. Crane, M. D. Morris, J. M. A. Ignelzi, and G. Yu, "Raman imaging demonstrates FGF2-induced craniosynostosis in mouse calvaria," *J. Biomed. Opt.* **10**(3), 031119 (2005).

118. D. Pienkowski, T. M. Doers, M.-C. Monier-Faugere, Z. Geng, N. P. Camacho, A. L. Boskey, and H. H. Malluche, "Calcitonin alters bone quality in beagle dogs," *J. Bone Miner. Res.* **12**(11), 1936-1943 (1997).

119. J. D. Currey, "Changes in the impact energy absorption of bone with age," *J. Biomech.* **12**(6), 459-469 (1979).

120. M. Grynpas, "Age and disease-related changes in the mineral of bone," *Calcif. Tissue Int.* **53**(Suppl 1), S57-S64 (1993).

121. E. P. Paschalis, F. Betts, E. DiCarlo, R. Mendelsohn, and A. L. Boskey, "FTIR microspectroscopic analysis of normal human cortical and trabecular bone," *Calcif. Tissue Int.* **61**(6), 480-486 (1997).

122. C. P. Tarnowski, M. A. Ignelzi, and M. D. Morris, "Mineralization of developing mouse calvaria as revealed by Raman microspectroscopy," *J. Bone Miner. Res.* **17**(6), 1118-1126 (2002).

123. O. Akkus, F. Adar, and M. B. Schaffler, "Age-related changes in physicochemical properties of mineral crystals are related to impaired mechanical function of cortical bone," *Bone* **34**(3), 443-453 (2004).

124. H. Ou-Yang, E. P. Paschalis, W. E. Mayo, A. L. Boskey, and R. Mendelsohn, "Infrared microscopic imaging of bone: Spatial distribution of CO_3^{2-}," *J. Bone Miner. Res.* **16**(5), 893-900 (2001).

125. A. Awonusi, M. D. Morris, and M. M. J. Tecklenburg, "Carbonate assignment and calibration in the Raman spectrum of apatite," *Calcif. Tissue Int.* **81**(1), 46-52 (2007).

126. R. Legros, N. Balmain, and G. Bonel, "Age-related changes in mineral of rat and bovine cortical bone," *Calcif. Tissue Int.* **41**(3), 137-144 (1987).

127. J. S. Yerramshetty, C. Lind, and O. Akkus, "The compositional and physicochemical homogeneity of male femoral cortex increases after the sixth decade," *Bone* **39**(6), 1236-1243 (2006).

128. J. J. Freeman, B. Wopenka, M. J. Silva, and J. D. Pasteris, "Raman spectroscopic detection of changes in bioapatite in mouse femora as a function of age and in vitro fluoride treatment," *Calcif. Tissue Int.* **68**(3), 156-162 (2001).

129. O. Akkus, A. Polyakova-Akkus, F. Adar, and M. B. Schaffler, "Aging of microstructural compartments in human compact bone," *J. Bone Miner. Res.* **18**(6), 1012-1019 (2003).

130. J. D. McElderry, N. D. Sahar, D. H. Kohn, M. M. J. Tecklenburg, and M. D. Morris, "Validation of Raman spectroscopic bone mineral crystallinity metrics," (in preparation).

131. N. Pleshko, A. Boskey, and R. Mendelsohn, "Novel infrared spectroscopic method for the determination of crystallinity of hydroxyapatite minerals," *Biophys. J.* **60**(10), 786-793 (1991).

132. S. Gadaleta, E. Paschalis, F. Betts, R. Mendelsohn, and A. Boskey, "Fourier transform infrared spectroscopy of the solution-mediated conversion of amorphous calcium phosphate to hydroxyapatite: New correlations between X-ray diffraction and infrared data," *Calcif. Tissue Int.* **58**(1), 9-16 (1996).

133. F. F. M. de Mul, C. Otto, J. Greve, J. Arends, and J. J. ten Bosch, "Calculation of the Raman line broadening on carbonation in synthetic hydroxyapatite," *J. Raman Spectrosc.* **19**(1), 13-21 (1988).

134. G. Penel, G. Leroy, C. Rey, and E. Bres, "MicroRaman spectral study of the PO_4 and CO_3 vibrational modes in synthetic and biological apatites," *Calcif. Tissue Int.* **63**(6), 475-481 (1998).

135. E. P. Paschalis, E. DiCarlo, F. Betts, P. Sherman, R. Mendelsohn, and A. L. Boskey, "FTIR microspectroscopic analysis of human osteonal bone," *Calcif. Tissue Int.* **59**(6), 480-487 (1996).

136. E. P. Paschalis, K. Verdelis, S. B. Doty, A. L. Boskey, R. Mendelsohn, and M. Yamauchi, "Spectroscopic characterization of collagen cross-links in bone," *J. Bone Miner. Res.* **16**(10), 1821-1828 (2001).

137. A. Carden, R. M. Rajachar, M. D. Morris, and D. H. Kohn, "Ultrastructural changes accompanying the mechanical deformation of bone tissue: A Raman imaging study," *Calcif. Tissue Int.* **72**(2), 166-175 (2003).

138. S. Gourion-Arsiquaud, J. C. Burket, L. M. Havill, E. DiCarlo, S. B. Doty, R. Mendelsohn, M. C. H. v. d. Meulen, and A. L. Boskey, "Spatial variation in osteonal bone properties relative to tissue and animal age," *J. Bone Miner. Res.* **24**(7), 1271-1281 (2009).

139. B. R. McCreadie, M. D. Morris, T.-c. Chen, D. S. Rao, W. F. Finney, E. Widjaja, and S. A. Goldstein, "Bone tissue compositional differences in women with and without osteoporotic fracture," *Bone* **39**(6), 1190-1195 (2006).

CHAPTER II

RAMAN MICROSPECTROSCOPIC IMAGING OF EQUINE BONE

1 Chapter overview

Bone is a dynamic tissue that adapts to the loads it experiences. The first section of this chapter investigates the changes bone undergoes during fracture and how stress is distributed. In the second section, compositional changes that occur in response to extreme exercise are presented. Raman imaging is used for stress mapping in the fracture model and composition mapping in the model for an extreme athlete. The bone utilized in both models is equine bone. For the fracture model, equine bone is used because equine bones are larger and easier to machine for the experiment, although another type of bone could have been used. In the athlete model, the use of equine bone is vital because a racehorse is the model that was used for an extreme athlete.

2 Stress mapping of undamaged, strained, and failed regions of bone using Raman spectroscopy

2.1 Introduction

Vibrational spectroscopy has been used to monitor the response of bone to external stress. One common spectroscopic response to external stress is a wavenumber shift in one or more of the spectral bands. For example, in high-pressure studies of calcium hydroxyapatite and other inorganic minerals similar to bone mineral,[1-4] the vibrational bands associated with the phosphate groups were shown to exhibit strain-dependent shifts. Subsequent high-pressure X-ray diffraction and Raman spectroscopic studies by Comodi and coworkers found that the phosphate ν_1 band shift in fluorapatite was mainly due to a change in the cation/anion spacing of phosphate.[5, 6] Similar effects in bone have been seen in our lab, including high-pressure Raman studies[7] and ongoing NMR experiments.[8]

In studies on bone, the mineral component has been examined in microdamaged,[9] fractured,[10] and nanoindented[11] regions. Researchers have observed a shift in the PO_4^{-3} ν_1 symmetric stretch, the most intense band in the bone spectrum. In microdamaged and fractured regions, an additional mineral factor was present, whose PO_4^{-3} ν_1 band corresponded to a higher wavenumber (963 cm^{-1} and 965 cm^{-1}, respectively) than the carbonated hydroxyapatite typically found in bone (~ 959 cm^{-1}). In the nanoindentation study, a PO_4^{-3} ν_1 band shift occurred in the middle of the indent where compression had occurred. A shift was not observed in the control region outside the indent, indicating that the shift was an effect of damage, and not a cause of it.

Pezzotti and colleagues have taken advantage of this phenomenon and monitored a shift in the PO_4^{-3} ν_1 band during fracture propagation of bovine cortical bone.[12-14] Quantitative stress fields were calculated and Raman stress maps were generated, allowing toughening mechanisms, such as microcracking, to be visualized. In subsequent studies, the PO_4^{-3} ν_1 band shift was monitored in murine bone during physiological loading and observed to change,[15] and on nanoindented teeth, Raman images were generated mapping this wavenumber shift.[16] The results of these studies suggest bone mineral plays a dynamic role in the response to external stress.

Because the mineral band position is sensitive to stress, we wanted to monitor the mineral response in a bone model where understanding stress distributions would be important, such as in a fracture model. Ritchie and coworkers introduced into the biomechanics literature the double-notch specimen, a model in which the early stages of fracture can be examined.[17] The specimens are rectangular beams of bone that have similar rounded notches milled equidistant from each end (Figure 2.1). In four-point bend tests, maximum strains occur at the roots of the notches, and eventually the bone fractures at one of the notches. Because both notches experience the same bending moment, when one notch breaks, the other remains 'frozen' in the state directly preceding fracture.

The objective of this preliminary study was to determine stress distributions in the double-notch specimen using Raman imaging. In this paper, we acquire spectra around the roots of unbroken and fractured notches and monitor stress via spectral shifts in the PO_4^{-3} ν_1 band. The resulting Raman images map the stress distribution.

2.2 Materials and methods

2.2.1 *Specimen preparation*

Fresh-frozen equine third metacarpals (Mc-III) from three female thoroughbreds were used. One horse died of a fracture of the left forelimb fetlock, and the cause of death of the other two horses was unknown. Specimens were milled to approximate dimensions of 2 mm (width) x 2 mm (thickness) x 21 mm (length). The geometry of the specimens is shown in Figure 2.1a. Specimen length corresponded to the long axis of the bone. Rounded notches (depth ~ 0.6-0.7 mm) were created using a 0.75 mm dental cutting disk (SummaDisk, Shofu Corp.) mounted on a CNC machine. The depths of both notches were made as similar as possible to ensure comparable stress-strain fields at the notch tips. Symmetric four-point bending tests (inner loading span S ~ 5mm) were conducted on the double-notch specimens. The specimens were loaded at 0.01 mm/s using an EnduraTec ELF 3200 testing machine (BOSE Corporation, ElectroForce Systems Group, Eden Prairie, MN). The bone was in tension on the side where the notches were located. The specimens remained hydrated throughout the preparation and testing procedures. Specimens were stored at -80°C until Raman images were acquired.

2.2.2 *Raman imaging*

A locally constructed Raman microprobe with a line-focused laser beam was used to image the double-notch specimens. Briefly, a 20x/0.75 NA objective (S Fluor, Nikon Instruments, Inc., Melville, NY) focused a 400-mW 785-nm diode laser (Invictus, Kaiser Optical Systems, Inc., Ann Arbor, MI) onto the specimen. Raman scatter was collected through the same objective and focused into a NIR-optimized spectrograph (HoloSpec f/1.8, Kaiser Optical Systems, Inc.) equipped with a 25-μm slit to provide spectral

resolution of 3-4 cm^{-1}. The detector was a thermoelectrically-cooled, back-illuminated, deep-depletion charge-coupled device (CCD) camera (DU401-BR-DD, Andor Technology, South Windsor, CT) operating at -75 °C. Hyperspectral images were acquired through the use of either a scanning mirror or motorized translation stage integrated with the microscope. For some specimens, images were acquired by scanning the line-focused laser across a stationary specimen using a single-axis galvanometer scanning mirror (6240H, Cambridge Technology, Inc., Lexington, MA). The field of view of the objective was smaller than the area to be imaged. Because of this, after mirror scanning over a region of 50 μm on the stationary specimen, the specimen was manually translated 50 μm, and the process repeated. Mirror movement and data acquisition were controlled via LabVIEW 7.1 (National Instruments, Austin, TX) software. The line focus enabled the simultaneous collection of spectra for each row of pixels on the CCD detector. Spectra collected along a line in this way are called a transect. Transects were acquired using an integration time of 60 s and 3.125-μm steps. The laser power at the specimen was ~ 105 mW. As a matter of convenience, the scanning mirror system was replaced by a motorized translation stage (H101A Proscan II, Prior Scientific, Inc., Rockland, MA). Hyperspectral images taken after this modification were then acquired by translating the specimen beneath the objective. Transects were acquired using an integration time of 60 s and 6.25-μm steps, and the laser power at the specimen was ~ 170 mW. The dashed boxes labeled as 1, 2, or 3 in Figure 2.1b indicate the approximate areas where images were collected. Box 1 is the undamaged area (control region), box 2 is the nonfractured notch (strained region), and box 3 is the fractured notch (failed region). During all Raman measurements, specimens were kept

hydrated in PBS buffer. To determine the spectral effect of protease inhibitor (Protease Inhibitor Cocktail P8340, Sigma-Aldrich, St. Louis, MO), it was added to the buffer used for specimen 2.

2.2.3 *Data analysis*

All data reduction was performed in MATLAB (The Mathworks, Inc., Natick, MA) using vendor-supplied and locally written scripts. Pre-processing included wavenumber calibration, correction for the curvature of spectral bands caused by the large gathering angle of the spectrograph, removal of noise spikes, subtraction of dark current, and correction for the wavelength response of the CCD. The wavenumber calibration procedure converted the CCD pixel axis into wavenumbers. The position of a Raman band can be estimated to a fraction of a pixel width by fitting the band to a Gaussian/Lorentzian profile.[18] This procedure ensured the wavenumber axis was accurate to approximately 0.1 cm^{-1}. Data processing was only carried out in the spectral region of interest (750 – 1750 cm^{-1}) and only on pixel rows in the middle of the CCD detector; rows at the edges of the CCD were not processed because they did not contain spectroscopic data. An iterative baselining procedure was used to remove the background fluorescence.[19] For images taken with the scanning mirror, each 50-μm section was processed individually. The sections were then concatenated to create the final image that spanned the region either of the unbroken notch, failed notch, or control region. Phosphate center of gravities (CGs) were calculated over the range of 930 – 980 cm^{-1}, which included the PO_4^{-3} ν_1 band at ~959 cm^{-1} and a prominent shoulder band at ~945 cm^{-1}. Below is the CG equation used:

$$\frac{\sum_{930\ cm^{-1}}^{980\ cm^{-1}} (I \times \nu)}{\sum_{930\ cm^{-1}}^{980\ cm^{-1}} I} \tag{2.1}$$

where I is the intensity in counts at each specified wavenumber and ν is the wavenumber value. The shift in the PO_4^{-3} ν_1 CG ($\Delta\ \nu$) was determined by calculating the difference between the CG at a particular point and the average CG of the control region for that beam (Eq. 2.2).

$$\Delta\ \nu = CG - \text{mean}(CG_{\text{control region}}) \tag{2.2}$$

Stresses were then calculated using the following equation:

$$\text{Stress} = \Delta\ \nu\ /\ (d\nu/dP) \tag{2.3}$$

where dν/dP is a coefficient representing the average change in position of the $PO_4^{-3}\nu_1$ band per unit pressure. The bovine cortical bone value of ~2.5 cm^{-1}/GPa measured by Pezzotti et al. under four-point bending was used.[12, 14] Finally, the effect of region (control, strain, fail) was tested with repeated measures ANOVA (analysis of variance) using a significance value of 0.05 (SAS 9.1.3., SAS Institute, Inc., Cary, NC).

2.3 Results

The most intense band in the bone spectrum is phosphate ν_1, which is indicative of carbonated hydroxyapatite and its position is sensitive to the mineral environment. The inset of Figure 2.2 shows the non-Gaussian shape of the PO_4^{-3} ν_1 band, with the CG labeled.

In this study, three bone specimens were imaged. Raman images taken on beam 1 from an undamaged region and at the base of the unbroken and fractured notch are shown in Figure 2.3. It is important to note that all of these Raman images are maps of the stress calculated using Eq. 2.3. All the images for this beam are on the same color scale, and

the x and y axes are in microns, where the y-axis corresponds to the length of the laser line. The average stress value in the control region (Figure 2.3a) was 0.004 MPa. The Raman image of the unbroken notch is shown in Figure 2.3b, along with a superimposed outline of the notch edge (x ~ 30-360 μm) to visualize where certain features of the notch appear. In the corresponding microscope image, the central black box denotes the imaged region and the tickmarks in the box represent every 100 μm. The Raman image of the unbroken notch had higher stress, with the highest stress being concentrated at the corners of the notch. At each of the unbroken notches, an average stress value was calculated from a 50 x 50 μm area above each corner, indicated by the dashed lines in Figures 2.3b, 2.4b, and 2.5b. The averages from all specimens and regions are compiled in Table 2.1. At the left and right corners of beam 1, the average stress values were 140.1 MPa and 127.0 MPa. The stress propagated ~100 μm away from the notch edge. For the fractured notch (Figure 2.3c), the edge of the notch and beginning of the fracture are located in the lower left-hand corner of the image. The outline from x ~ 100-250 μm indicates the edge of the notch. The outline from 0-100 μm designates the edge of the fracture; the bone fractured at ~100 μm in the image and propagated off to the left. At the failed notches, average stress values were calculated from a 25 x 25 μm area near the edges of the fracture (these ROIs are shown in Figures 2.3c, 2.4c, and 2.5c). For beam 1, regions of higher stress (137.1 MPa) were only observed near the edge of the fracture and propagated ~50 μm away (from y ~ 40-90 μm).

For beam 2 (Figure 2.4), the average value in the control region was -0.01 MPa. For the nonfractured notch of beam 2, a similar stress pattern as the nonfractured notch of beam 1 was observed. The corners of the unbroken notch were right below x ~200 and

~600 μm in the image. Average stresses of 81.0 MPa (left) and 162.2 (right) were seen at the very edge of these corners. Above the left corner, a stress of ~90 MPa extended ~100 μm away from the edge of the notch. At the right corner, a similar pattern was observed, except a larger magnitude stress extended into the tissue. For the fractured notch of beam 2, the fracture was located from x ~ 100-400 μm and extended along the entire y-axis. The regions of greatest stress were located near the left (234.3 MPa) and right (197.8 MPa) edge of the fracture. Also, a region of higher stress was located from x ~ 850-900 um, near the bottom of the image. It can be seen in Figure 2.4 that the hardware change of replacing the scanning mirror with the motorized stage had a beneficial effect on image quality; images taken with the motorized stage (i.e. Figure 2.4) are "seamless", whereas images taken with the scanning mirror (i.e. Figures 2.3 and 2.5) usually show a "seam" every 50 μm, the increment at which the specimens were manually translated.

For beam 3 (Figure 2.5), the stress pattern was different from those of the previous 2 specimens. The average stress value in the control region was -0.01 MPa. Unlike beams 1 and 2, the stressed regions at the unbroken notch were not really focused at the corners, but instead propagated across the notch (x = 0-500 μm) in the center of the image (y ~ 40-110 μm). In this large region, the average stress value was 57.2 MPa. However, at the left and right notch corners, the average stress was 15.1 MPa and 26.6 MPa, respectively. For the fractured notch, the fracture was in the middle of the image. In the designated region on the left side of the fracture, the average stress value was 13.2 MPa. On the right side, the average value was 43.2 MPa. Other regions of higher stress existed across the center of the image, but this was not different than the unbroken notch.

Repeated measures ANOVA was used to test for any differences in stress values among regions (control, strain, fail). A repeated measures design was used because the 3 regions were imaged in each specimen. In each region, the average stress values were calculated over the 2 ROIs indicated on the stress maps, and these measurements were treated as an independent replicate. For the control regions, the 2 average stress values were calculated by splitting the image in half at x = 100 μm and averaging over the first 100 μm for the first sub-region and the last 100 μm for the second sub-region. Treating region as the repeated factor, a significant difference in stress values was found ($p=0.0166$). Using the Tukey-Kramer post-hoc analysis, we found that the stress values in the control region were significantly smaller than those in the strain ($p=0.0425$) and fail regions ($p=0.0169$). Stress values did not differ significantly between the strain and fail regions ($p=0.4256$).

Because the stress patterns were different for specimen 3, a one-way ANOVA was used to detect differences among specimens, which was the between-subjects factor. A significant difference was detected ($p<0.0001$), and the Tukey-Kramer post-hoc analysis found that specimen 3 had significantly lower stress values than specimens 1 ($p=0.0003$) and 2 ($p<0.0001$).

2.4 Discussion

It can be seen in Figure 2.2 that the shape of the PO_4^{-3} ν_1 band is non-Gaussian because of unresolved shoulder bands that correspond to other phosphate environments. Thus, the CG of the PO_4^{-3} ν_1 band is a useful way to gather information about different mineral environments present via changes in intensity or position of these shoulder bands. Any changes in shoulder bands are overlooked if only the peak center is examined.

Shifts in the PO_4^{-3} ν_1 CG were converted into stress values using a conversion factor of 2.5 cm^{-1}/GPa. This term represents the expected wavenumber shift of the PO_4^{-3} ν_1 band and allows for the calculation of unknown stress fields in the mineral phase. It was determined by loading bovine cortical bone under four-point bending, the same type of loading used for the double-notch specimens. This value is similar to the 2.47 cm^{-1}/GPa calculated for hydroxyapatite.[20] The observed spectral shift was mainly due to a change in the spacing between the cations and anions of phosphate (a reversible effect), and a permanent change like distortion (changing bond lengths relative to one another) was far less likely. For example, Comodi and colleagues found very little change in the P-O bond lengths of phosphate, even when applying 4.72 GPa.[5] This pressure is far greater than that needed to fracture equine third metacarpals in four-point bending (bending strength = 227 ± 27 MPa).[21] Hence, it is very likely that the PO_4^{-3} ν_1 band shift is entirely due to changes that occur in spacing between the ions of phosphate.

The region near the unbroken notch corresponded to bone in a state directly preceding fracture. The most commonly observed pattern was a higher stress concentrated above the corners of the notch. This existence of residual stress suggested that the tissue remained in a loaded state. The residual stress formed a "U" or "V" pattern, with the greatest stress being located near the notch corners and the vertex or least stressed region being located close to the center of the notch. This pattern is consistent with the stress profile generated from a finite element model of the double-notch four-point bending specimen (Figure 2.6). The S_{11} stress component is plotted, which is the direction along the length of the beam. The model shows the stress is most concentrated near both corners of the notch, with predicted stresses of

approximately 230 MPa. For beams 1 and 2 (Fig. 2.3b and 2.4b), the stress in these V-shaped regions was ~134 MPa (average of the two ROIs) for beam 1 and ~ 122 MPa (average of the two ROIs) for beam 2 which were significantly different from control regions. The average values we calculate are less than the bending strength (227 ± 27 MPa) but greater than the yield stress (110 ± 27 MPa) for equine third metacarpals.[21] Some likely reasons that the average values are lower than the bending strength and predicted stresses of the model are because 1) the dv/dP coefficient was not calculated for the equine bone samples, but estimated from the dv/dP coefficient for bovine bone, and 2) the mineral is deposited in and around the matrix and its distribution is not homogeneous. This distribution probably contributes to the stripe-like morphology seen in the images, where points of high stress and low stress exist side by side. This is similar to the effect that Pezzotti has observed.[12, 14] If the individual data points (rather than the averages) in these ROIs are examined, it can be seen that numerous individual points do experience stresses of over 200 MPa.

In examination of images of unbroken notches, care must be exercised in interpretation. For beam 1, the notch was located along the bottom edge of the Raman image from about 30-360 μm. In this region, ~20 μm of the laser line was focused in the notch and not on bone. However, a bone signal was still detected even though the boundary of the notch appeared to be a sharp edge in the corresponding microscope image. The peak response of the video camera was lower than 700 nm, which minimized scattering effects in the microscope image. The near-infrared (NIR) excitation light used to generate the Raman images penetrated farther into the tissue and the scattering response of the signal was emphasized. The nonsharp boundary in the Raman image was

mainly because NIR light is multiply scattered in bone.[22] Thus, the boundary of the notch seen with visible light (microscope image) is sharper and more distinct than the boundary seen with near-infrared light (Raman image). The excitation (and Raman-generated) light propagates through the depth of the specimen, and Raman light is remitted not only from the surface of the bone, but also deeper along the notch edge. Hence, even though part of the laser beam was focused in the notch and not directly over bone, bone spectra could still be collected with our objective, albeit at a lower absolute signal and lower signal-to-noise ratio. Even in regions where the entire length of the laser line was focused on bone, Raman light that originated from deeper layers was collected. However, this out-of-focus light had a lower intensity and lower signal-to-noise ratio than the in-focus light at the surface of the bone. In order to exclude this effect, the system would need to be confocal, but this would result in reduced signal.

The stress pattern near the unbroken notches was different from the pattern near the fractured notches, even though both regions nominally experienced the same loading (because of the nearly symmetrical notches). When compared to the unbroken notch, the tissue at the corners of the fractured notch did not have as high of a residual stress. In these corner regions, the tissue appears to have elastically recovered after the notch fractured, resulting in a smaller residual stress in the mineral component. However, mineral stress can still be seen near the edges of the fracture, where the tissue did not elastically recover. The reason is that we have made permanent changes to the matrix in this region and have broken or distorted collagen cross-links. Because the mineral is deposited in and around the matrix, the response of the mineral and matrix are coupled. In regions near the fracture, there are permanent changes to the matrix but not necessarily

permanent changes to the mineral. However, an increased stress in the mineral is observed because of the coupling with the permanently stressed matrix. If all the collagen were removed, the mineral might return to almost its original state. The average stresses near the beam 1 and 2 fracture edges were about 137 MPa and 216 MPa (average of the two ROIs). Again, this was significantly higher than in control regions.

In order to determine the effects of protease inhibitor on bone spectra, protease inhibitor was added to the buffer used for all regions of beam 2, but not in the buffer used for beam 1. The protease inhibitor exhibited a band at 951 cm^{-1} that overlapped with the PO_4^{-3} ν_1 band in bone. When the laser was focused on the bone surface, the 951 cm^{-1} band comprised approximately 1% of the total area of the PO_4^{-3} ν_1 band, and it was determined that the protease inhibitor did not interfere with CG calculations. However, in regions where the buffer was pooled (i.e. within the fracture), the spectrum of the protease inhibitor contributed approximately 20% or more to the total area. This contribution could not be effectively removed by subtraction. Multivariate techniques were not used to remove the contribution because of the continuous, overlapping distribution of protease inhibitor and bone. For these reasons, the data in the fractured region was not used and the regions were left as white space. The other small white spaces in Figures 2.4b and 2.4c resulted from removal of data contaminated with a noise spike that overlapped with the PO_4^{-3} ν_1 band or a fluorescent background that could not be properly removed by baselining.

Beam 3 displayed different stress patterns for both notches, and was significantly different from beams 1 and 2. The stress observed at both notches was less than that of beams 1 and 2. This lower-magnitude stress was spread out across the length of the

notch and not really concentrated at the corners (Figure 2.5b). For the fractured notch, stress was present away from the edge of the fracture and across the middle of the image, suggesting the tissue did not relax during or after fracture, and the stress did not recover elastically. Another difference was that beam 3 fractured from the center of the notch, whereas the other specimens fractured at the corner of the notch where the greatest tension would be expected.

Differences among the specimens were analyzed to determine the reason for the discrepancy in residual stress patterns. Specimens 1, 2, and 3 were all excised from the dorsal-medial region of the Mc-III bone of female thoroughbreds, from either the distal or proximal end of the bone. A mixture of left and right bones were used, however, previous studies have shown that no differences existed in collagen orientation[23] and bone mineral content (BMC)[24] for left and right bones. The most likely reason for the discrepancy in specimen stress response was the age of the specimens. Beam 3 came from a horse that was 6 years old, whereas beams 1 and 2 came from horses that were 2 and 4 years younger, respectively.

The average strength of equine Mc-III bone peaks sometime between the age of 4 to 7 years; El Shorafa and colleagues found that peak strength was attained within this range[25] and Lawrence et al. showed that both BMC and bone breaking strength, defined as the maximum stress the material can withstand, peaked near 6 years of age.[24] From the force-displacement curves, the maximum breaking force for the 6-year-old bone (beam 3) was 54.9 N, whereas for the 2- and 4-year-old specimen it was 63.8 N and 66.5 N, respectively. In our study, the 6-year-old bone (specimen 3) was less strong than the younger bones. Lawrence's study also found that in maturing horses, the strength of

bone was due mainly to the increasing BMC. The Raman mineral-to-matrix band ratio (intensity values of phosphate ν_1 at ~959 cm^{-1}/proline at ~853 cm^{-1}), a measure of the amount of mineral in bone, for the 3 specimens was calculated in the failed notch ROIs designated in Figures 2.3c, 2.4c, and 2.5c. The average mineral-to-matrix ratio for specimens 1, 2, and 3 were 13.9 ± 1.1, 13.8 ± 1.1, and 11.8 ± 1.6. The mineral-to-matrix ratio was lower in the beam that had the smallest breaking force. The lower mineral content, perhaps from recent remodeling, may have contributed to the lower strength of that beam. Another reason for the different stress patterns at both notches could be because the bone structure caused the stress distribution to be different than the 2 previous specimens. However, because of the small number of specimens these conclusions are only preliminary.

It can be seen in Figure 2.5c that signal was collected from within the fractured region. Unlike beam 2, no protease inhibitor was used for beam 3. The reason bone signal was collected was because the fracture process was irregular, and the break was not perpendicular to the surface. Regions of bone were present below the plane of best focus (i.e. plane of bone surface), as illustrated in Figure 2.7. Because the Raman microprobe was not confocal, signal from these deeper layers was collected, albeit at a lower intensity.

2.5 Conclusion

In conclusion, residual stress in the loaded bone tissue was measured by analyzing band shifts in PO_4^{-3} ν_1. These mineral band shifts were a consequence of changes in spacing between phosphate cations and anions which is a reversible effect. A band shift

in the mineral component still could be measured after four-point bending, implying that the tissue near the unbroken notch and the edge of the fracture were left in a loaded state. Residual stresses in the strain and fail regions were significantly different than in control regions ($p=0.0425$ and $p=0.0169$, respectively). In beams 1 and 2, the location and pattern of the residual stresses was in agreement to that of the predicted stresses from a linear finite element analysis of the fracture specimen, where the highest stresses at the unbroken notch were concentrated at the corners. The calculated average stress magnitudes were lower than predicted, mainly because the dv/dP value used in the study was an estimate for equine bone, and the mineral distribution was not uniform. The exact stress distributions probably depend on the specimen age, BMC, and local load distribution. Careful interpretation of Raman images was required because both multiple light scattering in bone and irregularity of the fracture site caused signal to be collected from below the uppermost surface of the bone (i.e. the best plane of focus).

3 Composition mapping in model for extreme athlete

3.1 Introduction

Functional adaptation of bone is the process by which bone adapts to the loads that it experiences.[26] It does this through the process of bone modeling and remodeling, where bone is resorbed and then laid back down. This can result in changes to both the geometric and material properties of the tissue. For example, in athletes who play tennis, their dominant arm has a larger bone mass and area than their non-dominant arm.[27, 28] In another exercise study, mice that ran on a treadmill had greater tibial strength, but

showed no increase in tibial cross-sectional size or shape. Rather, compositional changes were observed.[29, 30]

Failure of functional adaptation to protect bones from fracture is common, particularly in cases that involve highly repetitive loading like exercise. For instance, runners who increase the frequency, duration, or intensity of their runs are at a higher risk for stress fracture.[31] Stress fractures are also common among military recruits during basic training.[32, 33] Stress, or fatigue, fractures are associated with activities that involve repetitive loading of the bone and not a single, traumatic event. They occur when the bone is unable to maintain a balance between skeletal repair and accumulation of microdamage.[31] The remodeling response generated by repetitive loading initially involves bone resorption, which temporarily weakens the bone and may allow microcracks to form more easily. If the loading becomes excessive or rest is inadequate, then microcracks may accumulate and lead to gross fracture.

Stress fracture is also common in the third metacarpal bone (Mc-III) of the racing Thoroughbred.[34] This bone is analogous to the third metacarpal in the human hand, however, the equine bone is much larger, found in the forelimbs, and provides much of the weight-bearing support for the horse. Fractures are more common in young Thoroughbred racehorses (1-2 years old)[35] where compressive strains at the mid-diaphysis of the Mc-III bone during racing have been measured to exceed -5000 microstrain.[34] However, fractures are rare in older horses (>4 years old).[34-36] In a 4- and 12-year-old Thoroughbred racehorse, the strain was lower and measured to be approximately -3300 microstrain.[34]

In addition to measuring strain, geometric changes have been studied in the Mc-III bone of racehorses as a function of age. The minimum moment of inertia, a measure of bone ability to resist bending in the dorsal-palmar direction, increased dramatically from 1-year-old Thoroughbreds to 4-year-old Thoroughbreds. After 4 years of age, changes in the minimum moment of inertia were insignificant. Fatigue fractures were also rare after this age, suggesting that changes to the inertial properties of the Mc-III bone served to decrease bone strain to some 'normal' level.[37] Other studies have examined the effect of exercise on Mc-III bone properties. Researchers found that exercise increased the impact strength and ability to absorb energy of the mid-diaphysis of the Mc-III bone of Thoroughbreds.[36] Another study found that exercise increased the subchondral bone thickness in the distal end of the Mc-III bone within a few months.[38] All of these results suggest that the equine Mc-III bone can alter its properties in order to decrease fracture risk. However, the exact mechanism of functional adaptation in this bone is not known.

In order to investigate this subject further, Muir and coworkers examined the role that microcracking played in functional adaptation in the distal region of the Mc-III joint of racehorses.[39] Oblique sections of the distal end of the Mc-III bone were divided into four regions-of-interest: lateral condyle (LC), lateral condylar groove (LCG), medial condyle (MC), and medial condylar groove (MCG). Microcracking in subchondral bone was found to be site-specific and was increased in the condylar groove regions, the region where parasagittal fracture often originates. The researchers found that microcracks may extend and lengthen into the calcified cartilage layer, particularly if preceded by an in-growth of blood vessels into the condylar groove calcified cartilage. The presence of

microcracks in the calcified cartilage preceded eventual development of stress fracture during high-speed running, suggesting that endochondral ossification might be an adaptive response. Also, microcracking appeared to be a key event in triggering functional adaptation.

Interestingly, the authors noticed that in their histological staining studies, subchondral bone from racehorses often had atypical staining in the condyles and condylar groove regions when compared to nonathletic horses.[40] Subchondral bone either did not stain well or the stain pooled and was suggestive of the presence of microcracks. Another outcome seen with histological staining is that the subchondral plate was sometimes collapsed. They hypothesized that the inconsistent staining may be due to a change in the composition of the subchondral bone, and changes in composition may be another process that occurs as part of functional adaptation. Hence, the purpose of this study was to use Raman spectroscopy and determine if a change in the composition of the Mc-III subchondral bone was occurring in response to habitual athleticism.

3.2 Materials and methods

3.2.1 *Specimen preparation*

Fresh-frozen equine specimens from the distal region of the third metacarpal (Mc-III) bone were used. Horses were humanely euthanized for reasons unrelated to the Raman study. One specimen was from an 8-year-old, neutered male Thoroughbred racehorse. A nonathletic specimen was obtained from an age-, gender-, and breed-matched horse that had no history of recent training or racing. Oblique dorso-proximal plantaro-distal frontal plane bone slices were prepared from the distal

joint surfaces of each specimen. Specimens were approximately 1 in (width) x 3 in (length) x 2 mm (thickness). The geometry of the specimens is shown in Figure 2.8. The block was divided into four regions-of-interest (ROI): medial and lateral condyles (MC and LC) and medial and lateral condylar grooves (MCG and LCG), as denoted by the black boxes in the figure. Specimens were stored at -20°C until Raman images were acquired.

3.2.2 *Raman imaging*

A locally constructed Raman microprobe with a line-focused laser beam was used to image the athletic and nonathletic specimens. Hyperspectral images were acquired by translating the specimen beneath the objective via a motorized translation stage integrated with the microscope. The same Raman system as described in section 2.2.2. was used, and thus the details are not repeated here. Transects were acquired using an integration time of 60 s and 20-μm steps. The laser power at the specimen was ~ 150 mW. The black boxes in Figure 2.8 indicate the approximate areas where Raman images were collected. During all Raman measurements, specimens were kept hydrated in phosphate-buffered saline.

3.2.3 *Data analysis*

All data reduction was performed in MATLAB (The Mathworks, Inc., Natick, MA) using vendor-supplied and locally written scripts. Preprocessing included wavenumber calibration, removal of noise spikes, subtraction of dark current, correction for the wavelength response of the CCD, and correction for the curvature of spectral bands caused by the large gathering angle of the spectrograph. Curvature correction was

performed by first rotating the CCD image to account for a slight misalignment of the CCD, and then removing the curvature.[41] Performing image rotation as a step in curvature correction is a more accurate method because most CCDs are slightly tilted with respect to the grating dispersion axis. Data processing was only carried out in the spectral region of interest (665 – 1832 cm^{-1}) and only on pixel rows in the middle of the CCD detector; rows at the edges of the CCD were not processed because they did not contain spectroscopic data or the signal-to-noise ratio was very low. Spectra were baselined using a third-order polynomial fit to selected background regions in the spectrum. The minimum point in each spectrum was set to zero intensity, and then each spectrum was normalized to the phosphate band.

Band height ratios were calculated, including the carbonate-to-phosphate, mineral-to-matrix, and collagen cross-link ratios. Peak fitting individual spectra was impractical due to the large number of spectra in the Raman images. Hence, height values were calculated in Matlab using the height of the band contours in the normalized spectra. To determine band heights, the intensity at the left and right endpoints of each band were calculated. The height difference between the left and right endpoints, if any, was divided by 2. This value was added to the height of the lower-intensity endpoint in order to approximate the height of the local baseline under the peak maximum. Peak height was calculated as the distance from the local baseline to the peak maximum. The peak maximum was taken as the mean over a small range near the maximum. The mean value over a small range was used in order to avoid assigning a noise spike in the data as the peak maximum. The collagen cross-link ratio was calculated as 1685-to-1665, the wavenumber positions of two amide I band components. The carbonate-to-phosphate

ratio was computed as 1070-to-960. The mineral-to-matrix ratio was calculated two different ways. The 960 cm^{-1} phosphate band was used as the mineral component, but the matrix band used was either the sum of the amide I components at 1665 and 1685 cm^{-1} (mm_amI), or the sum of the amide III components at 1245 and 1267 cm^{-1} (mm_amIII).

Once ratios were calculated, upon close inspection, some of the ratios were negative (a physical impossibility) and occurred if the local baseline value was greater than the peak maximum when calculating the height ratios. Negative values were removed, along with values that were greater than 3 standard deviations away from the mean. Due to the limited availability of equine specimens, statistical differences between groups [athletic (n=1) vs. nonathletic (n=1)] could not be tested.

3.3 Results

The means and standard deviations for the collagen cross-link, carbonate-to-phosphate, and mineral-to-matrix ratios in the four ROIs for each specimen were calculated. The height ratio results are shown in Table 2.2. For a given specimen, the average values for a specific ratio from all four regions were fairly similar. For example, in the nonathletic horse, the average values for the cross-link ratio were 0.65, 0.68, 0.66, and 0.62 for the LC, MC, LCG, and MCG regions, respectively. Within a specimen, there were no apparent regional differences. The biggest differences occurred between specimens, particularly in the mineral-to-matrix ratio.

The overall differences for the four imaging parameters are shown in the bar graphs of Figure 2.9. The solid gray bars represent the nonathletic horse and the striped bars represent the racehorse. Each bar is the average value of the four regional (LC, MC,

LCG, MCG) means, and the error bars are the average value of the standard deviations in those same regions. On average, mm_amI increased by 27.2% in the racehorse. The trend was reversed for mm_amIII, with an average decrease of 34.9% in the racehorse. The average difference in the collagen cross-link and carbonate-to-phosphate ratios between the specimens was less than 10%. Because only one specimen in each group was available, statistical differences between the racehorse and nonathletic horse could not be determined.

3.4 Discussion

As can be seen in Table 2.2 and Figure 2.9, the standard deviations for the racehorse were larger. This is because the spectra were noisier, and the lower signal-to-noise ratio caused more fluctuation in the band ratio calculations. The discrepancy between the mineral-to-matrix ratios is also apparent. If compared to the nonathletic specimen, the racehorse has higher mineral-to-matrix values if the ratio is calculated with the amide I band and lower values if the amide III band is used. To investigate this discrepancy, the second derivatives of the mean amide III spectra were calculated for both specimens in all four regions. In general, the second derivatives for the nonathletic specimen had six predominant minima which corresponded to six unresolved peaks. The second derivatives for the racehorse revealed ten predominant minima. As a representative example, the amide III spectrum and its second derivative for the lateral condyle are shown in Figure 2.10 for the racehorse and the nonathletic horse. For the racehorse, the higher intensity of the amide III region, and thus lower mma_amIII ratio, appears to be due to the presence of additional bands in this spectral region. The assignments of these additional bands are uncertain, but C-C or C-H

stretches of lipids can also occur in the spectral region containing amide III.[42] Muir and colleagues have shown that increased vascularization occurs in the articular cartilage of the subchondral plate of Thoroughbred racehorses.[39] The presence of nearby lipids in blood vessels may be contributing bands that overlap with amide III. The second derivative of the amide I contour for both the racehorse and nonathletic horse revealed the same number of minima. For these reasons, the mm_amI ratios were deemed more accurate.

For mm_amI, the ratios were on average 27% higher for the racehorse. The mineral-to-matrix ratio is a measure of the amount of mineral in the sample,[43, 44] so the ratio suggests that the racehorse has more mineral. The deposition of additional mineral is a common response to increased loading of bone.[45-47] The higher ratio suggests that the deposition of more mineral is one way that the Mc-III bone of racehorses adapts to increased athleticism. This functional adaptation process likely serves to decrease the risk of bone fracture.

Additional studies on subchondral bone from racehorses have shown that their bone has undergone recent remodeling.[39, 48] In the racehorse (Mc-III bone at mid-diaphysis), average remodeling over time (as determined by calculating the activation frequency and bone formation rate using a standard algorithm) and recent remodeling (as measured by resorption space density in histologically stained specimens) was significantly higher when compared to nonathletic horses.[49] Another study confirmed that excess resorption space is present in the immediate subchondral bone of racehorses using scanning electron microscopy images.[48] Recent remodeling is initially accompanied by a decrease in the mineral-to-matrix ratio. However, the

mineral-to-matrix ratio in this experiment was found to be increased in the racehorse. The age of the specimens may account for this. In the previously cited studies where remodeling was found to be increased, the horses examined were young, with a mean age of 3.2 years and 2.0 years for the different studies. The two specimens examined in this study were both from horses 8 years of age. Remodeling rates/resorption rates were not investigated for the specimens in this study, however, remodeling rates usually slow with age. It is likely that the specimens examined in this study had not undergone any recent remodeling, and thus the mineral had time to accumulate, leading to a higher mm_amI ratio.

3.5 Conclusion

The equine Mc-III bone is a model for an extreme athlete. The collagen cross-link, carbonate-to-phosphate, and mineral-to-matrix ratios were calculated. The mineral-to-matrix ratio calculated with the amide I matrix band was increased in the racehorse specimens. This suggests that the addition of more mineral is an adaptive mechanism that allows the bone to negotiate the increased loads it is experiencing. The functional adaptation of depositing more mineral likely allows the racehorse to withstand higher loads and lower its fracture risk.

4 Chapter summary

Raman imaging has been applied to two different equine animal models. One was a model for the early stages of bone fracture and the other was a model for an extreme athlete. Raman imaging is very useful if a spatial variation is expected in the parameter

that is being imaged. The technique was well-suited to map stress distribution in the fracture model. For the athlete model, imaging over a small region, rather than collecting a single transect, was more accurate because any variability in local composition was captured.

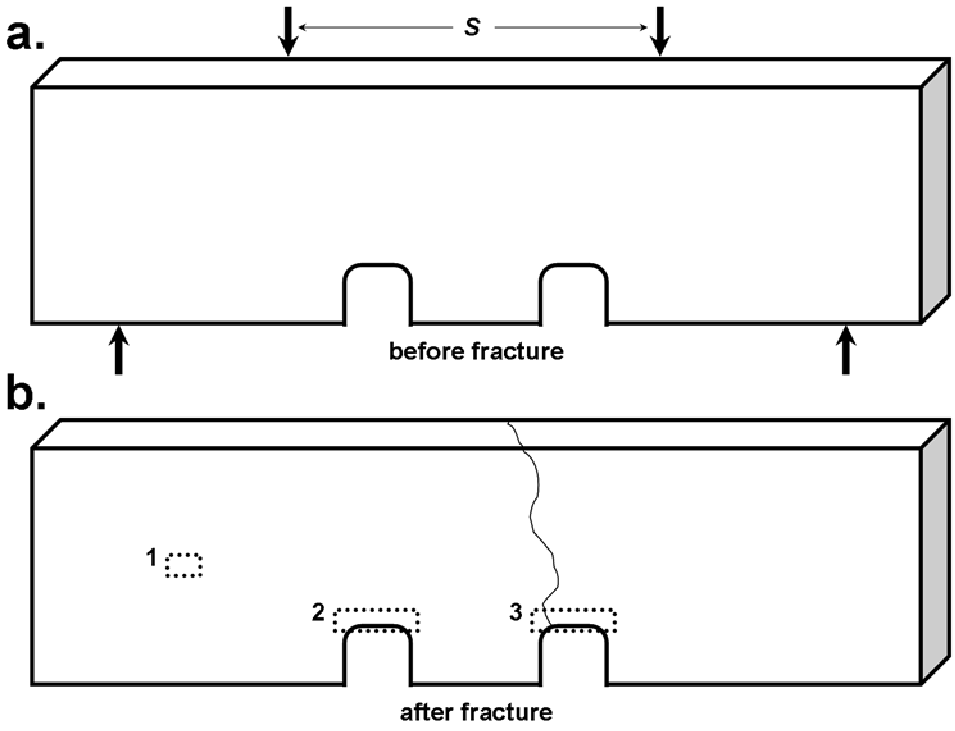

Figure 2.1. Double-notch specimens. (a) Specimen geometry. (b) Upon four-point bending, the bone fractured at one of the notches. The dashed lines indicate the three regions where Raman images were acquired: (1) control, (2) non-fractured, and (3) fractured regions, respectively.

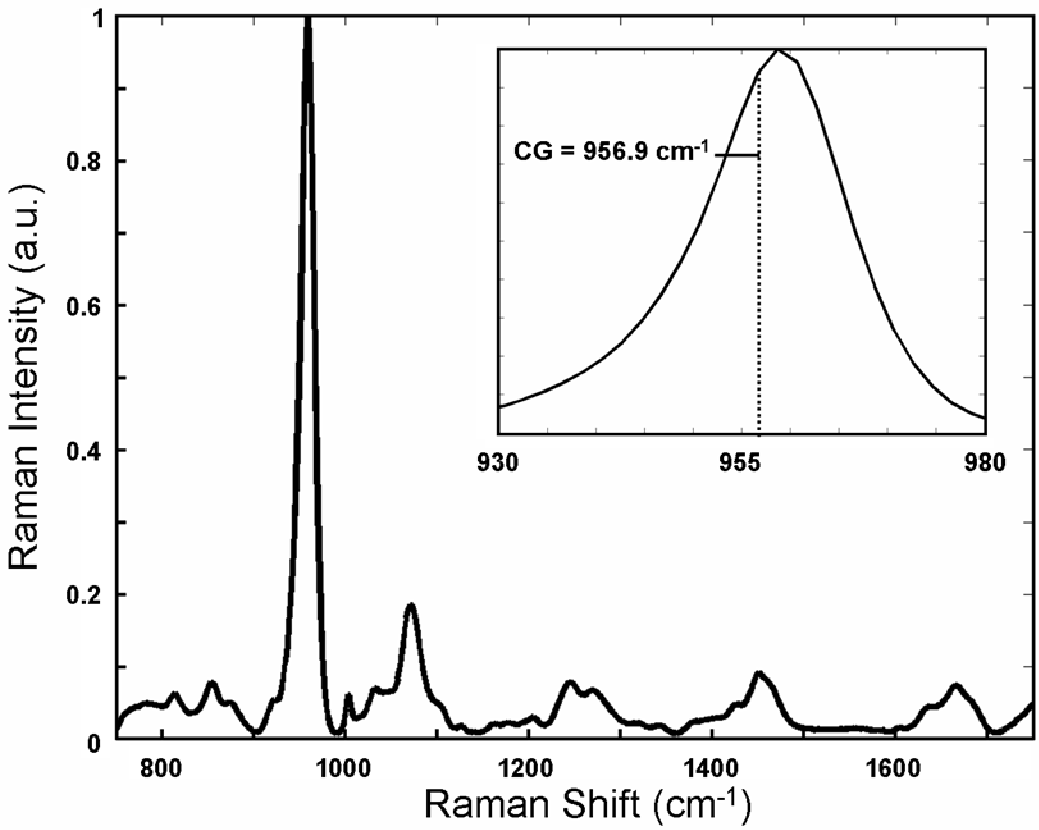

Figure 2.2. Representative Raman bone spectrum and phosphate center of gravity. The phosphate ν_1 peak is centered at ~959 cm^{-1}. The non-Gaussian shape of this band is shown in the inset, and its center of gravity is 956.9 cm^{-1}.

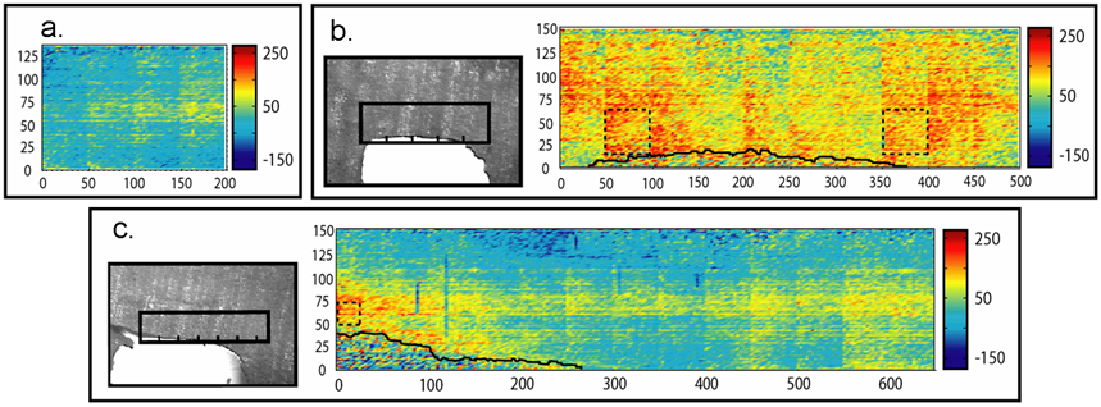

Figure 2.3. Raman images of stress for specimen 1. The x and y axes are in microns, and the color bar range for all images = (-184 to 276 MPa). (a) The average stress value in the control region was 0.004 MPa. [area = 0.027 mm^2] (b) Higher stresses were concentrated at the corners of the unbroken notch, represented by the dashed boxes. The average stress values in those regions were 140.1 and 127.0 MPa. The outline at the bottom of the image was the edge of the notch. [area = 0.075 mm^2] (c) Higher stresses were observed at the edge of the fracture (137.1 MPa in the dashed region). The outline from x ~ 0-100 μm was the edge of the fracture and from x ~ 100-250 μm was the edge of the notch. The subtle vertical lines visible every 50 μm were because the scanning mirror dictated images be taken in 50-μm sections, whereas the horizontal striations were due to imperfect flat-field correction. [area = 0.098 mm^2]

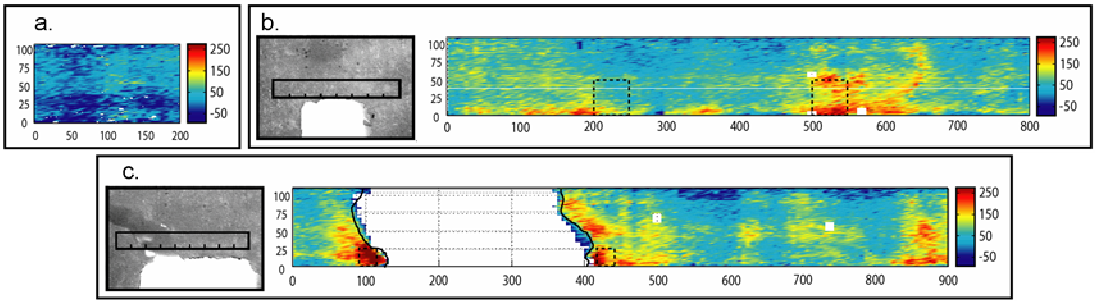

Figure 2.4. Raman images of stress for specimen 2. The x and y axes are in microns, and the color bar range for all images = (-92 to 276 MPa). (a) The average stress value in the control region was -0.01 MPa. [area = 0.021 mm^2] (b) Higher stresses were concentrated at the corners of the unbroken notch with the average stress values being 81.0 and 162.2 MPa. The corners of the notch were just below the Raman image, near x ~ 200 μm and x ~ 600 μm. [area = 0.088 mm^2] (c) Higher stresses were observed at both the left (234.3 MPa) and right (197.8 MPa) edges of the fracture. The fracture was located from x ~ 100-400 μm in the image. A region of higher stress was also located in the lower right-hand corner of the image, above the right corner of the notch. For the images in (b) and (c), the white spaces resulted from removal of data. For all images, imperfect flat-field correction led to striations in the horizontal direction. [area = 0.099 mm^2]

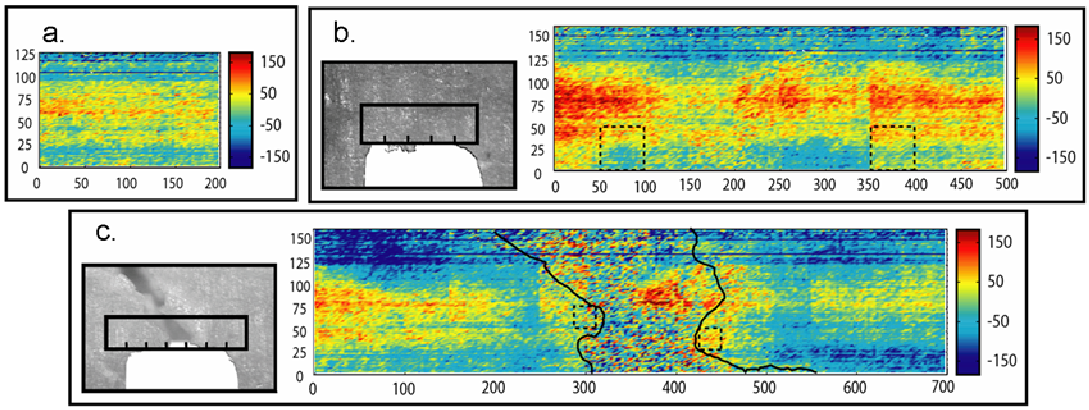

Figure 2.5. Raman images of stress for specimen 3. The x and y axes are in microns, and the color bar range for all images = (-184 to 184 MPa). (a) The average stress value in the control region was -0.01 MPa. [area = 0.025 mm^2] (b) Rather than being concentrated at the corners of the unbroken notch, stress propagated across the notch. [area = 0.083 mm^2] (c) The bone fractured in the middle of the notch. The stresses near the left and right fracture edge were 13.2 and 43.2 MPa, respectively. Horizontal striations were due to imperfect flat-field correction. [area = 0.116 mm^2]

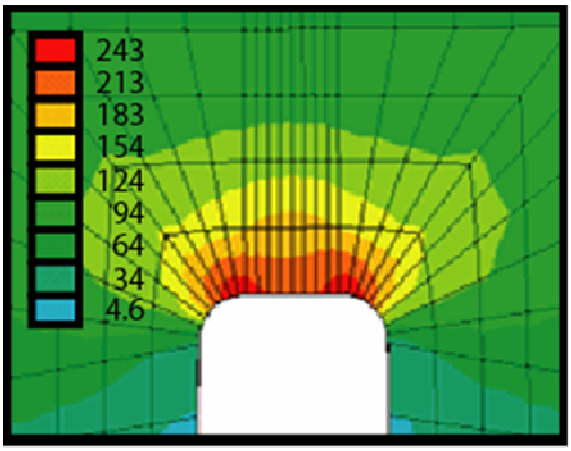

Figure 2.6. Stress profile generated from a finite element model of the double-notch four-point bending specimen. The models were linear elastic and had homogeneous properties such as modulus. The S_{11} stress component is plotted, and the model shows the stress is most concentrated near both corners of the notch, with predicted stresses of approximately 210-240 MPa. The units of the color scale are MPa.

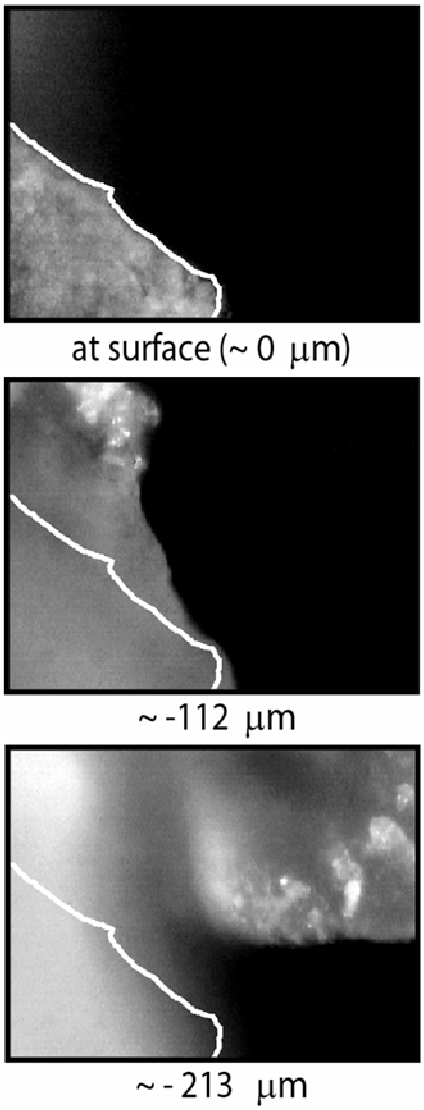

Figure 2.7. Irregular fracture process. When bone fractured, the break was not perpendicular to the surface; regions of bone were present below the surface of the bone, as shown for specimen 3. The white outline corresponded to the uppermost surface of bone at the left edge of the fracture. The regions of bone below the surface contributed to the signal that was collected from within the fractured region.

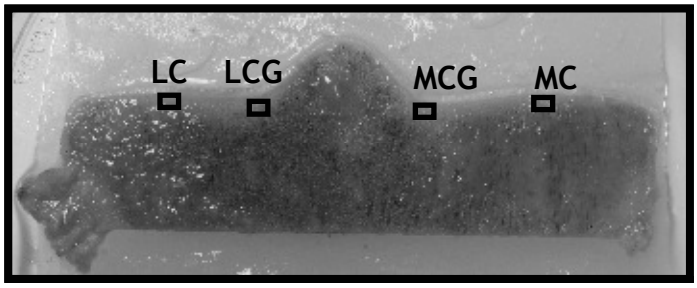

Figure 2.8. Subchondral bone slice through distal end of Mc-III joint. The four regions where Raman images were acquired include the lateral and medial condyle (LC and MC) and the lateral and medial condylar groove (LCG and MCG).

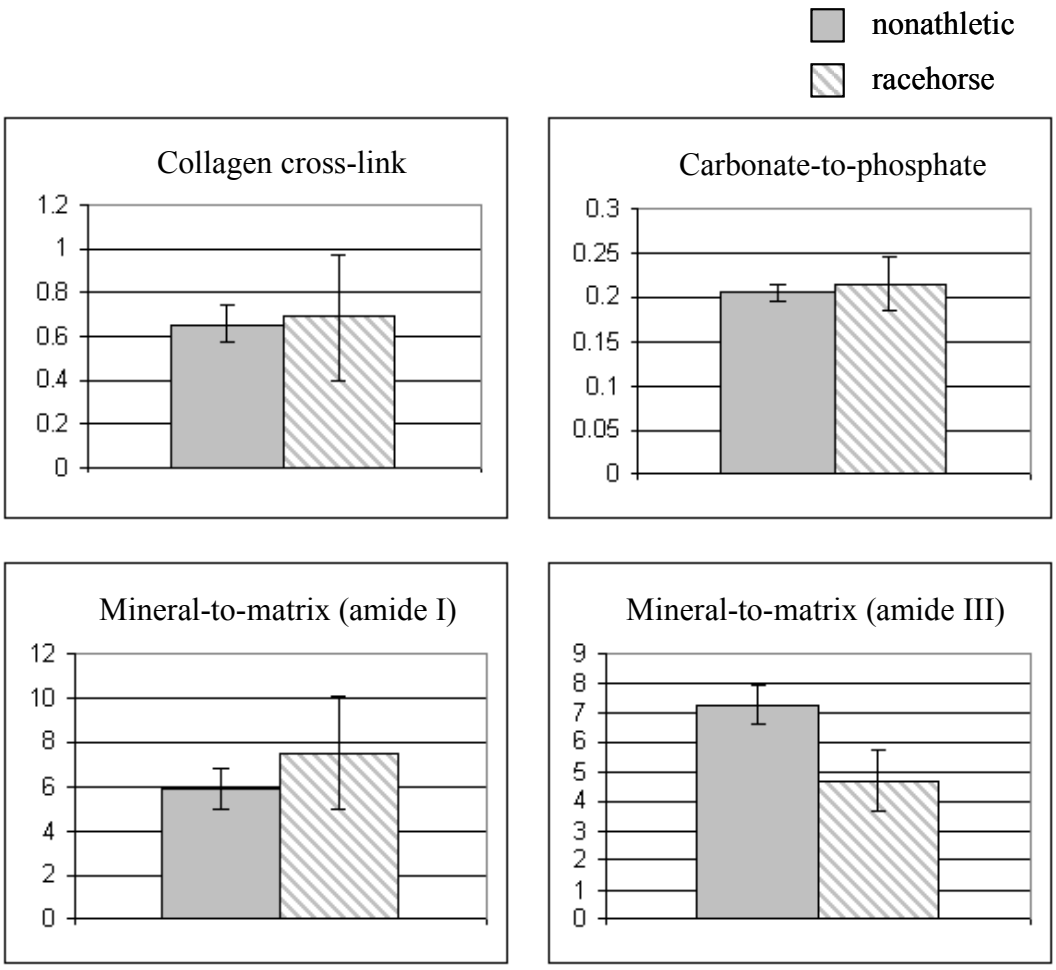

Figure 2.9. Overall averages of band ratios for the racehorse and nonathletic specimens. Each bar is the average of the four regional means (LC, MC, LCG, MCG). The error bars are the average value of the standard deviations in those same regions.

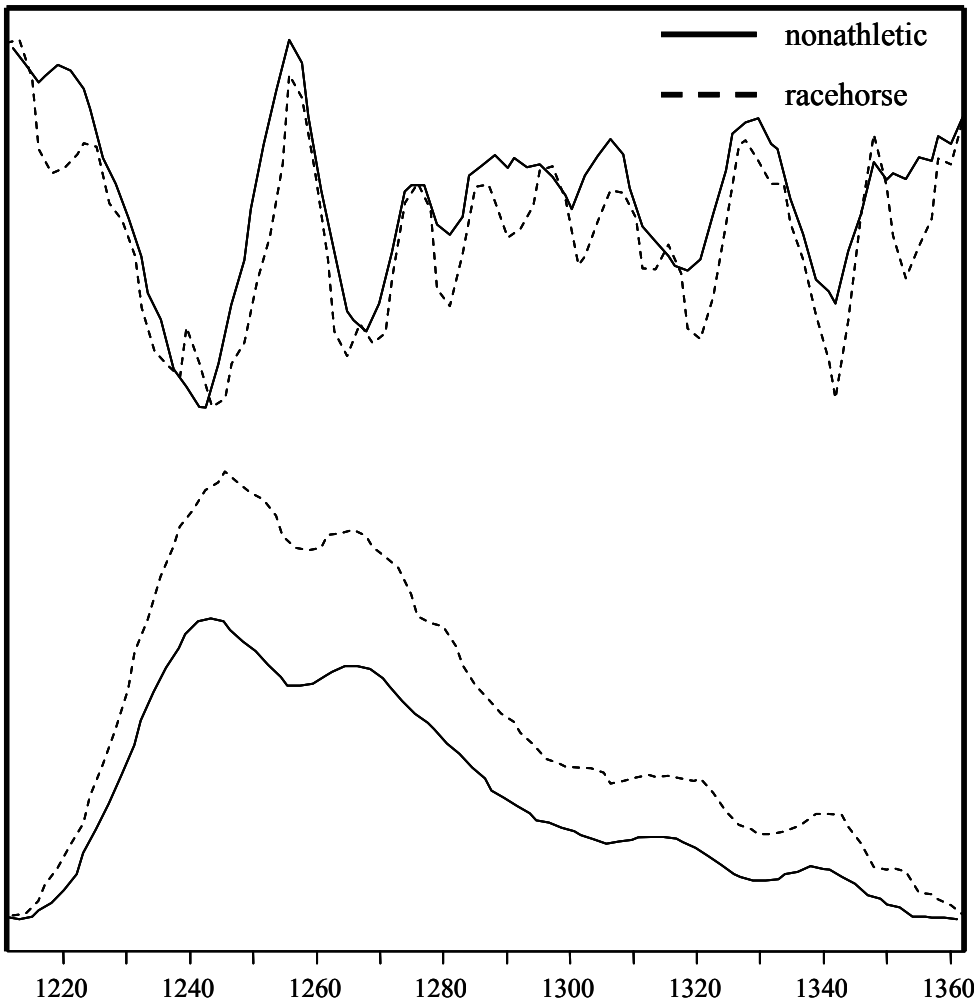

Figure 2.10. Amide III spectral region and corresponding second derivative. Raman spectra of the amide III region from the lateral condyle of the racehorse and nonathletic specimen are shown. The second derivative (top) of the spectrum for the nonathletic specimen had six predominant minima (corresponding to unresolved peaks) and ten predominant minima for the racehorse. The higher intensity of the amide III region in the racehorse specimen was influenced by these additional bands.

	Spec. #	C Side 1	C Side 2	S L corner	S R corner	F L side	F R side
Stress	1	-7.0	7.1	140.1	127.0	NA	137.1
St dev		40.3	43.1	52.0	40.3		38.3
Stress	2	-10.1	9.5	81.0	162.2	234.3	197.8
St dev		38.1	40.4	37.9	43.4	72.3	63.4
Stress	3	0.4	-0.5	15.1	26.6	13.2	43.2
St dev		55.6	51.9	46.3	36.8	60.6	37.0

Table 2.1. Average stress values and standard deviations for all regions of double-notch specimens. The units are MPa, and the control, strain, and failed regions are denoted by C, S, and F, respectively.

		cross-link	cp	mm_amI	mm_amIII
LC	nonath	.65 ± .08	.20 ± .01	6.0 ± .80	7.0 ± .64
MC		.68 ± .09	.20 ± .01	6.1 ± 1.3	7.1 ± .80
LC	race	.67 ± .26	.21 ± .03	7.7 ± 2.8	4.9 ± 1.0
MC		.70 ± .30	.21 ± .03	8.2 ± 2.5	4.8 ± 1.1
LCG	nonath	.66 ± .08	.20 ± .01	6.0 ± .84	7.1 ± .63
MCG		.62 ± .09	.21 ± .01	5.6 ± .84	7.8 ± .61
LCG	race	.69 ± .32	.22 ± .03	7.8 ± 2.9	4.8 ± 1.0
MCG		.69 ± .26	.22 ± .03	6.5 ± 2.0	4.3 ± 1.1

Table 2.2. Average height ratios and standard deviations for all regions of racehorse and nonathletic specimens. The mean collagen cross-link, carbonate-to-phosphate (cp), and mineral-to-matrix (mm) ratios are shown for the four different regions within the nonathletic and racehorse specimen. The use of amide I or amide III as the matrix band in the mineral-to-matrix ratio calculation is denoted as mm_amI or mm_amIII, respectively.

References

1. J. Xu, D. F. R. Gilson, I. F. Butler, and I. Stangel, "Effect of high external pressures on the vibrational spectra of biomedical materials: Calcium hydroxyapatite and calcium fluoroapatite," *J. Biomed. Mater. Res.* **30**(2), 239-244 (1996).

2. S. N. Vaidya, C. Karunakaran, B. M. Pande, N. M. Gupta, R. K. Iyer, and S. B. Karweer, "Pressure-induced crystalline to amorphous transition in hydroxylapatite," *J. Mater. Sci.* **32**(12), 3213-3217 (1997).

3. J. Xu, D. F. R. Gilson, and I. S. Butler, "FT-Raman and high-pressure FT-infrared spectroscopic investigation of monocalcium phosphate monohydrate, $Ca(H_2PO_4)_2 \cdot H_20$," *Spectrochim. Acta A* **54**(12), 1869-1878 (1998).

4. J. Xu, I. S. Butler, and D. F. R. Gilson, "FT-Raman and high-pressure infrared spectroscopic studies of dicalcium phosphate dihydrate ($CaHPO_4 \bullet H_2O$) and anhydrous dicalcium phosphate ($CaHPO_4$)," *Spectrochim. Acta A* **55**(14), 2801-2809 (1999).

5. P. Comodi, Y. Liu, P. F. Zanazzi, and M. Montagnoli, "Structural and vibrational behavior of fluorapatite with pressure. Part I: in situ single-crystal X-ray diffraction investigation," *Phys. Chem. Minerals* **28**(4), 219-224 (2001).

6. P. Comodi, Y. Lin, and M. L. Frezzotti, "Structural and vibrational behaviour of fluorapatite with pressure. Part II: in situ micro-Raman spectroscopic investigation," *Phys. Chem. Minerals* **28**(4), 225-231 (2001).

7. O. de Carmejane, M. D. Morris, M. K. Davis, L. Stixrude, M. Tecklenburg, R. M. Rajachar, and D. H. Kohn, "Bone chemical structure response to mechanical stress studied by high pressure Raman spectroscopy," *Calcif. Tissue Int.* **76**(3), 207-213 (2005).

8. P. Zhu, J. Xu, A. Ramamoorthy, D. H. Kohn, and M. D. Morris, unpublished data.

9. J. A. Timlin, A. Garden, M. D. Morris, R. M. Rajachar, and D. H. Kohn, "Raman spectroscopic imaging markers for fatigue-related microdamage in bovine bone," *Anal. Chem.* **72**(10), 2229-2236 (2000).

10. M. D. Morris, A. Carden, R. M. Rajachar, and D. H. Kohn, "Effects of applied load on bone tissue as observed by Raman spectroscopy," *Proc. SPIE* **4614**(1), 47-54 (2002).

11. A. Carden, R. M. Rajachar, M. D. Morris, and D. H. Kohn, "Ultrastructural changes accompanying the mechanical deformation of bone tissue: A Raman imaging study," *Calcif. Tissue Int.* **72**(2), 166-175 (2003).

12. G. Pezzotti and S. Sakakura, "Study of the toughening mechanisms in bone and biomimetic hydroxyapatite materials using Raman microprobe spectroscopy," *J. Biomed. Mater. Res. Part A* **65A**(2), 229-236 (2003).

13. G. Pezzotti, "Introducing a unique measurement for biomaterial nanomechanics," *Key Engng. Mater.* **240-242**(1), 893-900 (2003).

14. G. Pezzotti, "Raman piezo-spectroscopic analysis of natural and synthetic biomaterials," *Anal. Bioanal. Chem.* **381**(3), 577-590 (2005).

15. M. D. Morris, W. F. Finney, R. M. Rajachar, and D. H. Kohn, "Bone tissue ultrastructural response to elastic deformation probed by Raman spectroscopy," *Faraday Discuss.* **126**(1), 159-168 (2004).

16. L.-H. He, E. Carter, and M. Swain, "Characterization of nanoindentation-induced residual stresses in human enamel by Raman microspectroscopy," *Anal. Bioanal. Chem.* **389**(4), 1185-1192 (2007).

17. R. K. Nalla, J. H. Kinney, and R. O. Ritchie, "Mechanistic fracture criteria for the failure of human cortical bone," *Nat. Mater.* **2**(3), 164-168 (2003).

18. C. K. Mann and T. J. Vickers, "The quest for accuracy in Raman spectra," in *Handbook of Raman Spectroscopy*, I. R. Lewis and H. G. M. Edwards, Eds., pp. 251-274, Marcel Dekker, Inc., New York (2001).

19. C. A. Lieber and A. Mahadevan-Jansen, "Automated method for subtraction of fluorescence from biological Raman spectra," *Appl. Spectrosc.* **57**(11), 1363-1367 (2003).

20. V. Sergo, O. Sbaizero, and D. R. Clarke, "Mechanical and chemical consequences of the residual stresses in plasma sprayed hydroxyapatite coatings," *Biomaterials* **18**(6), 477-482 (1997).

21. G. Bigot, A. Bouzidi, C. Rumelhart, and W. Martin-Rosset, "Evolution during growth of the mechanical properties of the cortical bone in equine cannon-bones," *Med. Eng. Phys.* **18**(1), 79-87 (1996).

22. T. Vo-Dinh, Ed., Biomedical Photonics Handbook, CRC Press, Boca Raton (2003).

23. R. B. Martin, S. T. Lau, P. V. Mathews, V. A. Gibson, and S. M. Stover, "Collagen fiber organization is related to mechanical properties and remodeling in equine bone. A comparison of two methods," *J. Biomech.* **29**(12), 1515-1521 (1996).

24. L. A. Lawrence, E. A. Ott, G. J. Miller, P. W. Poulos, G. Piotrowski, and R. L. Asquith, "The mechanical properties of equine third metacarpals as affected by age," *J. Anim. Sci.* **72**(10), 2617-2623 (1994).

25. W. M. El Shorafa, J. P. Feaster, and E. A. Ott, "Horse metacarpal bone: Age, ash content, cortical area and failure stress interrelationships," *J. Anim Sci.* **49**(4), 979-982 (1979).

26. J. D. Currey, "How well are bones designed to resist fracture?," *J. Bone Miner. Res.* **18**(4), 591-598 (2003).

27. J. A. L. Calbet, J. S. Moysi, C. Dorado, and L. P. Rodríguez, "Bone mineral content and density in professional tennis players," *Calcif. Tissue Int.* **62**(6), 491-496 (1998).

28. J. Sanchis-Moysi, C. Dorado, H. Olmedillas, J. A. Serrano-Sanchez, and J. A. L. Calbet, "Bone mass in prepubertal tennis players," *Int. J. Sports Med.* **31**(6), 416-420 (2010).

29. D. H. Kohn, N. D. Sahar, J. M. Wallace, K. Golcuk, and M. D. Morris, "Exercise alters mineral and matrix composition in the absence of adding new bone," *Cells Tissues Organs* **189**(1-4), 33-37 (2009).

30. J. Wallace, K. Golcuk, M. Morris, and D. Kohn, "Inbred strain-specific effects of exercise in wild type and biglycan deficient mice," *Ann. Biomed. Eng.* **38**(4), 1607-1617 (2010).

31. M. A. Harrast and D. Colonno, "Stress fractures in runners," *Clin. Sports Med.* **29**(3), 399-416 (2010).

32. B. H. Jones, M. W. Bovee, J. M. Harris, and D. N. Cowan, "Intrinsic risk factors for exercise-related injuries among male and female army trainees," *Am. J. Sports Med.* **21**(5), 705-710 (1993).

33. J. M. Lappe, M. R. Stegman, and R. R. Recker, "The impact of lifestyle factors on stress fractures in female army recruits," *Osteoporos. Int.* **12**(1), 35-42 (2001).

34. D. M. Nunamaker, D. M. Butterweck, and M. T. Provost, "Fatigue fractures in thoroughbred racehorses: Relationships with age, peak bone strain, and training," *J. Orthop. Res.* **8**(4), 604-611 (1990).

35. G. L. Norwood, "The bucked shin complex in thoroughbreds," in Proceedings of the 24th Annual Convention of the American Association of Equine Practitioners, pp. 319-336 (1978).

36. G. C. Reilly, J. D. Currey, and A. E. Goodship, "Exercise of young thoroughbred horses increases impact strength of the third metacarpal bone," *J. Orthop. Res.* **15**(6), 862-868 (1997).

37. D. M. Nunamaker, D. M. Butterweck, and M. T. Provost, "Some geometric properties of the third metacarpal bone: A comparison between the Thoroughbred and Standardbred racehorse," *J. Biomech.* **22**(2), 129-134 (1989).

38. R. C. Murray, S. Vedi, H. L. Birch, K. H. Lakhani, and A. E. Goodship, "Subchondral bone thickness, hardness and remodelling are influenced by short-term exercise in a site-specific manner," *J. Orthop. Res.* **19**(6), 1035-1042 (2001).

39. P. Muir, J. McCarthy, C. L. Radtke, M. D. Markel, E. M. Santschi, M. C. Scollay, and V. L. Kalscheur, "Role of endochondral ossification of articular cartilage and functional adaptation of the subchondral plate in the development of fatigue microcracking of joints," *Bone* **38**(3), 342-349 (2006).

40. P. Muir, private communication.

41. F. W. L. Esmonde-White, M. V. Schulmerich, K. A. Esmonde-White, and M. D. Morris, "Automated Raman spectral preprocessing of bone and other musculoskeletal tissues," *Proc. SPIE* **7166**(1), 716605 (2009).

42. G. Penel, C. Delfosse, M. Descamps, and G. Leroy, "Composition of bone and apatitic biomaterials as revealed by intravital Raman microspectroscopy," *Bone* **36**(5), 893-901 (2005).

43. A. Boskey and R. Mendelsohn, "Infrared analysis of bone in health and disease," *J. Biomed. Opt.* **10**(3), 031102 (2005).

44. D. Pienkowski, T. M. Doers, M.-C. Monier-Faugere, Z. Geng, N. P. Camacho, A. L. Boskey, and H. H. Malluche, "Calcitonin alters bone quality in beagle dogs," *J. Bone Miner. Res.* **12**(11), 1936-1943 (1997).

45. A. Wittich, C. A. Mautalen, M. B. Oliveri, A. Bagur, F. Somoza, and E. Rotemberg, "Professional football (soccer) players have a markedly greater skeletal mineral content, density and size than age- and BMI-matched controls," *Calcif. Tissue Int.* **63**(2), 112-117 (1998).

46. A. Heinonen, H. Sievänen, P. Kannus, P. Oja, M. Pasanen, and I. Vuori, "High-impact exercise and bones of growing girls: A 9-month controlled trial," *Osteoporos. Int.* **11**(12), 1010-1017 (2000).

47. T. H. Huang, S. C. Lin, F. L. Chang, S. S. Hsieh, S. H. Liu, and R. S. Yang, "Effects of different exercise modes on mineralization, structure, and biomechanical properties of growing bone," *J. Appl. Physiol.* **95**(1), 300-307 (2003).

48. A. Boyde and E. C. Firth, "High resolution microscopic survey of third metacarpal articular calcified cartilage and subchondral bone in the juvenile horse:

Possible implications in chondro-osseous disease," *Microsc. Res. Tech.* **71**(6), 477-488 (2008).

49. T. M. Da Costa Gómez, J. G. Barrett, S. J. Sample, C. L. Radtke, V. L. Kalscheur, Y. Lu, M. D. Markel, E. M. Santschi, M. C. Scollay, and P. Muir, "Up-regulation of site-specific remodeling without accumulation of microcracking and loss of osteocytes," *Bone* **37**(1), 16-24 (2005).

CHAPTER III

THE ROLE OF SPROUTY2 ON BONE COMPOSITION IN NORMAL BONE DEVELOPMENT

1 Introduction

Genetically-modified mice have contributed substantially to scientific knowledge. They can be models of human diseases or enable study of the physiological roles of genes through the addition, deletion, or alteration of gene products.[1, 2] For example, some studies using genetically-modified mice have tried to link muscle lipid accumulation with impaired insulin signaling.[3] Lipid intermediates like diacylglycerol and ceramides were overexpressed and the susceptibility to insulin resistance was monitored. In another study, mice in which the nicotinic acetylcholine receptor subunits in the brain had been deleted were used to study drug addiction.[4] Genetically-modified mice have also been used as models for various types of cancer, including lung, breast, and pancreatic cancer.[5]

One gene that influences the development of many types of tissues, including bone, is Sprouty (Spry). There are four mouse Spry genes (Spry 1, 2, 3, and 4), and all have human orthologs.[6] Spry genes are inhibitors of the Receptor Tyrosine Kinase (RTK) signaling pathway.[7-9] RTK signaling regulates proliferation, survival, and differentiation of cells during embryonic development, including development of the brain, lung, tooth,

bone, and many other organs.[10] In a loss-of-function study where Spry2 was inactivated ($Spry2^{-/-}$), hearing loss was observed in $Spry2^{-/-}$ mice due to a postnatal cell fate transformation in the auditory organ of the inner ear.[11] Another study showed $Spry1^{-/-}$ mice displayed kidney and urinary tract defects due to development of supernumerary ureteric buds.[12] In addition to regulating RTK signaling during normal development, Spry genes are also involved in the pathogenesis of disease. Spry protein levels have been shown to be down- or up-regulated in a number of cancers and in cardiovascular and other disease.[13]

Spry genes also regulate tooth and bone development. In $Spry2^{-/-}$ mice and $Spry4^{-/-}$ mice, an extra tooth usually forms in the normally toothless gap between the molars and incisors.[14] In $Spry4^{-/-}$ mice where one Spry2 allele is inactivated ($Spry2^{+/-}$), abrasion of incisors is prevented by deposition of enamel on both sides of the tooth, resulting in incisors that are elongated and tusk-like.[15, 16] In bone studies, overexpression of Spry2 in the chick limb led to inhibition of cartilage cell differentiation and a decrease in limb growth.[6] Another study determined that three of the Spry genes (Spry1, Spry2, and Spry4) were expressed in bone.[17] When these genes were inactivated ($Spry1^{-/-}$, $Spry2^{-/-}$, and $Spry4^{-/-}$), only $Spry2^{-/-}$ mice had shorter long bones, smaller bone volume, and a lower body weight than wild-type (WT) littermates. This suggests that Spry2 plays a role in the accrual and maintenance of bone mass. The objective of this study was to examine how the Spry2 gene affects bone composition in normal bone development. To accomplish this, tibiae from $Spry2^{-/-}$ mice and WT mice were examined using Raman spectroscopy.

2 Materials and methods

2.1 Specimen preparation

Left tibiae were excised from three Spry2$^{-/-}$ mice and three WT mice. All specimens were obtained from 6-week-old male mice. The distal end of each tibia was potted in a small brass block using a low-melting-point lead alloy. This potting material sets in less than one minute and does not cause thermal denaturation of collagen. The exposed end of the tibia was then cut at the tibia-fibula junction using a low-speed precision saw (IsoMet, Buehler Ltd., Lake Bluff, IL). The tibia was cut at this junction because collaborators had taken μCT measurements of the cortical bone at this point for other specimens. The exposed cross-section of the tibia was then wrapped in phosphate-buffer-soaked gauze and stored at -20°C until Raman measurements were acquired.

2.2 Raman measurements

A locally constructed Raman microprobe, described previously,[18] with a line-focused laser beam was used for data acquisition. Briefly, a 20x/0.75 NA objective (S Fluor, Nikon Instruments, Inc., Melville, NY) focused a 400-mW 785-nm diode laser (Invictus, Kaiser Optical Systems, Inc., Ann Arbor, MI) onto the specimen. Raman scatter was collected through the same objective and focused into a NIR-optimized spectrograph (HoloSpec f/1.8, Kaiser Optical Systems, Inc.) equipped with a 50-μm slit to provide spectral resolution of 6-8 cm^{-1}. The detector was a thermoelectrically cooled charge-coupled device (CCD) camera (DV420A-OE-133, Andor Technology, South Windsor, CT) operating at -75 °C. The line focus enabled the simultaneous collection of

255 spectra, or one for each pixel row along the spatial dimension of the CCD. Spectra collected along a line in this way are called a transect. Transects were acquired using an integration time of 180 s. The laser power at the specimen was ~ 115 mW. The mounted specimens were placed on a rotation stage to better facilitate the acquisition of data from quadrants of the bone cross-section. Transects were acquired from the tibial cross-section in the anterior-lateral (AL), anterior-medial (AM), posterior-lateral (PL), and posterior-medial (PM) quadrants. In each quadrant, two transects were acquired, one at the mid-cortex and one near the periosteal edge of the bone. Figure 3.1 shows the approximate locations of transects with respect to the specimen geometry. During all Raman measurements, specimens were kept hydrated in PBS buffer.

2.3 Data Analysis

All data reduction was performed in MATLAB (The Mathworks, Inc., Natick, MA) using vendor-supplied and locally written scripts. Preprocessing included removal of noise spikes, subtraction of dark current, image rotation and slit image curvature correction,[19] correction for the wavelength response of the CCD, and wavenumber calibration. The data for each acquisition consisted of an array of 255 Raman spectra, the number of pixel rows along the spatial dimension of the CCD (i.e. slit height). Data processing was only carried out for the active region of the chip: the spectral region was truncated from 359-1914 cm^{-1} and the spatial dimension was truncated from 70-180 pixels. The average spectrum for each transect was calculated, and then that averaged spectrum was imported into GRAMS/AI (Thermo Galactic, Madison, WI). Spectra were baselined in GRAMS using a multi-point baseline, where connecting lines through selected points were subtracted from the trace. The minimum point in each spectrum was

set to zero, and then spectra were normalized to the phosphate ν_1 band. The spectra were baselined such that the edges of each band that was subsequently peakfit was below 0.005 intensity counts. The carbonate ν_1 and amide I region were fit for peak heights and areas using mixed Gaussian and Lorentzian polynomials. The areas under the curve for the phosphate ν_1, phosphate ν_2, phosphate ν_4, and proline-hydroxyproline (pro-hyp) regions were integrated. The selected wavenumber regions used for peak fitting/integration were: 902-993 cm^{-1} for phosphate ν_1, 367-502 cm^{-1} for phosphate ν_2, 503-655 cm^{-1} for phosphate ν_4, 832-901 cm^{-1} for pro-hyp, 1015-1118 cm^{-1} for carbonate ν_1, and 1608-1716 cm^{-1} for amide I. Band height and area ratios were calculated, including the mineral-to-matrix, carbonate-to-phosphate, and collagen cross-link ratios. The mineral-to-matrix ratio was calculated three different ways. The mineral band used was either the phosphate ν_1, ν_2, or ν_4 band. The matrix band used was always the pro-hyp band. The carbonate-to-phosphate ratio was computed as 1070-to-960. The collagen cross-link ratio was calculated as 1685-to-1665, the wavenumber positions of two amide I band components. Crystallinity was also calculated as the inverse full-width-half-maximum of the phosphate ν_1 band.

One-way ANOVAs were used to examine the effect of group (WT vs. $Spry2^{-/-}$), cortical site (mid-cortex or periosteal edge), and quadrant (AL, AM, PL, PM) using a significance value of 0.05.

3 Results

The overall group differences between $Spry2^{-/-}$ and WT mice are shown in Figure 3.2. The data from the four quadrants and two cortical sites were pooled for each

specimen in order to examine the overall differences between the two groups. Each bar represents the average value for the three Spry2$^{-/-}$ or three WT mice. The band height and area ratios were similar, so only the area ratios are shown in the figure. A significant difference was seen in the collagen cross-link ratio between Spry2$^{-/-}$ and WT mice ($p<0.05$). The mineral-to-matrix ratios showed a trend toward having a lower mineral-to-matrix ratio in the Spry2$^{-/-}$ mice, although the group differences were not significant. However, the group differences were close to being significant for the mineral-to-matrix ratios calculated using phosphate ν_2 or phosphate ν_4. The p-values were 0.20 and 0.17 for the phosphate ν_2 and ν_4 area ratios and 0.16 and 0.14 for the phosphate ν_2 and ν_4 height ratios. As can be seen in Figure 3.3, the area and intensity differences between the Spry2$^{-/-}$ and WT spectra in the low wavenumber region (~400-600 cm^{-1}) are noticeable. In general, the WT spectra had higher areas/intensities in this region. The carbonate-to-phosphate ratio and crystallinity are also shown in Figure 3.2. No significant group differences were found in these two parameters.

Group differences were then examined by cortical site (i.e. all WT data at the mid-cortex vs. all Spry2$^{-/-}$ data at the mid-cortex; all WT data at the periosteal edge vs. all Spry2$^{-/-}$ data at the periosteal edge). Figure 3.4 shows there is a significant difference in the phosphate ν_4-to-matrix area ratio ($p<0.05$), and a trend to significance in the phosphate ν_2-to-matrix area ratio ($p<0.1$) and collagen cross-link area ratio ($p<0.1$) at the mid-cortex. The collagen cross-link height ratio was significant ($p<0.05$) at the mix-cortex (data not shown). No significant differences were seen between groups at the periosteal edge.

Differences between the mid-cortex and periosteal edge within WT specimens or within Spry2$^{-/-}$ specimens were also examined, but there were no significant differences. Also, no significant differences among region (AL, AM, PL, PM) within WT specimens or within Spry2$^{-/-}$ specimens were found.

4 Discussion

Overall, Spry2$^{-/-}$ and WT specimens were significantly different in their collagen cross-link ratio. A close examination of the spectra in the amide I region shows a more prominent shoulder band near 1685 cm^{-1} for the WT specimens. This result agrees with the larger collagen cross-link ratio (1685-to-1665) calculated for the WT specimens. In the Spry2$^{-/-}$ mice, a lower collagen cross-link ratio was observed. The 1685 cm^{-1} component has been shown to decrease with age and collagen maturity, while the 1665 cm^{-1} component increases.[20, 21] A smaller cross-link ratio is generally indicative of more mature tissue. Since all specimens were from mice 6 weeks of age, the data suggests that cross-linking is occurring earlier in the Spry2$^{-/-}$ mice.

Overall group differences (Figure 3.2) in the mineral-to-matrix ratios were not significant ($p<0.2$). However, the noticeable area/intensity differences in the phosphate ν_2 or phosphate ν_4 bands between WT and Spry2$^{-/-}$ specimens (Figure 3.3) suggests that the overall difference in the phosphate ν_2-to-matrix or phosphate ν_4-to-matrix ratios may be found to be significant if more specimens are examined. Greater differences between groups were seen in the mineral-to-matrix ratios calculated using phosphate ν_2 or phosphate ν_4, rather than phosphate ν_1. In Spry2$^{-/-}$ spectra, the phosphate ν_2 and phosphate ν_4 areas were on average 9% lower and the pro-hyp areas were on average

10% higher than WT spectra in the same regions. Presumably, the mineral-to-matrix ratios calculated with phosphate ν_1, ν_2, and ν_4 should have the same percentage differences between the groups. The reason why there is less of a difference in the mineral-to-matrix ratio between groups when using phosphate ν_1 in the ratio calculation is likely due to differences in mineral orientation across the cross-section of the tibia. The intensity of the phosphate ν_1 band, due to the phosphate symmetric stretch, is sensitive to the polarization direction of the laser and to the orientation of the mineral. The long axis of the mineral is aligned parallel to the long axis of the collagen fibrils.[22-25] Phosphate ν_2 and ν_4 are less sensitive to orientation effects because each band consists of multiple vibration modes. In this study, the laser output was linearly polarized, and transects were collected in the four quadrants of the tibial cross-section. Another study of murine femoral cortical bone at the mid-diaphysis showed the orientation of collagen fibrils across the cross-section was not consistent.[26]

Fratzl and colleagues have examined transverse cross-sections of osteonal bone[27, 28] and showed that the intensity of phosphate ν_1 differed depending upon orientation of collagen fibrils relative to the polarization direction of exciting laser light. If the orientation of the fibrils was not parallel to the laser polarization, then the intensity of phosphate ν_1 was decreased. The intensities of phosphate ν_2 and phosphate ν_4 were shown to be fairly constant. For this study on Spry2$^{-/-}$ mice, the mineral-to-matrix ratios calculated with phosphate ν_2 or ν_4 are likely to be more accurate than the mineral-to-matrix ratio calculated with phosphate ν_1 because phosphate ν_2 and ν_4 are less sensitive to orientation effects. The lower mineral-to-matrix ratios calculated for the Spry2$^{-/-}$ specimens are consistent with results of collaborators who have shown that

Spry2$^{-/-}$ mice have undermineralized skeletons.[29] For future studies where the orientation of collagen fibrils and the mineral is expected to vary spatially at different measurement locations, the use of a depolarizer in the path of the excitation light would minimize orientation effects seen in the spectra.

The overall differences in the band intensity ratios were mainly due to differences at the mid-cortex. Significant ($p<0.05$) differences in the phosphate ν_4-to-matrix area ratio or nearly significant ($p<0.1$) differences in the phosphate ν_2-to-matrix and collagen cross-link area ratios were found at the mid-cortex. At the periosteal edge, there were no significant differences between WT and Spry2$^{-/-}$ mice. Bone growth occurs by apposition, so new bone growth occurs at the periosteal and endosteal edges of the bone.[30, 31] Thus, tissue near the mid-cortex is generally older than tissue at the periosteal edge.

In general, the mineral-to-matrix ratio increases with age.[32, 33] The mineral-to-matrix ratio across the tibial cross-section in the wild-type specimens was consistent with this trend. The average mineral-to-matrix ratio (phosphate ν_4/pro-hyp) for WT specimens was 4.57±0.33 for the periosteal edge and 4.76±0.24 for the mid-cortex. For Spry2$^{-/-}$ specimens, the average mineral-to-matrix ratio was approximately constant across the cross-section: 3.90±0.71 for the periosteal edge and 3.83±0.41 for the mid-cortex. The data suggest that the differences in the mineral-to-matrix and collagen cross-link ratios are site-specific in the tibial cross-section, and may be more likely to arise in older tissue.

5 Conclusion

The data suggests that the Spry2 gene influences the areas and intensities of both mineral and matrix Raman bands. Overall group differences included a significant difference in the collagen cross-link area ratio. Differences between the Spry2$^{-/-}$ and WT specimens were mainly due to differences at the mid-cortex, a site in cortical bone where, in general, the average tissue age is older than the periosteal edge of the bone. The lower cross-link ratio found in Spry2$^{-/-}$ specimens suggests that cross-linking is occurring earlier in those specimens. Significant differences were also found in the mineral-to-matrix area ratio at the mid-cortex (phosphate ν_4-to-matrix, $p<0.05$; phosphate ν_2-to-matrix, $p<0.1$). The lower mineral-to-matrix band ratios suggest that less mineral is present in the Spry2$^{-/-}$ specimens. Based on the observed differences in band ratios, Spry2 appears to regulate cross-link formation and accrual of mineral during normal bone development.

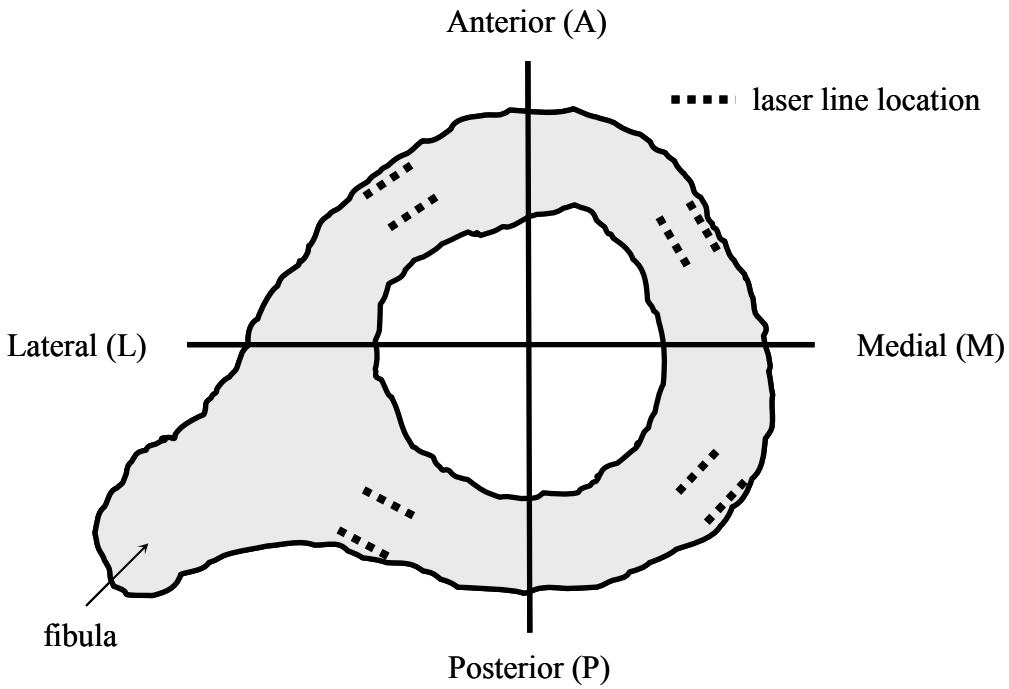

Figure 3.1. Cross-section of left tibia. Two transects were acquired in each quadrant, one at the periosteal edge and one at the mid-cortex.

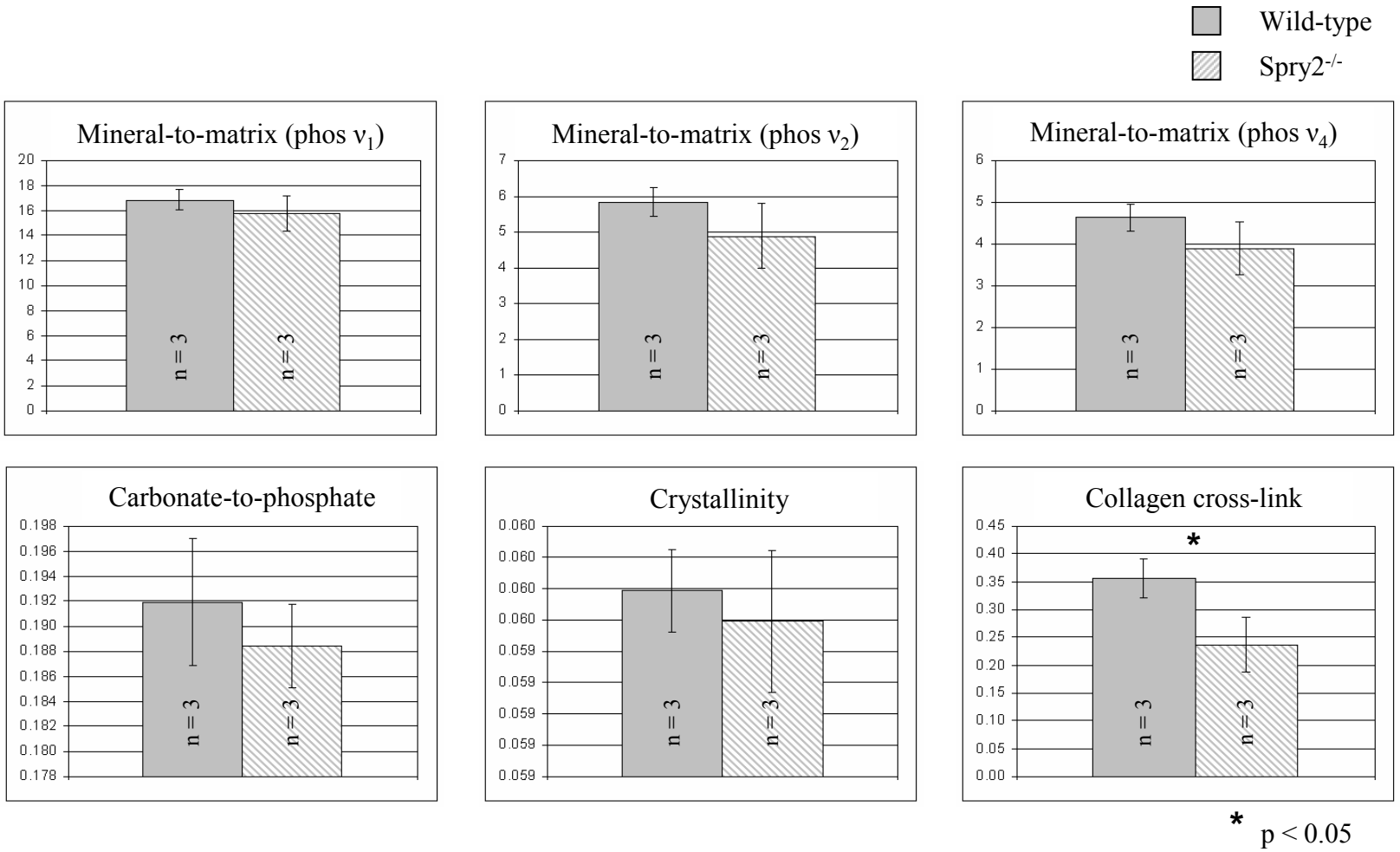

Figure 3.2. Overall group differences between Spry2$^{-/-}$ and WT mice. Area ratios are shown. The collagen cross-link ratio was significantly different between the two groups.

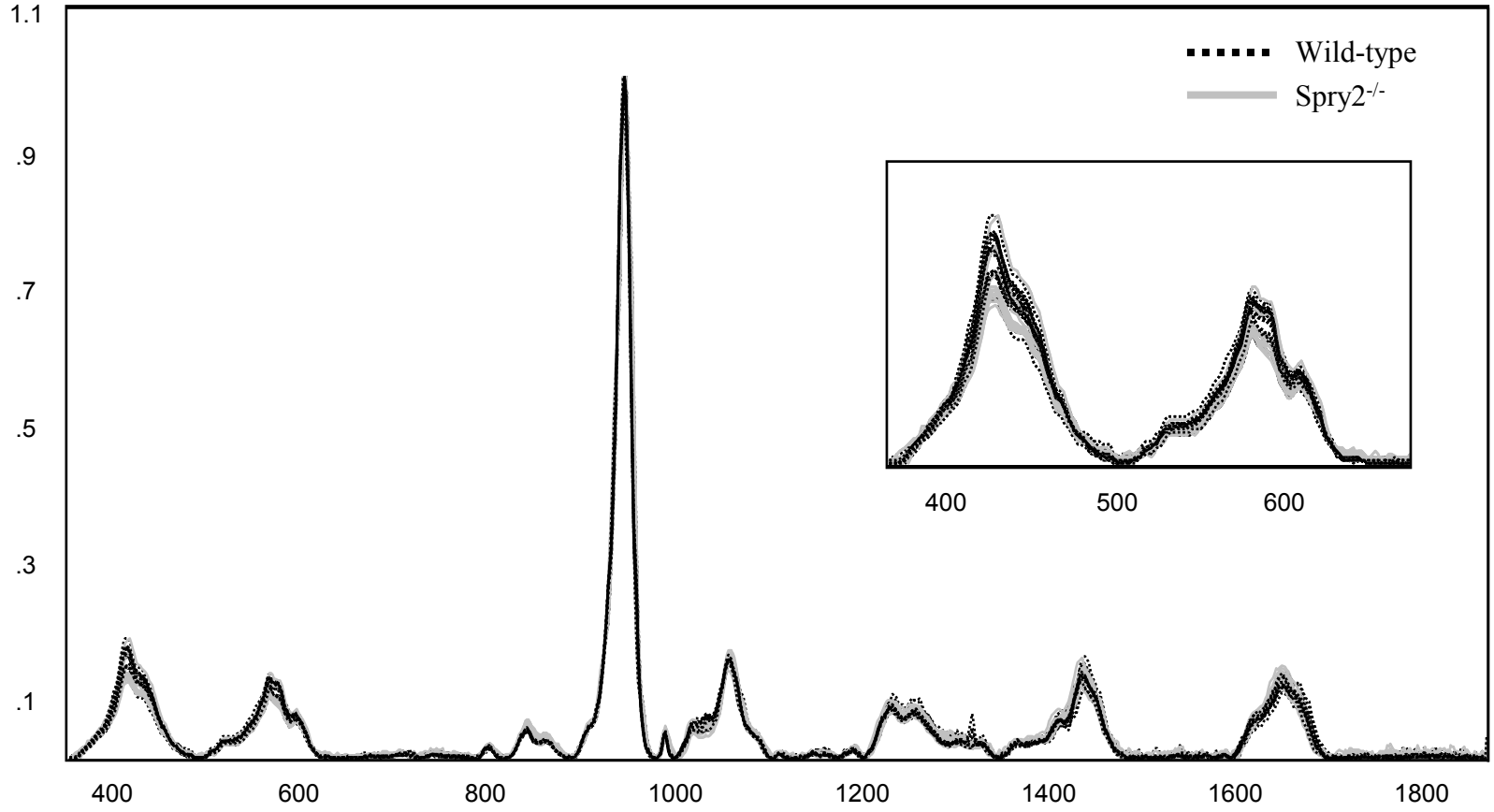

Figure 3.3. Raman spectra of Spry2$^{-/-}$ and WT mice. In general, the spectra from WT mice have higher intensities in the phosphate ν_2 and ν_4 regions, as shown in the inset.

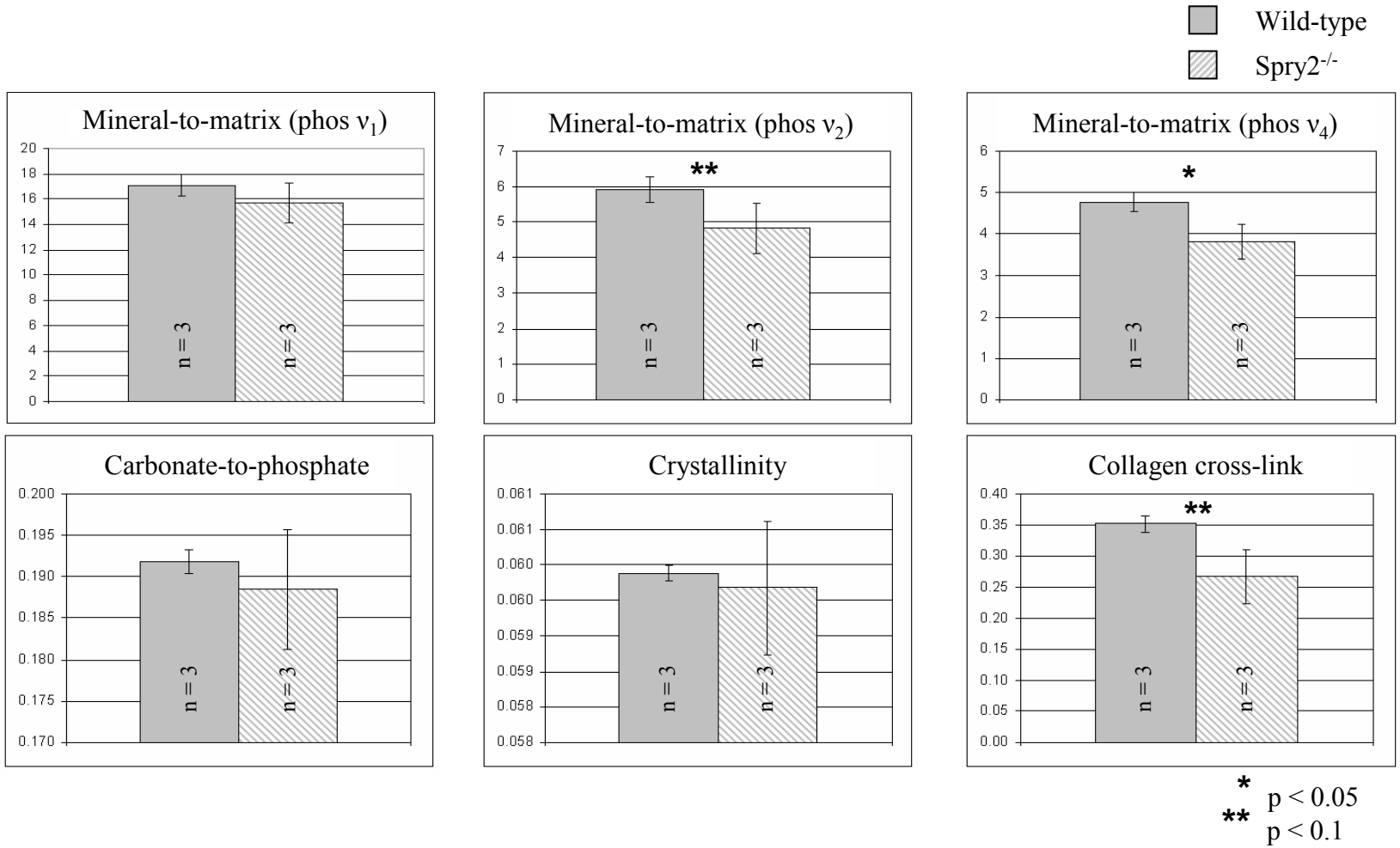

Figure 3.4. Group differences (Spry2$^{-/-}$ vs. WT) at mid-cortex. Area ratios are shown. The mineral-to-matrix ratio as calculated using phosphate ν_4 was significantly different at the mid-cortex between the two groups. The mineral-matrix ratio as calculated using phosphate ν_2 and the collagen cross-link ratio had p-values of less than 0.1.

References

1. K. Lyons, "Animal models: Genetic manipulation," in *Primer on the Metabolic Bone Diseases and Disorders of Mineral Metabolism*, C. J. Rosen, Ed., pp. 45-51, American Society for Bone and Mineral Research, Washington, D.C (2008).

2. L. M. Chaible, M. A. Corat, E. Abdelhay, and M. L. Z. Dagli, "Genetically modified animals for use in research and biotechnology," *Genet. Mol. Res.* **9**(3), 1469-1482 (2010).

3. E. W. Kraegen and G. J. Cooney, "Free fatty acids and skeletal muscle insulin resistance," *Curr. Opin. Lipidol.* **19**(3), 235-241 (2008).

4. J.-P. Changeux, "Nicotine addiction and nicotinic receptors: Lessons from genetically modified mice," *Nat. Rev. Neurosci.* **11**(6), 389-401 (2010).

5. L. Zender, J. Zuber, and S. W. Lowe, "Snapshot: Genetic mouse models of cancer," *Cell* **129**(4), 838 (2007).

6. G. Minowada, L. A. Jarvis, C. L. Chi, A. Neubuser, X. Sun, N. Hacohen, M. A. Krasnow, and G. R. Martin, "Vertebrate Sprouty genes are induced by FGF signaling and can cause chondrodysplasia when overexpressed," *Development* **126**(20), 4465-4475 (1999).

7. S. Kramer, M. Okabe, N. Hacohen, M. A. Krasnow, and Y. Hiromi, "Sprouty: a common antagonist of FGF and EGF signaling pathways in Drosophila," *Development* **126**(11), 2515-2525 (1999).

8. A. Reich, A. Sapir, and B. Shilo, "Sprouty is a general inhibitor of receptor tyrosine kinase signaling," *Development* **126**(18), 4139-4147 (1999).

9. H. J. Kim and D. Bar-Sagi, "Modulation of signalling by Sprouty: A developing story," *Nat. Rev. Molec. Cell. Biol.* **5**(6), 441-450 (2004).

10. J. M. Mason, D. J. Morrison, M. A. Basson, and J. D. Licht, "Sprouty proteins: Multifaceted negative-feedback regulatros of receptor tyrosine kinase signaling," *Trends Cell Biol.* **16**(1), 45-54 (2006).

11. K. Shim, G. Minowada, D. E. Coling, and G. R. Martin, "Sprouty2, a mouse deafness gene, regulates cell fate decisions in the auditory sensory epithelium by antagonizing FGF signaling," *Dev. Cell* **8**(4), 553-564 (2005).

12. M. A. Basson, S. Akbulut, J. Watson-Johnson, R. Simon, T. J. Carroll, R. Shakya, I. Gross, G. R. Martin, T. Lufkin, A. P. McMahon, P. D. Wilson, F. D. Costantini, I. J. Mason, and J. D. Licht, "Sprouty1 is a critical regulator of GDNF/RET-mediated kidney induction," *Dev. Cell* **8**(2), 229-239 (2005).

13. F. Edwin, K. Anderson, C. Ying, and T. B. Patel, "Intermolecular interactions of Sprouty proteins and their implications in development and disease," *Mol. Pharmacol.* **76**(4), 679-691 (2009).

14. O. D. Klein, G. Minowada, R. Peterkova, A. Kangas, B. D. Yu, H. Lesot, M. Peterka, J. Jernvall, and G. R. Martin, "Sprouty genes control diastema tooth development via bidirectional antagonism of epithelial-mesenchymal FGF signaling," *Dev. Cell* **11**(2), 181-190 (2006).

15. O. D. Klein, D. B. Lyons, G. Balooch, G. W. Marshall, M. A. Basson, M. Peterka, T. Boran, R. Peterkova, and G. R. Martin, "An FGF signaling loop sustains the generation of differentiated progeny from stem cells in mouse incisors," *Development* **135**(2), 377-385 (2008).

16. T. Boran, R. Peterkova, H. Lesot, D. B. Lyons, M. Peterka, and O. D. Klein, "Temporal analysis of ectopic enamel production in incisors from Sprouty mutant mice," *J. Exp. Zool. (Mol. Dev. Evol.)* **312B**(5), 473-485 (2009).

17. A. Joo, A. Sanders, R. Long, W. Chang, and O. Klein, "Sprouty2 regulates bone development," *J. Bone Miner. Res.* **24**(Suppl 1), http://www.asbmr.org/Meetings/AnnualMeeting/AbstractDetail.aspx?aid=85e83adff-b83d85-429d-428d445-428c405e0288915 (2009).

18. A. Carden, R. M. Rajachar, M. D. Morris, and D. H. Kohn, "Ultrastructural changes accompanying the mechanical deformation of bone tissue: A Raman imaging study," *Calcif. Tissue Int.* **72**(2), 166-175 (2003).

19. F. W. L. Esmonde-White, M. V. Schulmerich, K. A. Esmonde-White, and M. D. Morris, "Automated Raman spectral preprocessing of bone and other musculoskeletal tissues," *Proc. SPIE* **7166**(1), 716605 (2009).

20. E. P. Paschalis, K. Verdelis, S. B. Doty, A. L. Boskey, R. Mendelsohn, and M. Yamauchi, "Spectroscopic characterization of collagen cross-links in bone," *J. Bone Miner. Res.* **16**(10), 1821-1828 (2001).

21. K. Otsubo, E. P. Katz, G. L. Mechanic, and M. Yamauchi, "Cross-linking connectivity in bone collagen fibrils: The carboxy-terminal locus of free aldehyde," *Biochemistry* **31**(2), 396-402 (1992).

22. J. Moradian-Oldak, S. Weiner, L. Addadi, W. J. Landis, and W. Traub, "Electron imaging and diffraction study of individual crystals of bone, mineralized tendon and synthetic carbonate apatite," *Connect. Tissue Res.* **25**(3-4), 219-228 (1991).

23. W. J. Landis, M. J. Song, A. Leith, L. McEwen, and B. F. McEwen, "Mineral and organic matrix interaction in normally calcifying tendon visualized in three dimensions

by high-voltage electron microscopic tomography and graphic image reconstruction," *J. Struct. Biol.* **110**(1), 39-54 (1993).

24. W. J. Landis, "Tomographic imaging of collagen-mineral interaction: Implications for osteogenesis imperfecta," *Connect. Tissue Res.* **31**(4), 287-290 (1995).

25. S. Weiner and W. Traub, "Organization of hydroxyapatite crystals within collagen fibrils," *FEBS Letters* **206**(2), 262-266 (1986).

26. S. Gamsjaeger, A. Masic, P. Roschger, M. Kazanci, J. W. C. Dunlop, K. Klaushofer, E. P. Paschalis, and P. Fratzl, "Cortical bone composition and orientation as a function of animal and tissue age in mice by Raman spectroscopy," *Bone* **47**(2), 392-399 (2010).

27. M. Kazanci, P. Roschger, E. P. Paschalis, K. Klaushofer, and P. Fratzl, "Bone osteonal tissues by Raman spectral mapping: Orientation-composition," *J. Struct. Biol.* **156**(3), 489-496 (2006).

28. M. Kazanci, H. D. Wagner, N. I. Manjubala, H. S. Gupta, E. Paschalis, P. Roschger, and P. Fratzl, "Raman imaging of two orthogonal planes within cortical bone," *Bone* **41**(3), 456-461 (2007).

29. O. Klein, "The role of Spry2 in skeletogenesis," in IBMS Sun Valley Workshop, Sun Valley, ID (2009).

30. E. Seeman, P. B. John, G. R. Lawrence, and T. J. Martin, "Modeling and remodeling: The cellular machinery responsible for the gain and loss of bone's material and structural strength," in *Principles of Bone Biology*, pp. 1-28, Academic Press, San Diego (2002).

31. A. M. Parfitt, R. Travers, F. Rauch, and F. H. Glorieux, "Structural and cellular changes during bone growth in healthy children," *Bone* **27**(4), 487-494 (2000).

32. M. Grynpas, "Age and disease-related changes in the mineral of bone," *Calcif. Tissue Int.* **53**(Suppl 1), S57-S64 (1993).

33. E. P. Paschalis, F. Betts, E. DiCarlo, R. Mendelsohn, and A. L. Boskey, "FTIR microspectroscopic analysis of normal human cortical and trabecular bone," *Calcif. Tissue Int.* **61**(6), 480-486 (1997).

CHAPTER IV

COMPARISON OF MOLECULAR ORIENTATION IN FEMORAL CORTICAL BONE FROM WILD-TYPE AND BRITTLE MICE USING POLARIZED RAMAN SPECTROSCOPY

1 Introduction

Polarized Raman spectroscopy can report on the microstructure and degree of alignment of both inorganic and organic components of a material. It has been used to study the molecular orientation in synthetic polymers including polyethylene and poly(ethylene terephthalate)[1, 2] and biological polymers like spider silk[3] and a filamentous virus.[4] The structure of polymers is important because their chemical and physical properties are affected by molecular orientation. Polarized Raman spectroscopy may also be used for vibrational mode assignments. For example, the technique has been used to determine the symmetry of vibrational modes in hydroxyapatite crystals[5] and human tooth enamel.[6]

Another mineralized tissue that has been examined with polarized Raman spectroscopy is bone. Two bone Raman bands that are commonly studied include phosphate ν_1 (P-O symmetric stretch) and amide I (carbonyl stretch, C=O) because they report on the orientation of bone mineral and the collagenous matrix, respectively.[7-9] At

the outer cortical surface of long bones, collagen fibers are aligned preferentially parallel to the long axis of the bone.[10-12] The carbonated apatite crystals are aligned with their longest dimension, the c-axis, parallel to the long axis of the collagen fibrils.[13-16] The molecular organization of bone tissue provides that Raman scattering from the C=O stretch or P-O stretch are more intense along a particular direction. Because the carbonyl groups are oriented perpendicular to the collagen backbone,[3, 7] amide I Raman scattering is more intense perpendicular to the long axis of the collagen fibrils/bone (see Figure 4.1). Whereas for phosphate, the c-axis of the mineral crystals is aligned along the long axis of the collagen fibrils, and thus phosphate ν_1 Raman scattering is more intense parallel to the long axis of the bone. The Raman intensities of hydroxyapatite bands have been shown to be dependent on the c-axis orientation, and changes in band intensity reflect changes in the c-axis orientation.[5] Hence, when light is polarized perpendicular or parallel to the collagen fibrils, information about the orientation of bone matrix and mineral can be gathered.

A common metric reported for polarized Raman measurements is the depolarization ratio (ρ). It is a measure of the polarization direction dependence of the Raman scattering, and is measured experimentally by $\rho = I_{\perp}/I_{\parallel}$.[1] $I_{\perp}$ and $I_{\parallel}$ are the Raman scattering intensities when the polarization direction of the collected light is perpendicular (cross-polarized) or parallel (co-polarized), respectively, to the polarization direction of the excitation light. For solutions where molecules are randomly oriented, the depolarization ratio depends mainly on vibrational symmetry. In structured solids, the molecular alignment also influences the depolarization ratio. Thus, the depolarization ratio can provide information about the orientation of components in bone tissue. From

polarized Raman theory, the depolarization ratio for a vibrational mode in nonresonance Raman scattering should have a value in the range ρ = 0-0.75.[17] If ρ = 0.75, the corresponding vibrational mode is depolarized and if ρ = 0 to <0.75, then the mode is polarized. Although the value of ρ can approach 0.75 for a polarized band, the value is typically in the range ρ = 0.01-0.3. For a structured solid like bone, a ρ value close to zero indicates the vibration is highly symmetric and also highly ordered along the axis of observation.

Polarized Raman spectroscopy can be useful in monitoring changes in tissue organization that arise with disease. For example, polarized Raman spectroscopy has been used for the detection of early dental caries on extracted human teeth.[18] The phosphate ν_1 band was monitored in both sound enamel and carious lesions. Sound enamel had a mean ρ_{959} = 0.10 and carious lesions had a mean ρ_{959} = 0.40. The larger ratio for carious lesions was attributed to increased elastic scattering within the lesion (which can depolarize the light) and a change in hydroxyapatite crystal orientation due to demineralization.

One bone disease that affects the organization and structure of collagen is osteogenesis imperfecta (OI). OI is a family of genetic disorders that affect production of type I collagen because of mutations in the COL1A1 or COL1A2 genes that encode the α1(I) and α2(I) chains of the collagen molecule.[19] The disorders are characterized by bone fragility and fractures, skeletal deformities, and poor hearing. The Brittle IV (Brtl) mouse is a model for the moderately severe type IV OI, and its defect mimics the defect seen in human patients. In the mouse model, a cysteine substitutes for glycine at position 349, a region in the triple helical domain of type I collagen.[20] Cysteine is a bulkier amino

acid and its larger size prevents proper folding of the collagen triple helix. This point substitution results in mice that have an undermineralized skeleton, skeletal deformities, disorganized trabeculae in their long bones, and are smaller with respect to WT controls.[21]

Because the amino acid point substitution prevents proper folding of the triple helix, some of the collagen is likely distorted. This would presumably affect the orientation of the mineral considering it is deposited in and around the collagen fibrils. Hence, the objective of this study was to use polarized Raman spectroscopy to determine any differences in the orientation of bone mineral and bone collagen between WT and Brtl mice.

2 Materials and methods

2.1 Specimen preparation

Left femora were excised from four wild-type (WT) and four Brtl heterozygous mice ($Brtl^{+/-}$). All specimens were obtained from female mice that were between 3 and 4 months of age. The epiphyses were removed, and the bone marrow was flushed from the mid-diaphysis with phosphate-buffered saline (PBS). The femora were then wrapped in phosphate-buffer-soaked gauze and stored at -20°C until Raman measurements were acquired.

2.2 Polarized Raman measurements

A locally constructed Raman microprobe, with a line-focused laser beam was used for data acquisition. A schematic of the microprobe is shown in Figure 4.2. A

400-mW 785-nm diode laser (Invictus, Kaiser Optical Systems, Inc., Ann Arbor, MI) was focused onto the specimen through a Nikon E600 microscope and 40x/0.90 NA objective (S Fluor, Nikon Instruments, Inc., Melville, NY). Raghavan and co-workers showed that a high numerical aperture (NA) is needed for polarization measurements in tissue in order to eliminate artifacts from multiple elastic light scattering.[22] A half-wave plate (WPMH05M-780, Thorlabs, Inc., Newton, NJ) was used to select the polarization direction of the excitation laser light. Raman scatter was collected through the same objective and directed through a polarization analyzer (LPNIR050, Thorlabs, Inc.) which selected the parallel or perpendicular polarization component. A depolarizer (DPU-25-B, Thorlabs, Inc.) eliminated intensity artifacts caused by the polarization dependence of the spectrograph grating.[23] The collected light was then focused into a NIR-optimized spectrograph (HoloSpec f/1.8, Kaiser Optical Systems, Inc.) equipped with a 25-μm slit to provide spectral resolution of 3-4 cm^{-1}. The detector was a thermoelectrically cooled charge-coupled device (CCD) camera (DU401A-BR-DD, Andor Technology, South Windsor, CT) operating at -75 °C.

The line focus enabled the simultaneous collection of 255 spectra, or one for each pixel row along the spatial dimension of the CCD. Spectra collected along a line in this way are called a transect. Transects were acquired using an integration time of 300 s. The laser power at the specimen was ~ 50 mW. The specimens were placed in a small Petri dish on a piece of gauze wet with PBS to prevent dehydration. During all Raman measurements, specimens were kept hydrated with PBS. Transects were acquired at five locations along the femoral mid-diaphysis for each specimen. For these measurements, the polarization of the excitation laser light was always oriented parallel to the long axis

of the femora. At each location, the analyzer was positioned to collect the parallel (co-polarized) or perpendicular (cross-polarized) component of the Raman-scattered light.

In order to measure the polarization dependence of the Raman spectra of WT or Brtl femora, a series of measurements was acquired at a sixth location along the mid-diaphysis where the polarization direction of the excitation light was at different angles relative to the polarization direction of the collected light. For these measurements, the specimen orientation and analyzer position were kept stationary, but the half-wave plate was rotated. Transects were collected when the half-wave plate was oriented at 0°, 20°, 40°, 60°, 80°, and 90° relative to the position of the analyzer.

2.3 Data Analysis

All data reduction was performed in MATLAB (The Mathworks, Inc., Natick, MA) using vendor-supplied and locally written scripts. Preprocessing included removal of noise spikes, subtraction of dark current, correction for image rotation (caused by slight misalignment of camera axis to dispersion axis) and slit image curvature (caused by the large gathering angle of the spectrograph),[24] correction for the wavelength response of the CCD, and wavenumber calibration. The wavenumber calibration procedure converted the CCD pixel axis into wavenumbers and was accomplished by measuring the emission lines of a neon discharge lamp. Data were truncated along the spectral axis from 276-1923 cm^{-1}. The average spectrum for each transect was calculated, and then the averaged spectrum was imported into GRAMS/AI (Thermo Galactic, Madison, WI).

In GRAMS, spectra were truncated in the phosphate ν_1 region from 735-1150 cm^{-1} and in the amide I region from 1500-1800 cm^{-1}. Both regions were subsequently baselined using a multi-point baseline, where connecting lines through selected points were subtracted from the trace. The minimum point in each spectrum was set to zero. The spectra were baselined such that the edges of the phosphate ν_1 band or amide I band were below 2 intensity counts. Peak fitting was performed using mixed Gaussian and Lorentzian polynomials. The selected wavenumber region used for peak fitting was 902-993 cm^{-1} for phosphate ν_1 and 1592-1721 cm^{-1} for amide I. Band heights of the phosphate ν_1 component at ~959 cm^{-1} and the amide I component at ~1663 cm^{-1} were used to calculate the depolarization ratios because band heights are usually less susceptible to errors from baselining than are band areas. The depolarization ratios ($\rho_{959} = I_{959(\perp)}/ I_{959(\parallel)}$ and $\rho_{1663} = I_{1663(\perp)}/I_{1663(\parallel)}$) for the five locations measured on each specimen were calculated, where $I_\perp$ is the intensity of the cross-polarized component for phosphate ν_1 or amide I, and $I_\parallel$ is the intensity of the co-polarized component for phosphate ν_1 or amide I.

The depolarization intensity ratios were corrected for the polarization dependence of the optics by calibration against the isotropic sample cyclohexane. The correction factor was determined experimentally by calculating the depolarization ratio for six different cyclohexane bands and comparing the experimental values to the published depolarization ratios for cyclohexane.[25] The five depolarization ratios for each specimen were averaged. The effect of genotype (WT vs. Brtl) on the average depolarization intensity ratios was tested using two-tailed unpaired t-tests and a significance value of 0.05.

3 Results

The average depolarization ratios (ρ_{959} and ρ_{1663}) from the five locations on each specimen are shown in Table 4.1. The values are grouped by genotype and specimen age. The overall differences in ρ_{959} between the genotypes are depicted pictorally in the bar graph of Figure 4.3a. The solid gray bars represent WT mice and the striped bars represent Brtl mice. Each bar is the average depolarization ratio of the four specimen means. The depolarization ratio for phosphate ν_1 was not significantly different between the four WT and four Brtl specimens. However, if only the 13-week-old specimens were examined (2 WT mice and 2 Brtl mice), a significant difference was found between WT and Brtl, as shown in Figure 4.4a. The depolarization ratio for phosphate ν_1 for the Brtl 13-week-old specimens was significantly lower (over 35%) than ρ_{959} for the age-matched WT counterparts.

The overall differences in ρ_{1663} for the four WT and four Brtl specimens are shown in Figure 4.5a. No significant differences in this ratio were found between the two genotypes when all specimens were compared. There was also no significant difference between ρ_{1663} from specimens that were 13 weeks of age (bar graph not shown).

The dependence of Raman band intensities on laser polarization was determined when the angle between the incident laser polarization and analyzer position was changed. Figure 4.3b and 4.4b plot the normalized intensities of the phosphate ν_1 band as a function of angle. In the plots, the 959 cm^{-1} band intensity at each angle was normalized to the intensity of the band at angle = 0°. Each data point represents the average intensity from all four WT or Brtl specimens (Figure 4.3b) or from the two 13-week-old WT or Brtl specimens (Figure 4.4b). The plots for the 13-week-old specimens and all four

specimens were essentially identical. No significant differences in the phosphate ν_1 band intensity were present at any angle between WT and Brtl specimens. The 959 cm^{-1} band intensity decreased from a value of 1 at 0° degrees to ~0.15 when the angle was 90°.

The dependence of the amide I band intensity between WT and Brtl spectra is shown in Figure 4.5b. As with phosphate ν_1, the 1663 cm^{-1} band intensity at each angle was normalized to the band intensity at 0°, and every data point was the average intensity from all four WT or Brtl specimens. The only significant difference in amide I band intensity between WT and Brtl mice existed at 90 degrees, where the Brtl mice showed slightly lower sensitivity toward the polarization state of the laser, as indicated by a higher amide I intensity.

4 Discussion

The depolarization ratio for phosphate ν_1 was significantly lower for Brtl specimens at 13 weeks of age. The lower ratio for Brtl mice indicates the phosphate ν_1 band is more sensitive to polarization in these specimens. It is also suggestive that either the mineral is more ordered in Brtl mice or there is less elastic light scattering in the Brtl specimens. Because the Gly349Cys point substitution disrupts the coiling of the collagen triple helix in the Brtl specimens, it seems unlikely that the mineral is more ordered. In fact, small-angle x-ray scattering has shown that mineral crystals were less well aligned in oim mice, another murine model for OI in which mice lack the α2(I) chain of type I collagen.[26] The depolarization ratio may be lower for Brtl mice because there is less multiple light scattering in these specimens due to an increased spacing between collagen

fibrils. Computational studies have been performed on a reference collagen molecule that consisted of three identical chains of Gly-Pro-Hyp triplets.[27] The authors investigated the effects of seven different amino acid substitutions, including a cysteine replacement, for a glycine in the reference molecule. For all of the mutated peptides, they found that intermolecular adhesion was reduced and intermolecular spacing was increased in the collagen fibrils. Experimental studies have shown similar results in oim mice. Reduced packing of collagen molecules within a fibril has been observed[28] and attributed to the presence of more water in oim fibers.[29]

The process of multiple light scattering in tissue can depolarize the light (with enough scattering events). Hence, a larger spacing between collagen fibrils causes less multiple light scattering and thus less depolarization of the light. Less depolarization of the light in Brtl mice could result in the lower depolarization ratio that was observed in these specimens.

Even though the difference in ρ_{959} for 13-week-old specimens may not be due to a difference in mineral orientation, a difference was still detected. However, there was no detectable difference between genotypes in the older specimens at 15 weeks of age (WT) and 17 weeks of age (Brtl). The difference detected in the 13-week-old specimens may not be real, but instead may be a consequence of the small sample size. For WT mice, two specimens at 13 weeks and two specimens at 15 weeks of age were available for study. Similarly for Brtl mice, two specimens at ages 13 and 17 weeks were examined.

Presumably, if a difference exists between genotypes in the depolarization ratio for phosphate ν_1, then a difference should also be present in the amide I depolarization ratio. However, no significant differences in ρ_{1663} were detected between WT or Brtl

specimens. One reason for this may be because the amide I spectral region has a much lower signal-to-noise ratio than the phosphate ν_1 region, and the amide I envelope is more broad than phosphate ν_1. Peak fitting a less intense, noisier, broad band like amide I leads to less reliable results than peak fitting phosphate ν_1. Accurately detecting any changes between genotypes is more difficult. Another reason that no difference in ρ_{1663} was found between genotypes may be that the polarization direction of the input laser light was parallel to the long axis of the bone, and thus, was roughly perpendicular to the carbonyl bonds in collagen (assuming collagen fibrils are parallel to the bone long axis). There is likely a smaller difference in Raman band intensities along the perpendicular direction than there would be if the laser polarization was parallel to the carbonyl bands.

In order to measure the polarization dependence of the phosphate ν_1 and amide I band for WT and Brtl mice, the polarization direction of the excitation light was rotated and aligned at different angles relative to the polarization direction of the collected light. No significant differences were found in the polarization rotation measurements for phosphate ν_1, indicating that the degree of alignment of the mineral was similar between the genotypes. This supports the notion that the significant difference in ρ_{959} for the 13-week-old specimens was likely due to a decreased amount of multiple light scattering in the Brtl specimens, rather than a difference in the orientation of the mineral.

For the polarization rotation measurements of amide I, a significant difference between the genotypes was found at 90 degrees. The average normalized intensity of the 1663 cm^{-1} band was 0.31±0.04 for WT specimens and 0.38±0.02 for Brtl specimens. Considering the depolarization ratios were very similar between the genotypes, the

significant difference at this angle may not be sustained if additional specimens are examined.

5 Conclusion

The outer cortical surface of bone tissue from WT and Brtl femora were examined with polarized Raman spectroscopy. In the outer cortex of long bones, collagen fibrils are aligned parallel to the long axis of the bone, and phosphate mineral is aligned parallel to the long axis of the collagen fibrils. Depolarization ratios of the phosphate ν_1 and amide I band were calculated and used as indicators of molecular orientation for the mineral and collagen, respectively. No significant differences in the depolarization ratio of the phosphate ν_1 or amide I band could be detected between WT and Brtl specimens. The significant difference seen in ρ_{959} for the 13-week-old specimens is likely a consequence of decreased scattering in the Brtl specimens due to a larger spacing between collagen fibrils, rather than an actual difference in the mineral orientation.

Polarization dependences of the phosphate ν_1 and amide I bands were measured by rotating the polarization direction of the laser light with respect to the collected light. The sensitivity to polarization of phosphate ν_1 and amide I was similar between WT and Brtl spectra, suggesting that there were no significant differences in the degree of mineral or collagen alignment between the genotypes.

Although no changes in orientation were detected with polarized Raman measurements, it is known that the folding of the triple helix is disrupted in Brtl mice. The Gly349Cys point substitution may have caused local, but not overall, systematic disruptions to the triple-helical folding of collagen. The data collected was averaged over

the length of the laser line. The regions probed may be an average over too large of an area to have captured this disruption.

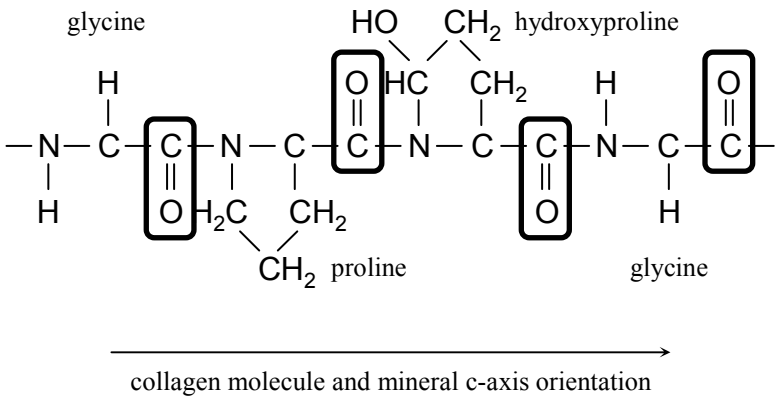

Figure 4.1. Orientation of amide I carbonyl bonds. The repeating amino-acid sequence of type I collagen is glycine-X-Y, where X and Y are often proline and hydroxyproline, respectively. The amide I mode corresponds mainly with C=O bonds, which are oriented perpendicular to the collagen backbone.

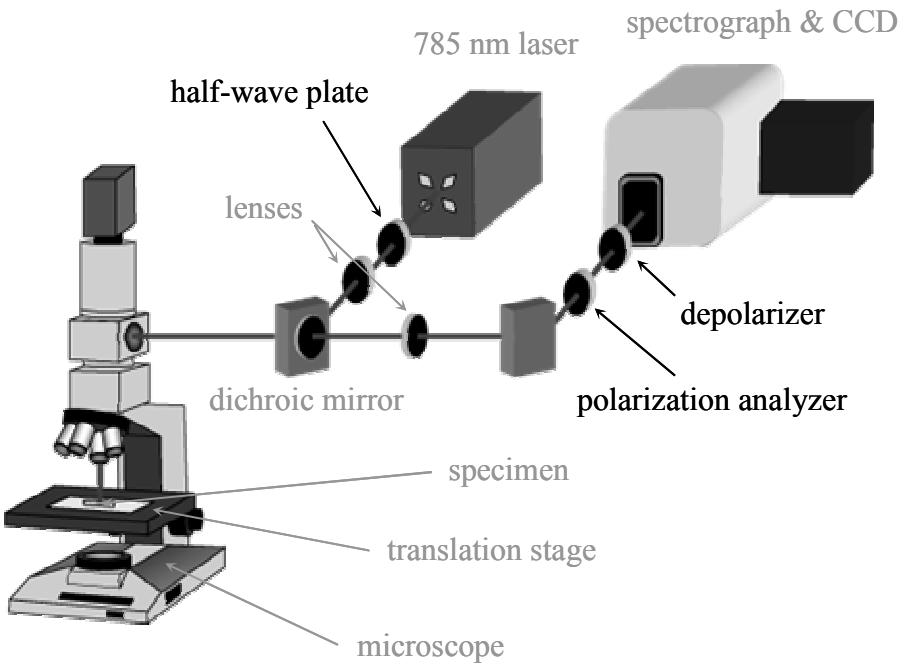

Figure 4.2. Raman microprobe used for polarization measurements. A half-wave plate rotates the plane of polarization of the laser light and the polarization analyzer selects the polarization direction of the Raman-scattered light. A depolarizer randomizes the polarization to eliminate intensity artifacts caused by the polarization dependence of the spectrograph grating.

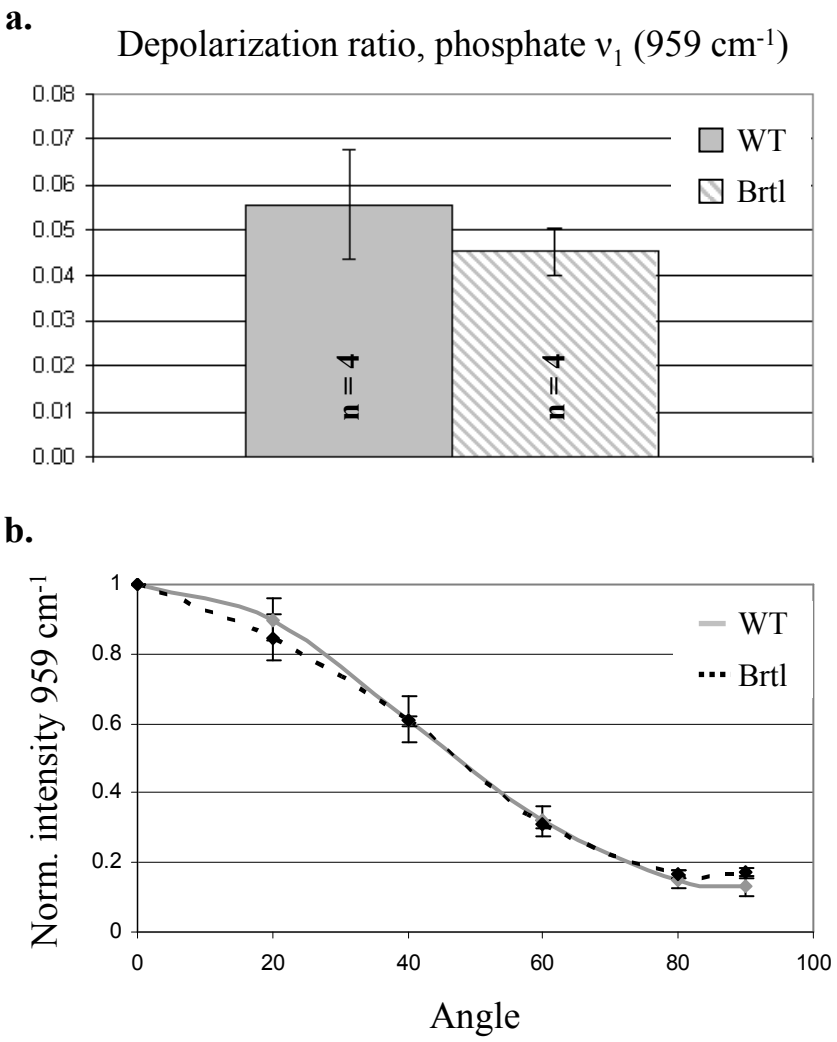

Figure 4.3. Average phosphate ν_1 depolarization ratio for all specimens. (a) The average depolarization ratio obtained for the 4 WT and 4 Brtl specimens examined. Mean ± standard deviation values are shown. $R_{959,WT} = 0.056 \pm 0.012$ and $R_{959,\ Brtl} = 0.045 \pm 0.005$. (b) Normalized peak intensity at 959 cm^{-1} was measured as a function of angle between the polarization direction of the excitation and collected light. Each data point is the average intensity from 4 WT or 4 Brtl specimens.

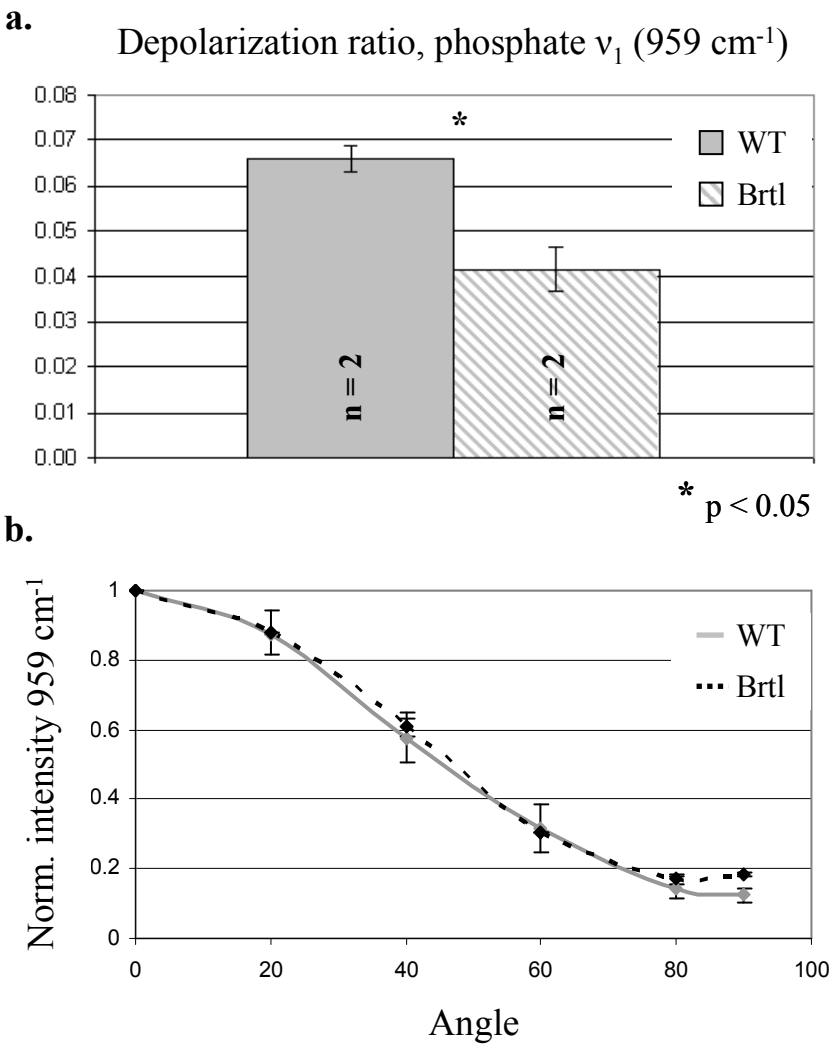

Figure 4.4. Average phosphate ν_1 depolarization ratio for 13-week-old specimens. (a) A significant difference was found between the average depolarization ratio obtained for the 2 WT and 2 Brtl specimens at 13 weeks of age. Mean ± standard deviation values are shown. $R_{959,WT}$ = 0.066 ± 0.003 and $R_{959,Brtl}$ = 0.042 ± 0.005. (b) Normalized peak intensity at 959 cm^{-1} was measured as a function of angle between the polarization direction of the excitation and collected light. Each data point is the average intensity from 2 WT or 2 Brtl specimens.

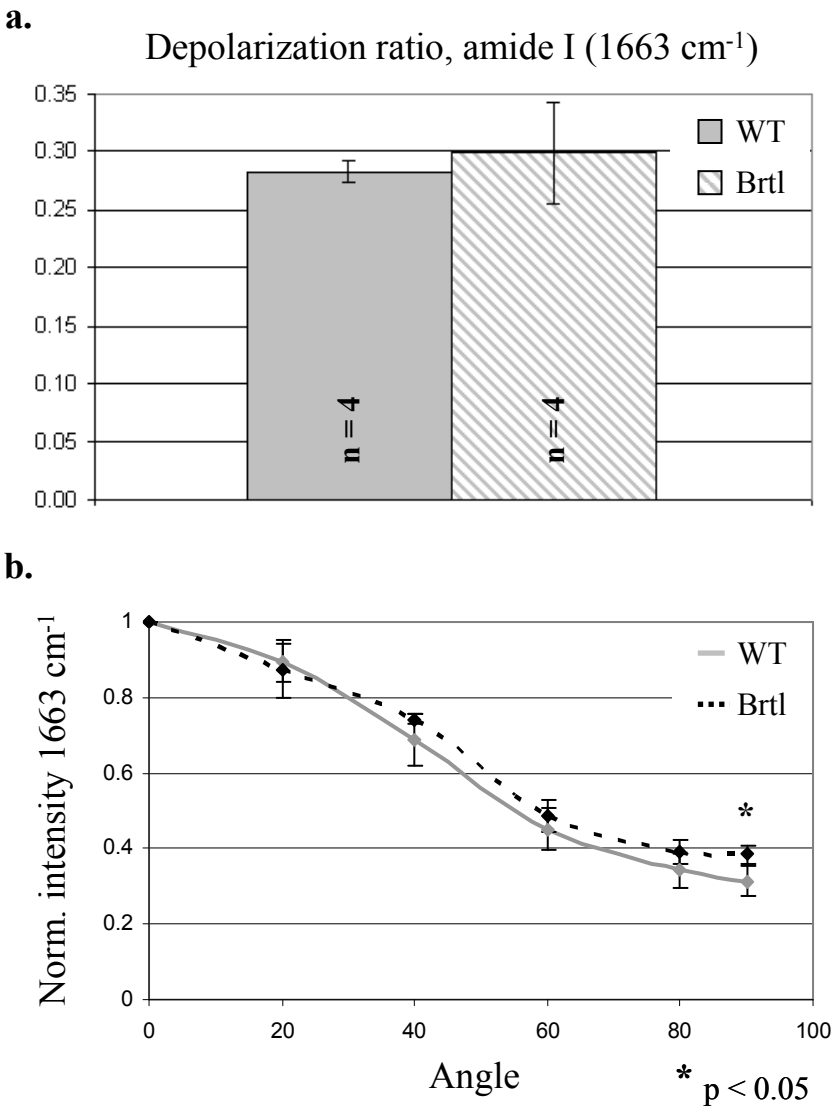

Figure 4.5. Average amide I depolarization ratio for all specimens. (a) The average depolarization ratio obtained for the 4 WT and 4 Brtl specimens examined. Mean ± standard deviation values are shown. $R_{1663,WT} = 0.28 \pm 0.01$ and $R_{1663,Brtl} = 0.30 \pm 0.04$. (b) Normalized peak intensity at 1663 cm^{-1} was measured as a function of angle between the polarization direction of the excitation and collected light. Each data point is the average intensity from 4 WT or 4 Brtl specimens.

	ID	Age (weeks)	R_{959} (Mean ± SD)	R_{1663} (Mean ± SD)
WT	1	13	0.064 ± 0.023	0.27 ± 0.04
	2	13	0.068 ± 0.018	0.28 ± 0.04
Brtl	3	13	0.045 ± 0.010	0.27 ± 0.03
	4	13	0.038 ± 0.006	0.28 ± 0.02
WT	5	17	0.044 ± 0.008	0.28 ± 0.06
	6	17	0.046 ± 0.011	0.30 ± 0.06
Brtl	7	15	0.046 ± 0.004	0.36 ± 0.09
	8	15	0.051 ± 0.017	0.28 ± 0.07

Table 4.1. Average depolarization ratios for WT and Brtl specimens. The average depolarization ratio for phosphate ν_1 (959 cm^{-1}) and amide I (1663 cm^{-1}) are shown. The ratios are the averages from five locations on each specimen.

References

1. M. Tanaka and R. Young, "Polarised Raman spectroscopy for the study of molecular orientation distributions in polymers," *J. Mater. Sci.* **41**(3), 963-991 (2006).

2. N. J. Everall, "Measurement of orientation and crystallinity in uniaxially drawn poly(ethylene terephthalate) using polarized confocal Raman microscopy," *Appl. Spectrosc.* **52**(12), 1498-1504 (1998).

3. M.-E. Rousseau, T. Lefevre, L. Beaulieu, T. Asakura, and M. Pezolet, "Study of protein conformation and orientation in silkworm and spider silk fibers using Raman microspectroscopy," *Biomacromolecules* **5**(6), 2247-2257 (2004).

4. M. Tsuboi, J. M. Benevides, P. Bondre, and G. J. Thomas, "Structural details of the thermophilic filamentous bacteriophage PH75 determined by polarized Raman microspectroscopy," *Biochemistry* **44**(12), 4861-4869 (2005).

5. H. Tsuda and J. Arends, "Orientational micro-Raman spectroscopy on hydroxyapatite single crystals and human enamel crystallites," *J. Dent. Res.* **73**(11), 1703-1710 (1994).

6. G. Leroy, G. Penel, N. Leroy, and E. Bres, "Human tooth enamel: A Raman polarized approach," *Appl. Spectrosc.* **56**(8), 1030-1034 (2002).

7. M. Kazanci, P. Roschger, E. P. Paschalis, K. Klaushofer, and P. Fratzl, "Bone osteonal tissues by Raman spectral mapping: Orientation-composition," *J. Struct. Biol.* **156**(3), 489-496 (2006).

8. M. Kazanci, H. D. Wagner, N. I. Manjubala, H. S. Gupta, E. Paschalis, P. Roschger, and P. Fratzl, "Raman imaging of two orthogonal planes within cortical bone," *Bone* **41**(3), 456-461 (2007).

9. G. Falgayrac, S. Facq, G. Leroy, B. Cortet, and G. Penel, "New method for Raman investigation of the orientation of collagen fibrils and crystallites in the Haversian system of bone," *Appl. Spectrosc.* **64**(7), 775-780 (2010).

10. M. Portigliatti Barbos, P. Bianco, A. Ascenzi, and A. Boyde, "Collagen orientation in compact bone: II. Distribution of lamellae in the whole of the human femoral shaft with reference to its mechanical properties," *Metab. Bone Dis. & Rel. Res.* **5**(6), 309-315 (1984).

11. S. I. Hong, S. K. Hong, J. M. Wallace, and D. H. Kohn, "Ultrastructural observation of electron irradiation damage of lamellar bone," *J. Mater. Sci.: Mater. Med.* **20**(4), 959-965 (2009).

12. S. Gamsjaeger, A. Masic, P. Roschger, M. Kazanci, J. W. C. Dunlop, K. Klaushofer, E. P. Paschalis, and P. Fratzl, "Cortical bone composition and orientation as a function of animal and tissue age in mice by Raman spectroscopy," *Bone* **47**(2), 392-399 (2010).

13. J. Moradian-Oldak, S. Weiner, L. Addadi, W. J. Landis, and W. Traub, "Electron imaging and diffraction study of individual crystals of bone, mineralized tendon and synthetic carbonate apatite," *Connect. Tissue Res.* **25**(3-4), 219-228 (1991).

14. W. J. Landis, M. J. Song, A. Leith, L. McEwen, and B. F. McEwen, "Mineral and organic matrix interaction in normally calcifying tendon visualized in three dimensions by high-voltage electron microscopic tomography and graphic image reconstruction," *J. Struct. Biol.* **110**(1), 39-54 (1993).

15. W. J. Landis, "Tomographic imaging of collagen-mineral interaction: Implications for osteogenesis imperfecta," *Connect. Tissue Res.* **31**(4), 287-290 (1995).

16. S. Weiner and W. Traub, "Organization of hydroxyapatite crystals within collagen fibrils," *FEBS Letters* **206**(2), 262-266 (1986).

17. D. P. Strommen, "Specific values of the depolarization ratio in Raman spectroscopy," *J. Chem. Educ.* **69**(10), 803-807 (1992).

18. A. C.-T. Ko, L.-P. i. Choo-Smith, M. Hewko, M. G. Sowa, C. C. S. Dong, and B. Cleghorn, "Detection of early dental caries using polarized Raman spectroscopy," *Opt. Express* **14**(1), 203-215 (2006).

19. P. H. Byers and W. G. Cole, "Osteogenesis imperfecta," in *Connective Tissue and Its Heritable Disorders*, P. M. Royce and B. Steinmann, Eds., pp. 385-430, Wiley-Liss, Inc. (2002).

20. A. Forlino, F. D. Porter, E. J. Lee, H. Westphal, and J. C. Marini, "Use of the Cre/lox recombination system to develop a non-lethal knock-in murine model for osteogenesis imperfecta with an α1(I) G349C substitution," *J. Biol. Chem.* **274**(53), 37923-37931 (1999).

21. A. Forlino and J. C. Marini, "Osteogenesis imperfecta: Prospects for molecular therapeutics," *Mol. Genet. Metab.* **71**(1-2), 225-232 (2000).

22. M. Raghavan, N. D. Sahar, R. H. Wilson, M.-A. Mycek, N. Pleshko, D. H. Kohn, and M. D. Morris, "Quantitative polarized Raman spectroscopy in highly turbid bone tissue," *J. Biomed. Opt.* **15**(3), 037001 (2010).

23. C. D. Allemand, "Depolarization ratio measurements in Raman spectrometry," *Appl. Spectrosc.* **24**(3), 348-353 (1970).

24. F. W. L. Esmonde-White, M. V. Schulmerich, K. A. Esmonde-White, and M. D. Morris, "Automated Raman spectral preprocessing of bone and other musculoskeletal tissues," *Proc. SPIE* **7166**(1), 716605 (2009).

25. M. J. Pelletier, "Effects of temperature on cyclohexane Raman bands," *Appl. Spectrosc.* **53**(9), 1087-1096 (1999).

26. P. Fratzl, O. Paris, K. Klaushofer, and W. J. Landis, "Bone mineralization in an osteogenesis imperfecta mouse model studied by small-angle X-ray scattering," *J. Clin. Invest.* **97**(2), 396-402 (1996).

27. A. Gautieri, S. Uzel, S. Vesentini, A. Redaelli, and M. J. Buehler, "Molecular and mesoscale mechanisms of osteogenesis imperfecta disease in collagen fibrils," *Biophys. J.* **97**(3), 857-865 (2009).

28. D. J. McBride, V. Choe, J. R. Shapiro, and B. Brodsky, "Altered collagen structure in mouse tail tendon lacking the α2(I) chain," *J. Mol. Biol.* **270**(2), 275-284 (1997).

29. C. A. Miles, T. J. Sims, N. P. Camacho, and A. J. Bailey, "The role of the α2 chain in the stabilization of the collagen type I heterotrimer: A study of the type I homotrimer in oim mouse tissues," *J. Mol. Biol.* **321**(5), 797-805 (2002).

CHAPTER V

FIBER-OPTIC RAMAN SPECTROSCOPIC PROBES AND SOFTWARE

1 Chapter overview

Research using fiber-based Raman systems, in which light is directed to and from the specimen with fiber-optic cables rather than through a microscope, is addressed in this chapter. Improvements to ex vivo, through-the-skin bone measurements on animal tissue are presented. Also, an experimental study detailing the improvements to fiber spectra obtained by applying software corrections to coupling errors that arise when collecting with fiber bundles is discussed.

2 Improvements in transcutaneous bone Raman spectroscopy

2.1 Introduction

Depth-resolved measurements of chemical content in turbid systems, such as living tissue, are an important goal in biomedical research. The ability to noninvasively probe tissue is important because biochemical changes often accompany disease states. Raman spectroscopy is well-suited to this goal because of its relative insensitivity to water and its high chemical specificity. For example, it has been used to detect calcified

materials placed under chicken breast tissue.[1, 2] Other applications of depth-resolved measurements in tissue include monitoring the state of bone health[3] and monitoring glucose concentrations in vivo.[4] Depth-resolved Raman measurements are not simply limited to applications in tissue. They can be implemented in any case where information about chemical content of subsurface layers is desired, such as in quality control monitoring of pharmaceutical tablets and capsules[5, 6] or security screening through bottles or other opaque containers.[7, 8]

When taking transcutaneous measurements, several challenges exist that hinder efficient collection of bone Raman spectra and limit the depths at which accurate spectra can be obtained. These include intense light scattering in tissue, fluorescence from skin components, and thermal damage due to absorption of laser light. Intense light scattering occurs because the illumination wavelengths used for transcutaneous measurements (785 or 830 nm) are in the diagnostic window, and the predominant process is scattering rather than absorption. Scattering is a random process, analogous to diffusion, and light propagation under scattering conditions is called photon diffusion or photon migration in the biomedical optics literature.[9, 10] It arises from the multiple differences in refractive indices of cellular structures.[11] It is important to note that diffusive scattering is different than Raman scattering. Diffusive scattering is elastic and does not involve a change in photon energy, whereas Raman scattering is inelastic and arises from an energy exchange between the incident light and the scattering molecules. Photon migration not only limits the amount of excitation light that is incident on bone, but also limits the amount of Raman-scattered light that is collected. Other difficulties in transcutaneous measurements include fluorescence from tissue components, particularly melanin in skin

and hemoglobin in blood.[12, 13] The fluorescent components contribute background to the Raman spectra that may overwhelm the Raman signal. Also, if the laser power is too high, absorption may cause thermal damage to the skin.[14]

Currently, the simplest and most effective way to alleviate these problems is by spatially separating the illumination and collection regions, as is commonly done in tissue fluorescence and NIR absorbance spectroscopies.[11, 15] In Raman spectroscopy, the technique of using a spatial separation between illumination and collection is known as spatially offset Raman spectrosocopy (SORS).[16] Due to the diffusive nature of photons in tissue, an offset configuration allows collection of Raman spectra that contain greater contributions from subsurface components (see Figure 5.1). As the distance between illumination and collection regions is increased, signals arising from near the surface become less prominent, and more of the collected Raman scattered light originates from deeper within the tissue. One of the first probe configurations used point illumination and point collection,[16, 17] but SORS probes can employ many different illumination/collection geometries. Another probe design independently developed in our lab[18, 19] and by Matousek[7] includes a circular collection fiber bundle surrounded by an illumination ring. In this ring/disk probe, the spacing between the illumination ring and collection disk can be varied to emphasize contributions from Raman spectra at different depths. This configuration is also beneficial because surface fluorescence from skin melanin can be spatially rejected and thermal damage can be minimized and usually eliminated entirely by the distribution of laser power over the illumination ring.

This section outlines improvements made to Raman transcutaneous measurements of bone using canine and murine tissue. Using the ring/disk probe, accurate recovery of

band ratios through thick overlying tissue layers will be discussed. The introduction of another probe geometry to reduce fluorescence and noise for use in measurements of murine tissue will also be presented.

2.2 Materials and methods

2.2.1 *Specimen preparation*

Intact lower limbs from canine (n=1) and murine specimens (n=3) were used. All animals were sacrificed in the course of unrelated studies at the University of Michigan Medical School. For the canine measurements, the left limb was used and all soft tissues and skin distal to the femur were preserved. For the murine specimens, the mice were intact and their limbs not dissected. For both types of tissue specimens, hair was removed from each leg with a depilatory agent (Sally Hansen Corporation, Uniondale, NY) prior to transcutaneous measurements. Glycerol (Sigma-Aldrich Corporation, Milwaukee, WI) was then applied to the skin as an optical clearing agent to increase the laser light penetration depth into the tissue.[20, 21] Transparent, 12.5-µm thick polyethylene film (Handi-Wrap, DowBrands, Indianapolis, IN) was placed over the surface of the limb, and water was dripped onto the film during collection in order to prevent thermal damage.

2.2.2 *Raman instrumentation and spectroscopic measurement*

A schematic of the Raman spectroscopy experimental apparatus is shown in Figure 5.2. A 400-mW 785-nm diode laser (Invictus, Kaiser Optical Systems, Inc., Ann Arbor, MI) was used for excitation. The laser light was launched into a 200-µm core NIR optical fiber (Multimode Fiber Optics, Hackettstown, NJ) and then collimated with a fiber-optic collimator (F810FC-780, Thorlabs, Inc., Newton, NJ). For the canine

specimen, the beam was directed through an axicon (cone angle 175°, Del Mar Photonics, San Diego, CA) which converts the Gaussian laser beam into a ring of light. A positive/negative lens pair was used to adjust the inner diameter of the illumination ring to between 2.5 and 11 mm at the specimen. For the murine specimens, the collimated laser beam was directed through a 60-mm focal length cylinder lens, which focuses the laser beam into a line. A positive/negative lens pair focused the line to dimensions of approximately 0.75 mm x 3.65 mm at the specimen. All beam-shaping and focusing optics were mounted in lens tubes (SM1 series, Thorlabs, Inc.).

A dichroic mirror (Chroma Technology Corporation, Rockingham, VT) then reflected the excitation light onto the specimen and also transmitted the Raman signal to the collection fibers. Two collection fiber bundles were used: fifty 100-μm-core fibers arranged in a circular bundle at the sample (PhAT probe, Kaiser Optical Systems, Inc.) and fifty 100-μm-core fibers arranged in a 5 x 10 rectangular array at the sample (FiberTech Optica Inc., Kitchener, Ontario, Canada). For the opposite end of each bundle, the fibers were arranged into a line and positioned at the input focal plane of the spectrograph.

For canine transcutaneous measurements, the circular bundle was used for collection. It was positioned at the medial side of the mid-diaphysis of the tibia. The collection disk was focused to a 3-mm-diameter field of view using a 75-mm focal length lens placed at the distal end of the collection bundle. Each of the ten illumination rings (inner diameter range 2.5-11 mm) was centered around the field of view of the collection bundle. The acquisition time for measurement at each ring diameter was 200 seconds. The power at the specimen was approximately 230 mW. After all transcutaneous

measurements were completed, the overlying tissue was removed and measurements on exposed bone were obtained with an integration time of 120 seconds. For exposed bone measurements, laser light was projected through the built-in optics of the PhAT probe (circular collection bundle) and the 75-mm focal length lens.

For murine transcutaneous measurements, both the circular and rectangular fiber bundle were used for collection. Three line illumination/collection geometries were used, as shown in Figure 5.2. For all three configurations, the collection bundle was centered over the mid-diaphysis of the tibia, and the long axis of the rectangular bundle was parallel to the long axis of the tibia. The collection disk was focused to a 3-mm-in-diameter spot and the collection rectangle was focused to an approximately 1.5 mm x 3 mm rectangle using a 75-mm focal length lens placed at the head of the collection bundle. For each illumination/collection geometry, data were acquired in a series of 10 measurements at 30 seconds each. The power at the specimen was approximately 165 mW. After transcutaneous measurements were completed, exposed bone measurements were acquired for 60 seconds using global illumination and collection via the PhAT probe circular fiber bundle.

Both collection bundles delivered light to a NIR-optimized imaging spectrograph (HoloSpec f/1.8, Kaiser Optical Systems) equipped with a 50-μm slit that provided 6-8 cm^{-1} spectral resolution. The detector was a thermoelectrically-cooled, back-illuminated, deep-depletion CCD camera (DU420-BR-DD, Andor Technology, South Windsor, CT) operating at -75 °C.

2.2.3 *Data analysis*

For the canine measurements, all data reduction was performed in MATLAB (The Mathworks, Inc., Natick, MA) using vendor-supplied and locally written scripts. Pre-processing included CCD wavenumber calibration against a neon discharge lamp and a Teflon Raman spectrum, removal of noise spikes, subtraction of dark current, correction for the wavelength response of the CCD, and correction for the curvature of spectral bands caused by the large gathering angle of the spectrograph,

The data for each acquisition consisted of an array of 256 Raman spectra, the number of pixel rows along the spatial dimension of the CCD. The 256 spectra were collected by 50 fibers. In order to approximate the spectrum collected by one fiber and avoid cross-talk, the three central pixel rows for each fiber were averaged. This yielded a data set of 50 spectra in which each spectrum corresponded to one fiber. After the 50 individual fiber spectra were recovered, an iterative baselining procedure was used to remove the background fluorescence.[22] Baselined spectra were then normalized to the phosphate band.

Band target entropy minimization (BTEM),[23, 24] an algorithm based on factor analysis, was used to recover the portion of the collected Raman signals that originated solely from bone tissue, called the recovered bone factor. In spectroscopy, factor analysis extracts spectral characteristics that are correlated with each other. It is useful for separating pure components that have overlapping spectra but different spatial distributions within the analysis volume or area. Hence, it is useful for tissue Raman spectroscopy because a transcutaneous spectrum can be viewed as a mixed component spectrum that consists of linear superpositions of pure component spectra (i.e. skin, muscle, tendon, fat, bone, etc), each with a different distribution.

The covariance matrix of the mixed component spectrum was calculated, and then singular value decomposition was used to calculate the eigenvectors of the covariance matrix. The eigenvectors represent the amount of variance in the data set, where the first eigenvector represents the most variance and the last eigenvector represents the least variance and describes mainly noise. To recover a pure bone spectrum, a 4 cm^{-1} interval around the phosphate ν_1 band (~959 cm^{-1}) was chosen for band targeting because the band is intense and absent from surrounding tissues. The number of eigenvectors used in extracting the pure component bone spectrum was determined by using a weighting test.[25] Eigenvectors were added until their weightings were near zero and the resulting spectrum did not change upon addition of more eigenvectors. Eigenvectors containing mainly noise were used to improve the signal-to-noise ratio in the recovered bone factors.

The recovered bone factor and the mean exposed bone measurement were imported into GRAMS/AI (Thermo Galactic, Madison, WI) and fit for peak heights and areas using mixed Gaussian and Lorentzian polynomials. To compare the recovered bone factor with exposed bone, the carbonate-to-phosphate (1070 cm^{-1}/959 cm^{-1}) height and area ratios were calculated.

For the murine measurements, the transcutaneous spectra from all three mice (six tibiae) taken with a single illumination/collection geometry were averaged together in order to examine the overall fluorescence among the three illumination/collection geometries used. The amount of noise in the transcutaneous measurements was quantified using the mean spectra which had not been corrected for background or separated into bone and overlying tissue components. The power spectrum was calculated for each mean spectrum. For those calculations, the dispersion axis was left in

pixels (rather than converting to wavenumbers) so the noise contribution from each pixel would be weighted equally.

2.3 Results

From the 10 ring/disk separations measured on the canine limb, the optimal separation distance was determined by plotting the phosphate ν_1-to-phenylalanine ring breathing (~1001 cm^{-1}) band height ratios as functions of illumination ring diameter (Figure 5.3a). This ratio measures the relative amounts of bone mineral to total collagen (skin, tendon, and bone) in the recovered spectra. The best fit line through the data points is approximated by the curve above the data points. The optimal separation between illumination and collection occurs during the rise of the curve, which corresponds to rings 5-7. The data from rings 5-7 was then combined into one file that was used to recover the pure bone spectrum by BTEM. Figure 5.3b shows the mean transcutaneous spectrum from rings 5-7, the recovered bone spectrum, and the reference spectra of exposed bone (n=50). In Figure 5.3c, the calculated carbonate-to-phosphate band height and area ratios from the recovered bone spectrum are compared to those from the exposed bone tissue. The height measurements are in good agreement (3% error) with the results for exposed tissue, but the agreement is worse (41% error) for measurements by area.

For the murine specimens, the mean spectrum for each probe geometry is plotted in Figure 5.4b. Fluorescence, as seen by the higher intensity background, was greatest in the line/box geometry where the illumination line was parallel to the rectangular bundle (line/box-1). Next was the line/disk geometry, and the least amount of fluorescence was collected by the line/box geometry where the illumination line was perpendicular to the rectangular bundle (line/box-2). Figure 5.4c shows the power spectrum, which is a

measure of how much noise is present in the spectrum. The higher frequency components correspond to higher noise. The most noise was collected with the line/box-1 probe, followed by the line/disk and then line/box-2 probe.

2.4 Discussion

For the ring/disk measurements on canine tissue, different spatial separations between the illumination ring and the collection fiber bundle were used to investigate the recovery of subsurface Raman spectra. The optimal separation was determined by plotting the phosphate-to-phenylalanine ratio vs. ring center diameter. At small separations, the ratio is low and Raman scatter from near the skin surface is overemphasized. With increasing ring/disk spacing, the ratio increases. The increase is slow at small spacings and rapid when the spacing is increased sufficiently to attenuate much of the signal from skin and tendon collagen. The ring center diameters coincident with the rapid rise in the phosphate-to-phenylalanine ratio define the illumination/collection separations at which the best accuracy is obtained. Although the bone contributions to the measured spectra are even greater with larger spacings, the signal-to-noise ratio decreases rapidly, leading to increased error. In this experiment, illumination rings 5-7 had the most nearly optimal separation distances from the circular collection fiber bundle. The optimal separation depends on the depth of the bone below the surface. In this experiment, the depth of the tissue overlying the canine tibia was 6 mm and was measured only after transcutaneous measurements were completed.

The accuracy of the recovered bone spectrum measured transcutaneously was determined by calculating the carbonate-to-phosphate ratio and comparing it to the exposed bone measurements. Using band heights, the carbonate-to-phosphate ratio

between the recovered bone and the exposed bone differed by 4%. The area ratio was in error by over 40%, probably because band areas are more susceptible to errors from imperfect baselining than are band heights. The accurate recovery of Raman bone spectra through 6 mm of canine tissue is 20% improved depth penetration compared to published results.[19] The ability to accurately recover the carbonate-to-phosphate ratio could be clinically important. For example, our laboratory has shown that in iliac crest specimens matched for age and bone volume fraction the Raman-measured carbonate-to-phosphate ratio was significantly higher (~20%) in women who suffered an osteoporotic fracture than in women who did not suffer a fracture.[26]

For the measurements on murine tissue, the amount of fluorescence and noise collected was influenced by the amount of separation between the excitation and collection regions. The distance between the field of view of the farthest collection fiber and the delivery region of the excitation light was different for the three probes. The dimension of the collection fiber bundles relative to the illumination line is shown in Figure 5.4a. The illumination line was 0.75 mm thick, and the size of the collection fiber bundles was 3 mm in diameter for the circular bundle and 1.5 mm x 3 mm for the rectangular bundle. The separation distance between the illumination line and the farthest collection fiber was 0.38 mm for line/box-1, 1.13 mm for line/disk, and 1.13 mm for line/box-2. Line/box-1, which had the smallest spatial separation, also collected the most fluorescence and noise. Of the three geometries tested, the ring/disk and line/box-2 probe had the greatest separation, but the line/box-2 probe collected the least amount of fluorescence and noise.

Line illumination, rather than ring illumination, is more compatible with the limb dimensions of the long bones of small animals like mice. An illumination ring cannot be focused tightly enough to fit on a mouse limb. The rectangular collection bundle is also more compatible with the smaller limb dimensions. The circular collection bundle is 3 mm in diameter and it also cannot be focused tightly enough to impinge entirely on the limb. The fibers at the edges of the circular bundle "fall off" the edge of the limb and are not in focus on its surface. This effectively decreases the greatest separation that can be achieved between the illumination and collection regions and explains why the fluorescence and noise were higher in the line/disk probe compared to line/box-2.

2.5 Conclusion

Accurate recovery of the carbonate-to-phosphate band height ratio was demonstrated through 6 mm of overlying tissue on a canine tibia, currently the deepest depth achievable using backscattered light and a standoff configuration. For the murine measurements, the line/box-2 probe was the best suited for transcutaneous measurements of the three configurations tested because the geometry of the probe most accurately matched the geometry of the site of interest. The line/box-1 probe may be more suitable for other regions if the thickness of the overlying tissue is less and a smaller separation is needed. The amount of separation needed between illumination and collection regions for accurate recovery depends on the depth of the bone or target below the surface. For larger specimens, many more possibilities may exist for probe geometries.

3 Mathematical correction for coupling errors in fiber optic spectroscopy

3.1 Introduction

In imaging spectroscopy fiber optic bundles can be used to couple light into imaging spectrographs. Fiber bundles are used for light collection in spectroscopies including UV/Vis, fluorescence, Raman, and IR for a wide variety of applications. Fluorescence imaging fiber bundles have been used to image cancer cells and tumors in vivo[27] and to detect the presence of vapors from nerve agents or from materials that could be used for explosives.[28] They have also been used to detect differences in pH[29] and to monitor cell migration.[30] Thermal imaging with fiber bundles has been performed in the infrared region of the spectrum.[31, 32] Surface-enhanced Raman spectroscopy using metal particles applied to the tip of a bundle has been used to produce chemical images.[33]

Conventional thought is that a bundle with high fiber density is desirable for imaging because it will improve spatial resolution. Also, a bundle with a greater number of fibers collects more light, permitting shorter acquisition times. However, a close spacing of fibers may lead to light coupling and spectral mixing among fibers, thereby decreasing the spatial resolution. As Chen et al. showed, both fiber density and fiber-to-fiber coupling affect the spatial resolution.[34] At long wavelengths (978 nm), coherent imaging bundles with a lower fiber density outperformed bundles with more closely packed fibers because light coupling between the fibers degraded the image resolution. The fiber coupling was greater at longer wavelengths because refractive index of the silica fibers decreases as wavelength increases. While fiber coupling can occur at all wavelengths, this work demonstrated that fiber coupling is especially important when

working with longer wavelengths, as used in noninvasive biomedical applications where longer wavelengths are used to better penetrate tissue and to minimize absorption of tissue components.[11]

In these imaging examples, coherent bundles were employed, however, imaging with incoherent bundles is also feasible if the bundle has been previously mapped and the correspondence between fibers at both ends of the bundle are known.[35, 36] If the mapping is completed manually, then it is practical only on smaller bundles of about 100 fibers or fewer. In theory, the process could be automated and allow use of a bundle with a much greater number of fibers. With incoherent bundles, the problem of fiber-to-fiber coupling is especially troublesome because signal mixing from non-adjacent regions of the sample may occur.

Two types of fiber coupling, overlap and cross-talk, are shown in Figure 5.5. Overlap occurs after the collected light exits the fibers and is focused onto the charge-coupled device (CCD). It is caused by diffraction and uncorrected aberrations such as field curvature. The second type of coupling, cross-talk, occurs within the fibers when light from neighboring fibers crosses the cladding barrier that separates the light-guiding cores. In the fibers of Figure 5.5, the outer buffer has been stripped from the ends of the fibers, allowing cross-talk to occur. Removing the buffer from the ends of the optical fiber bundle is a common practice because it allows closer fiber packing, and therefore more fibers to be imaged onto the CCD.

Most methods for minimizing fiber coupling involve physical changes to the fiber bundle. These include increasing the spacing between adjacent fibers[37], increasing the refractive index difference between core and cladding[34], and adding a “dark” glass

around the fibers to absorb stray photons.[38] Increasing fiber-to-fiber spacing could completely eliminate coupling, but it reduces fiber count so the spatial resolution and achievable definition are inherently lower. Barriers or special coatings may also be used to minimize coupling but may increase the cost of the bundles substantially.

Instead of making hardware changes to correct for fiber coupling, we propose the use of software correction to recover individual fiber spectra during data preprocessing. The aim of this study is to compare two different spectral preprocessing methods for their ability to correct for fiber signal mixing. Mathematical correction for fiber coupling enables the use of a tightly-packed fiber bundle, thus bypassing the fiber spacing/signal mixing trade-off.

3.2 Materials and methods

3.2.1 *Experimental configuration*

The collection fiber bundle used in this experiment consisted of 50 fibers with 100-μm core/110-μm cladding. The 240-μm buffer was removed from all fibers at both ends of the bundle in order to more efficiently use the detector height. The fibers were arranged into a 5x10 rectangular array at the sample, and arranged into a 1x50 line at the spectrograph. The incoherent bundle was mapped and fiber assignment determined.

The light collected by the fiber bundle was delivered to the RAMAN RXN1 system (Kaiser Optical Systems, Inc., Ann Arbor, MI), which consists of an axial transmissive imaging spectrograph (HoloSpec f/1.8) configured with a 50-μm slit to provide spectral resolution of 6-8 cm^{-1} and a thermoelectrically cooled 1024x255 pixel CCD camera (Model DV420A-OE-133, Andor Technology, South Windsor, CT)

operated at - 40°C. The RXN1 system also includes a 400-mW 830-nm diode laser (Invictus, Kaiser Optical Systems, Inc.) equipped with a fiber launcher.

For data measurements, the 5x10 fiber array was focused onto the intersection of two polymers, Teflon and Delrin. Blocks of these two polymers were separated by a piece of aluminum foil (see Figure 5.7a). Since the aim of this study was to examine the effects of fiber signal mixing, the foil ensured that any spectral mixing that was seen was caused by signal mixing between fibers, rather than light coupling between the polymers. Twenty fibers were centered over each of Teflon and Delrin. The ten fibers that were partially centered over the aluminum foil were excluded from analysis. The laser was launched into a separate fiber-optic cable and focused with a 100-mm achromat (Thorlabs, Inc.) onto the intersection of the polymers. The entire region over which the fibers were in focus was illuminated. Because the polymers were obliquely illuminated, the power density varied slightly between them.

In order to do software correction and separate spectra collected with each fiber, the profiles of individual fibers in the detector's spatial dimension were measured. This was most easily accomplished by focusing the fiber bundle through a microscope and then illuminating one fiber at a time via a pinhole placed over a white-light source. A HoloLab Calibration Accessory (Kaiser Optical Systems, Inc., Ann Arbor, MI) was secured to the microscope translation stage. A custom-made adapter positioned a 25-μm pinhole over the diffused white light from the Calibration Accessory. The pinhole was brought into focus using a 4x/0.2 NA objective (Plan Apo, Nikon Instruments, Melville, NY). Next, the rectangular end of the bundle was focused through the microscope using a 60-mm achromat (Thorlabs, Inc., Newton, NJ) and the same 4x objective. White light

was injected into the linear end of the bundle to visualize the fibers and focus them at the same plane where the pinhole was in focus. All 50 fibers could be seen in the field of view of the objective. Using the translation stage, the pinhole, whose diameter was smaller than the diameter of a fiber, was centered in the middle of a fiber. At this point, the linear end of the bundle was presented to the spectrograph, and a white-light spectrum was collected for that fiber. This procedure was repeated for all 50 fibers. These measurements allowed assessment of both fiber overlap and fiber cross-talk.

3.2.2 *Data treatment*

All data reduction was performed in MATLAB (The Mathworks, Inc., Natick, MA) using vendor-supplied and locally written scripts. Preprocessing included removal of noise spikes, subtraction of dark current, image rotation and slit image curvature correction,[39] wavenumber calibration, and correction for the wavelength response of the CCD. The data for each acquisition consisted of an array of 255 Raman spectra, the number of pixel rows along the spatial dimension of the CCD (i.e. slit height). The 255 spectra were collected by the 5x10 rectangular fiber array, and in order to calculate a single spectrum for each fiber, two data processing methods were used. In the first, the three most intense or central pixel rows per fiber were averaged, resulting in 1 spectrum per fiber. Averaging the most intense pixels is a common way to process spectroscopic data. In this method, only about 60-70% of the collected light is used because data outside a fiber's three central pixel rows is simply thrown away. In contrast, the second procedure uses all the data in performing a least squares fitting of the known overlap and cross-talk spatial profiles for each fiber to the spectroscopic data. Each method reduces

the initial 255 spectra to 50 spectra, one per fiber. The two methods are subsequently referred to as the averaging or least squares method.

After the 50 individual fiber spectra were recovered, spectra were truncated and baselined using a polynomial fitting routine that finds the maximum value among multiple polynomial fits, rather than using a single polynomial fit across the entire spectrum.[40] We have found this method to be satisfactory in determining a good baseline across the entire spectrum, especially at the lowest and highest wavenumbers. Removal of fiber silica background was accomplished using derivative subtraction.[41]

3.3 Results

Typical fiber profiles are depicted in Figure 5.6. The two panels show the extent of overlap. For this experiment, the focus of the spectrograph was such that the fibers at the edges of the CCD were in better focus than the fibers in the center. For example, light from fiber 8 is distributed over ~9 pixel rows and overlaps with light from adjacent fibers. However, signal from fiber 25, centered at pixel 122 in the middle of the detector, is distributed over ~11 pixels. Because of this broader profile, signal from fiber 25 overlaps with signal from adjacent fibers and also its next nearest neighbors. A close examination of fiber profiles revealed the presence of cross-talk, although the intensity never exceeded 0.4% of the overall intensity. Cross-talk played a minor role in fiber coupling whereas overlap was the dominant contributor.

The averaging and least squares method are compared in Figures 5.7 to 5.10. Together with reference Teflon and Delrin spectra, the position of the rectangular bundle relative to the two polymers is shown in Figure 5.7a. These two polymers were chosen because each has at least one band that does not spectrally overlap with bands from the

other polymer. The most intense Teflon band is centered at 732 cm^{-1}, and the most intense Delrin band is centered at 918 cm^{-1}. Four of the most intense bands from each polymer are highlighted, with Teflon bands highlighted with dots and Delrin bands highlighted with slanted lines. In Figure 5.7b and 5.7c, the results from the averaging and least squares method are shown. Teflon-interrogating fibers are plotted on the left, with bands from the contaminating polymer (i.e. Delrin) highlighted. Delrin-interrogating fibers are plotted on the right and the contaminating Teflon bands are highlighted. For the Teflon-interrogating fibers, more of the Teflon signal is being recovered with the least squares method, as can be seen by the higher intensity of the 732 cm^{-1} Teflon band. This results in a slightly higher signal-to-noise ratio, but the bigger benefit is the reduction in intensity of contaminating Delrin bands. The heights of the highlighted Delrin bands in the least squares method are less than for the averaging method. The same pattern is seen in the Delrin-interrogating fibers, but the effect is less pronounced. The reason may be because the illumination was more intense on the Delrin side, as evidenced by the higher number of counts.

Upon closer inspection of the twenty Teflon-interrogating fibers, several fibers were identified in which by averaging, the contaminating Delrin bands were fairly intense even though the fibers were centered entirely over Telfon. This included Teflon fiber 27, whose spectrum showed the Delrin band at 918 cm^{-1} was actually more intense than the 732 cm^{-1} Teflon band. Figure 5.8 shows Teflon fiber 20, a fiber with intense Delrin contributions, for both the averaging and least squares method. The 732 cm^{-1} Teflon band is at ~1080 counts for the least squares method and only ~800 for the averaging method. Not only is the recovered Teflon signal more intense with least squares recovery,

but the contaminating Delrin band at 918 cm^{-1} is reduced in intensity from ~470 to ~190 counts. A representative fiber in which the contamination is less dramatic, fiber 35, is shown in Figure 5.9. Fiber 35 is centered over Teflon, with the main Teflon band intensity near 1120 counts and the main Delrin band near 60 counts for the averaging method. With the least squares method, the Teflon band is increased to ~1300 counts and the contaminating Delrin band is reduced to ~35.

In the previous examples, the least squares method outperformed the averaging method. However, in 4 of the 40 fibers analyzed, the averaging method did a better job of reducing the intensity of contaminating bands. These were fibers 19, 26, 28, and 37, two of which were centered over Teflon and two over Delrin. The spectrum for Delrin fiber 26, with contaminating Teflon bands highlighted, is shown in Figure 5.10. As expected, the major Delrin band increased in intensity with the least squares method. Unlike with most other fibers, however, is the contaminating Teflon band at 732 cm^{-1} also increased in intensity. The intensity was 20 counts for the averaging method but 99 counts with the least squares method.

3.4 Discussion

The degree of overlap among fibers is shown in Figure 5.6. The focus of the spectrograph can be adjusted to change the degree of fiber overlap. However, there is a compromise between good spatial resolution/number of fibers that can be in focus and spectral resolution. Perfect focus cannot be obtained over the entire width of the detector because residual field curvature is present. It is possible to get minimal overlap, but only for a limited number of fibers. If the entire detector height is illuminated (i.e. 50 fibers are used), some spatial resolution must be traded for spectral resolution. If focus or only

slight defocus is achieved for all 50 fibers, the minimum amount of overlap that exists for a fiber is with its two adjacent neighbors. Because our fiber bundle is incoherent, the coupling leads to spectral mixing among fibers that are not necessarily next to one another at the distal (or sample) end.

For the vast majority of the fibers, the least squares method does a better job of minimizing the effects of fiber overlap and cross-talk. It is more effective than the averaging method because the individual overlap and cross-talk profile for each fiber is measured, resulting in knowledge of how the signals will mix. All of the light that is collected is used when calculating the individual fiber spectra from the matrix of response profiles. As can be seen in Figure 5.7, the intensity of unwanted, contaminating bands are decreased in the spectra processed via the least squares method rather than the averaging method. Also, the intensity of the desired polymer bands is higher in the least squares spectra.

As seen in Figure 5.8 and 5.9, Teflon fiber 20 and 35 are specific cases where least squares reduces the intensity of the contaminating Delrin bands. Fiber 20 is a more dramatic case because the contaminating Delrin bands are quite intense. The spectral mixing seen in fiber 20 can be partially explained from the location of its adjacent neighbors. At the spectrograph end, adjacent fibers are not necessarily centered over the same polymer. Fiber 20 is centered over Teflon, but has an intense contribution from Delrin. Both fibers 19 and 21 (see 5x10 fiber map in Figure 5.8) are centered over Delrin and exhibit a strong Delrin signal. Hence, one of the reasons that fiber 20 has a strong Delrin contribution is because there is fiber coupling between its adjacent fibers at the

spectrograph end. Conversely, Teflon fiber 35 has a minor contribution from Delrin because its adjacent fibers, 34 and 36, are also centered over Teflon.

The extent of coupling for an individual fiber is not only affected by the type of spectra (i.e. Teflon or Delrin) collected by adjacent fibers, but also by other factors including the illumination intensity over the fiber and the focus of the CCD region where the fiber is located. The most serious cases of fiber coupling were observed with Teflon fibers. Fiber coupling was worse for Teflon fibers because the illumination intensity was uneven over the two polymers because oblique illumination was used. Teflon had lower illumination intensity than Delrin (as evidenced by the lower intensities). Also contributing to the discrepancy in intensity is the fact that Delrin is a higher-intensity Raman scatterer than Teflon, and so contamination by Delrin is more noticeable in the spectra than contamination by Teflon. In addition, fiber coupling was greatest for fibers focused in the middle of the CCD, where the focus was slightly worse than at the ends (see Figure 5.6). Therefore more overlap and more spectral mixing occurred in this region.

For four of the fibers (fibers 19, 26, 28, and 37), the averaging method slightly outperformed the least squares method. The exact reason is unclear. One possible contributor to this discrepancy is that the fiber core plus cladding (110 μm) is not an exact multiple of the CCD pixel height (26 μm). Because of this, in some cases the edge of a fiber will coincide with the middle of a pixel rather than the edge of a pixel. This limits the precision of the individual fiber profile measurements that are used in the least squares method. Another reason may be that the four fibers were focused in the middle

of the CCD, a region of slight defocus. The absolute intensities were lower in this region, and thus errors in the individual fiber profiles could lead to least squares fitting errors.

3.5 Conclusion

The effects of signal mixing can be quite pronounced with tightly-packed bundles. In this paper, the effects were dramatic because there was such a sharp boundary between two different polymers. In measurements of a more typical system, the coupling effects would be more subtle. Even still, the issue of fiber coupling should be considered. With incoherent fiber bundles, adjacent fibers centered over different regions of a heterogeneous sample are unavoidable. Uneven illumination and less-than-perfect spectrograph focus are not uncommon, and these problems that exacerbate signal mixing are likely to be encountered.

Signal mixing is mainly caused by fiber overlap, although cross-talk plays a minor role. If the fiber overlap and cross-talk profiles are measured for each fiber, then the fiber coupling that occurs can be corrected with least squares preprocessing. In almost every case, least squares reduces the effects of signal mixing more than conventional averaging. Because least squares minimizes signal mixing, it allows a closely-spaced fiber arrangement as the coupling is no longer required to be physically separated.

4 Chapter summary

For the transcutaneous measurements discussed in Section 2, both the illumination and collection fibers were in a standoff configuration, meaning the fibers

were focused onto the specimen using optical elements, rather than being placed directly on the specimen. There will always be a role for standoff measurements like the ones presented, particularly when validating in vivo transcutaneous measurements on humans (for example, during knee surgery), and direct contact with a patient's bone tissue would be prohibited. Thus, continual improvements to probe design, including different illumination/collection geometries, will be important. In addition to hardware improvements, software improvements that correct for the problem of overlap and cross-talk in closely-packed fiber bundles, like the least squares correction presented in Section 3, will also be beneficial in transcutaneous measurements.

These improvements, along with the exciting development of Raman tomography of bone (in which illumination and collection fibers are placed directly on the skin), will only lead to better, more accurate measurements of bone tissue through the skin. With these advancements, accurate transcutaneous measures of the bone matrix, rather than just the bone mineral, may be possible. Recovering accurate information about the bone matrix transcutaneously is a definite challenge as collagen is found not only in bone, but also in the overlying tissue.

It should also be noted that the least squares correction procedure is not limited to applications involving bone or Raman spectroscopy. Essentially any technique that uses closely-packed fiber bundles could potentially achieve more accurate results because of its implementation.

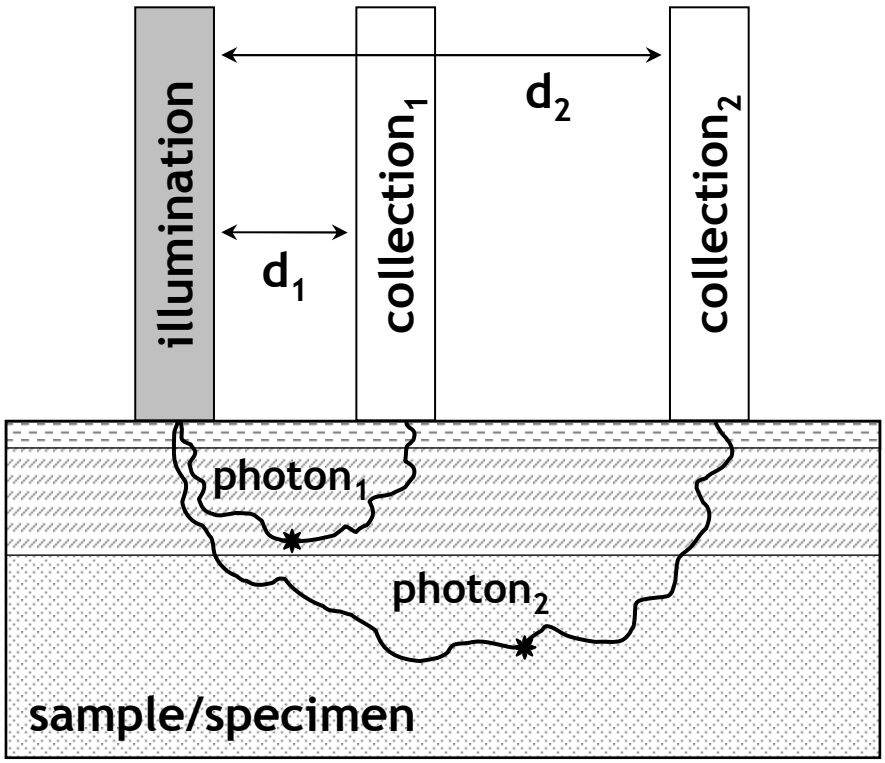

Figure 5.1. SORS model. Increasing the separation between the illumination and collection regions emphasizes Raman scatter that contains greater contributions from subsurface components. The stars represent the points where Raman scattered photons are generated.

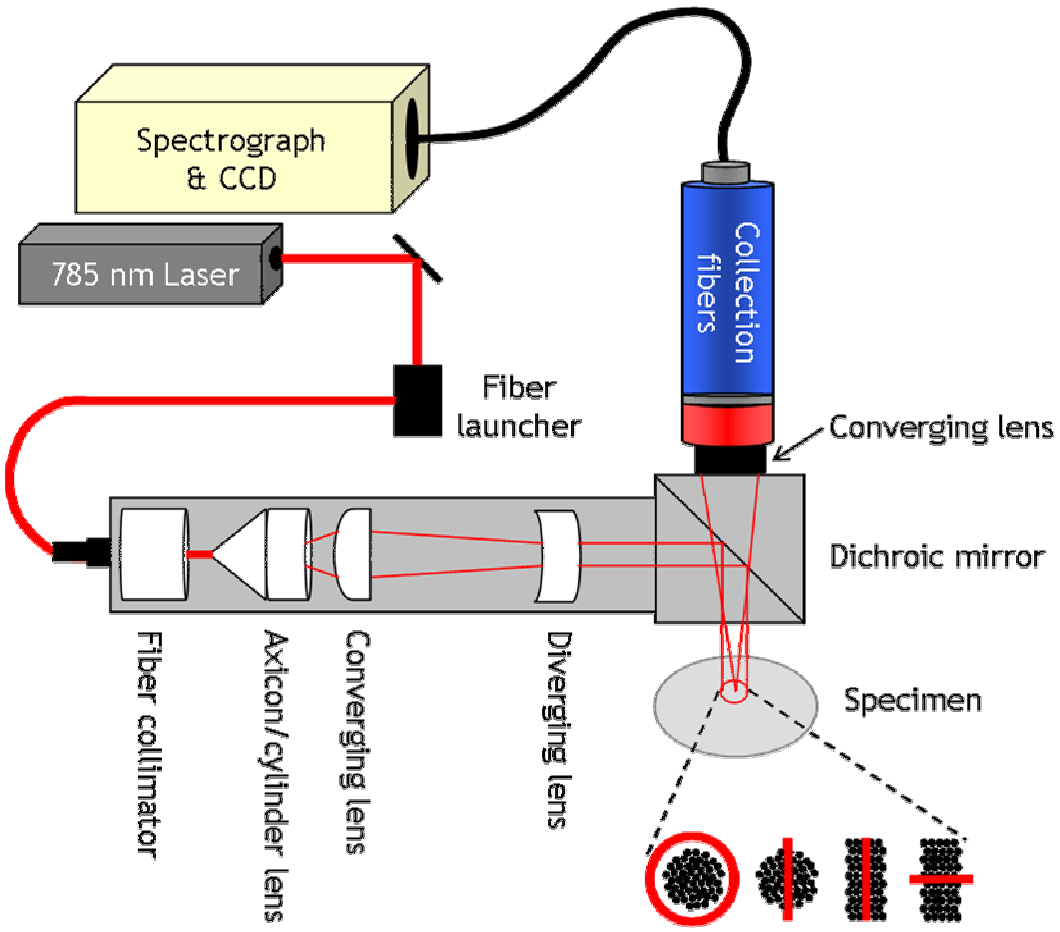

Figure 5.2. Experimental apparatus for SORS measurements. The probe generates an illumination ring or line by using an axicon or cylinder lens. The size of the illumination ring/line can be adjusted using lenses of different focal lengths. Light is collected with either a circular or rectangular bundle of 50 collection fibers in the geometries shown.

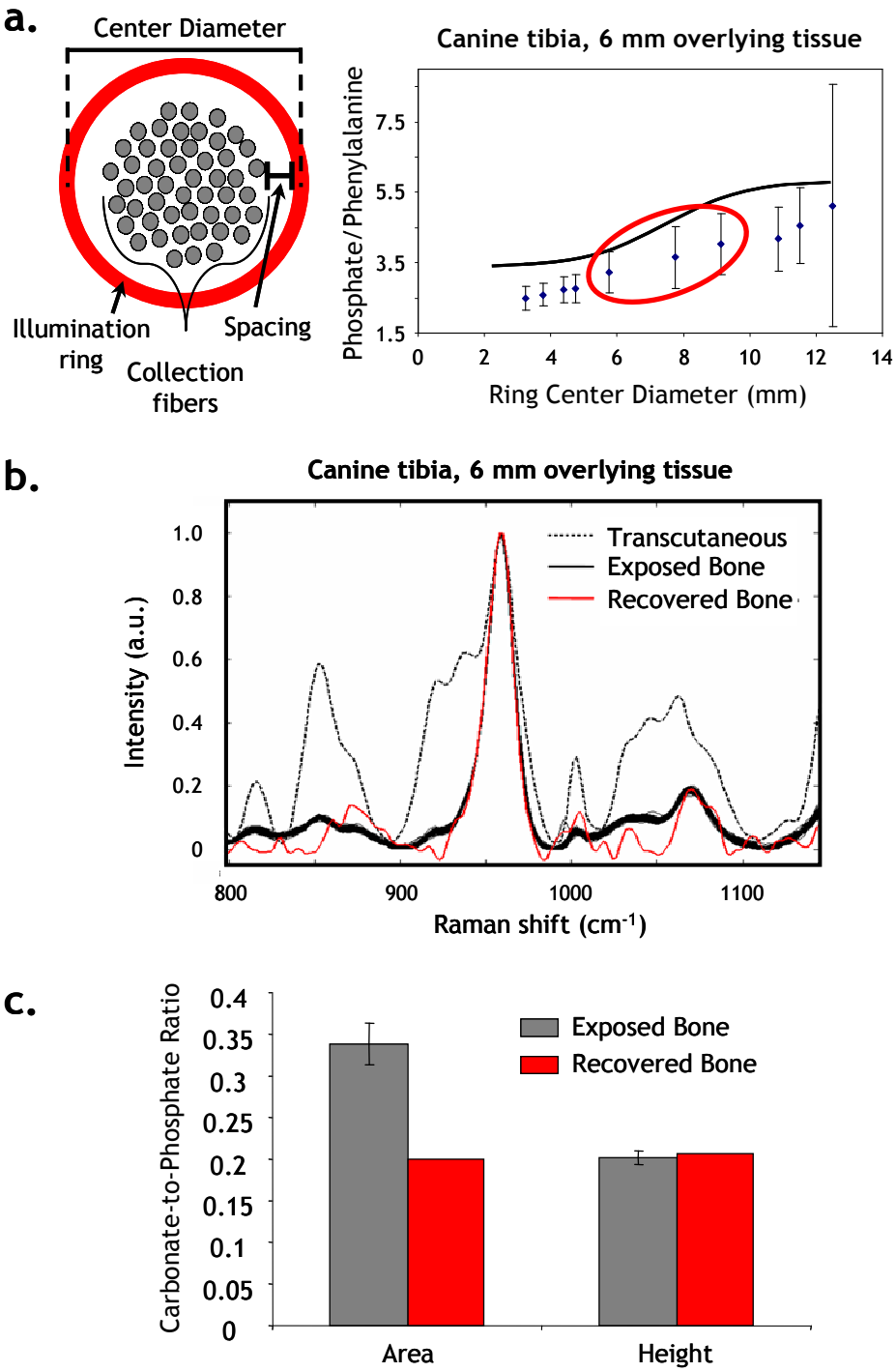

Figure 5.3. Transcutaneous Raman spectra of canine tibia. (a) The phosphate ν_1-to-phenylalanine band height ratio is plotted as a function of ring center diameter. (b) Transcutaneous Raman spectrum of canine tibia (dotted line), exposed bone spectra (n=50) (black), and recovered bone spectrum (red) are shown. (c) Accurate recovery of the carbonate-to-phosphate height ratio is achieved through 6 mm overlying tissue.

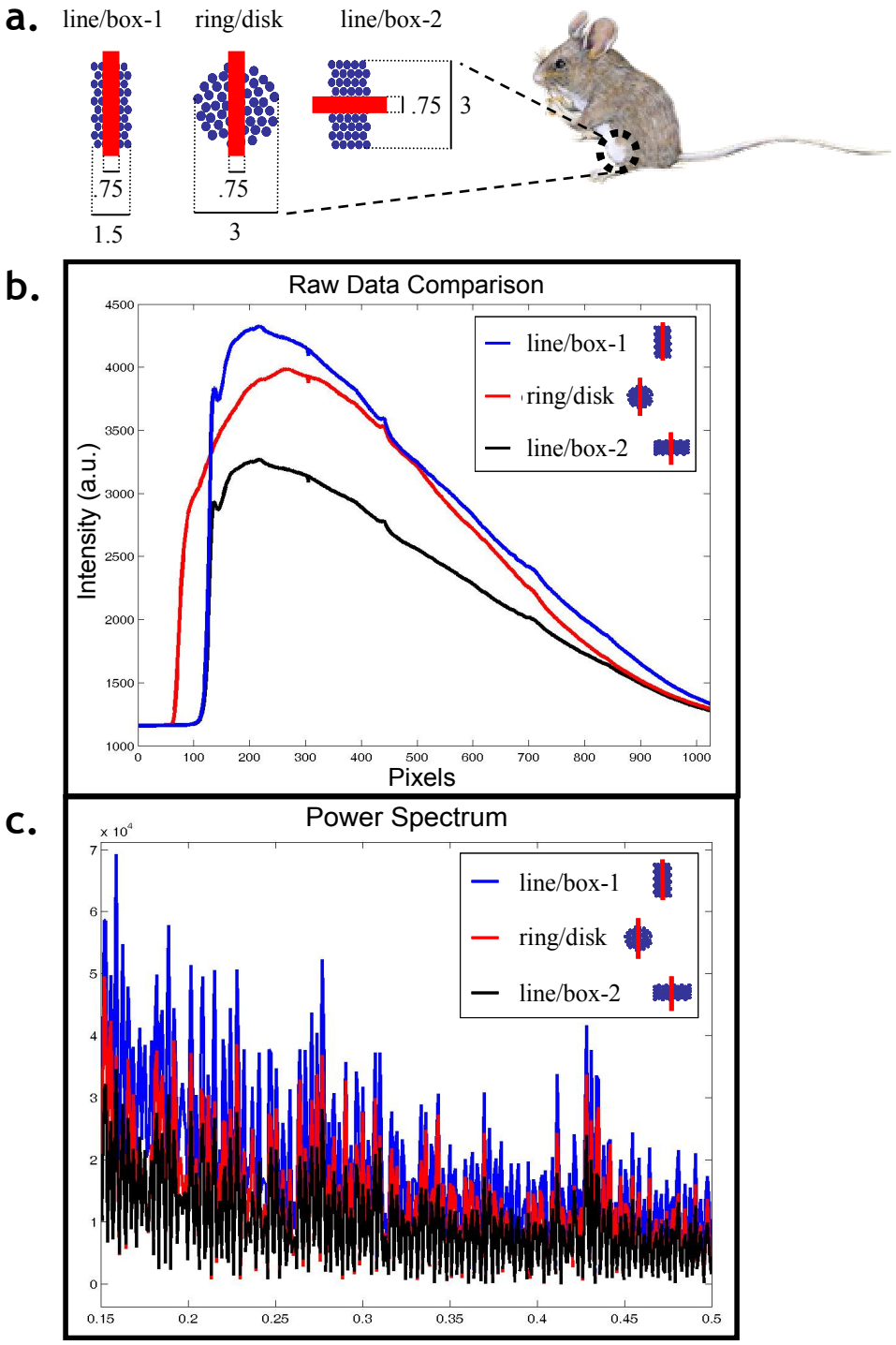

Figure 5.4. Comparison of three probe geometries for transcutaneous murine measurements. (a) Geometry of the three probe configurations is shown. (b) The mean spectrum for each probe geometry is shown. Fluorescence was highest with the line/box-1 probe. (c) Power spectra were calculated for the mean spectrum collected with each probe geometry. Higher frequency components corresponded to higher noise.

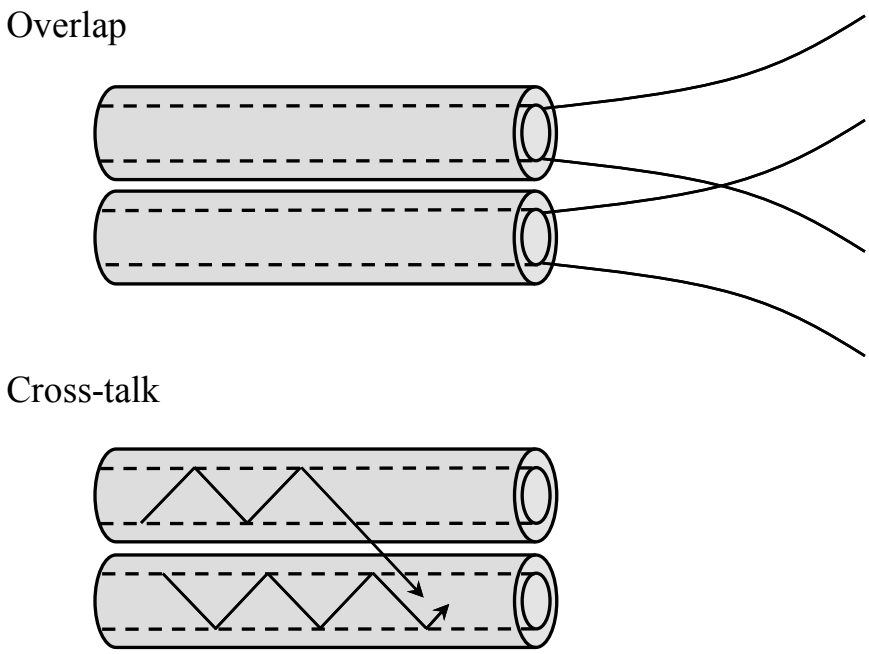

Figure 5.5. Fiber coupling. Both overlap and cross-talk cause signal mixing among fibers. Overlap occurs after light exits the fibers and is focused onto the detector. Cross-talk occurs between the fibers.

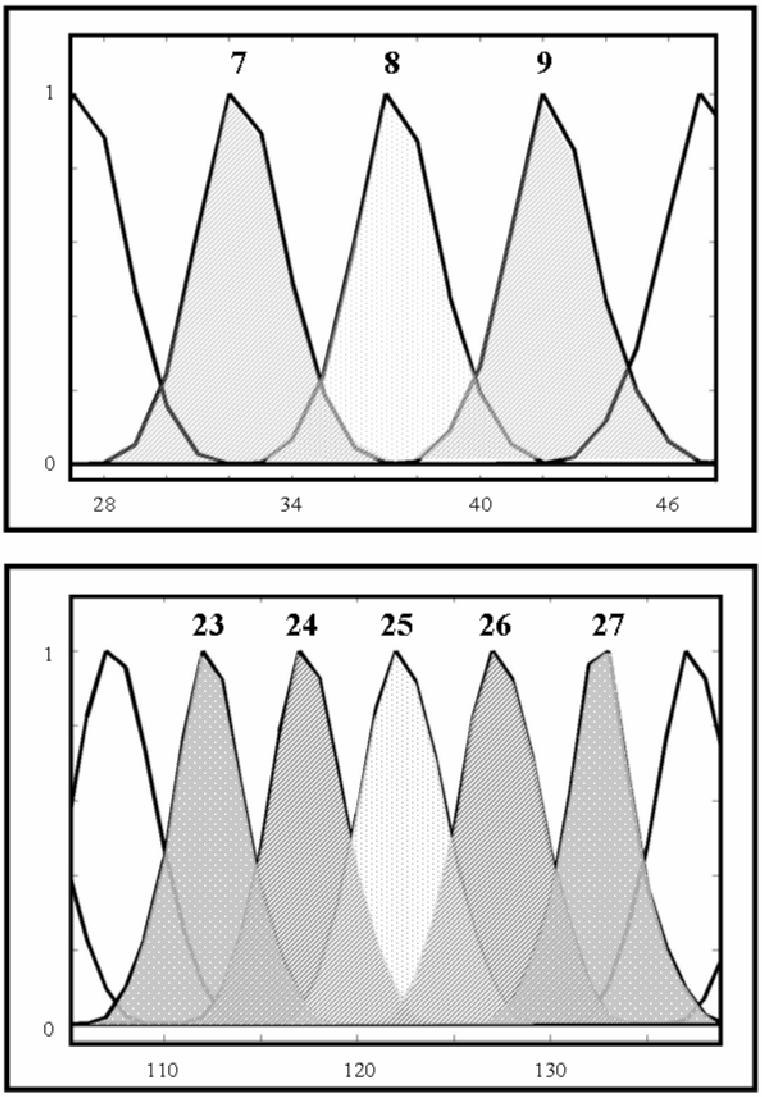

Figure 5.6. Extent of overlap. The profiles of individual fibers were measured. Both panels show the superposition of the fiber profiles and the extent of overlap for fibers 8 and 25, focused near the edge or the middle of the detector, respectively.

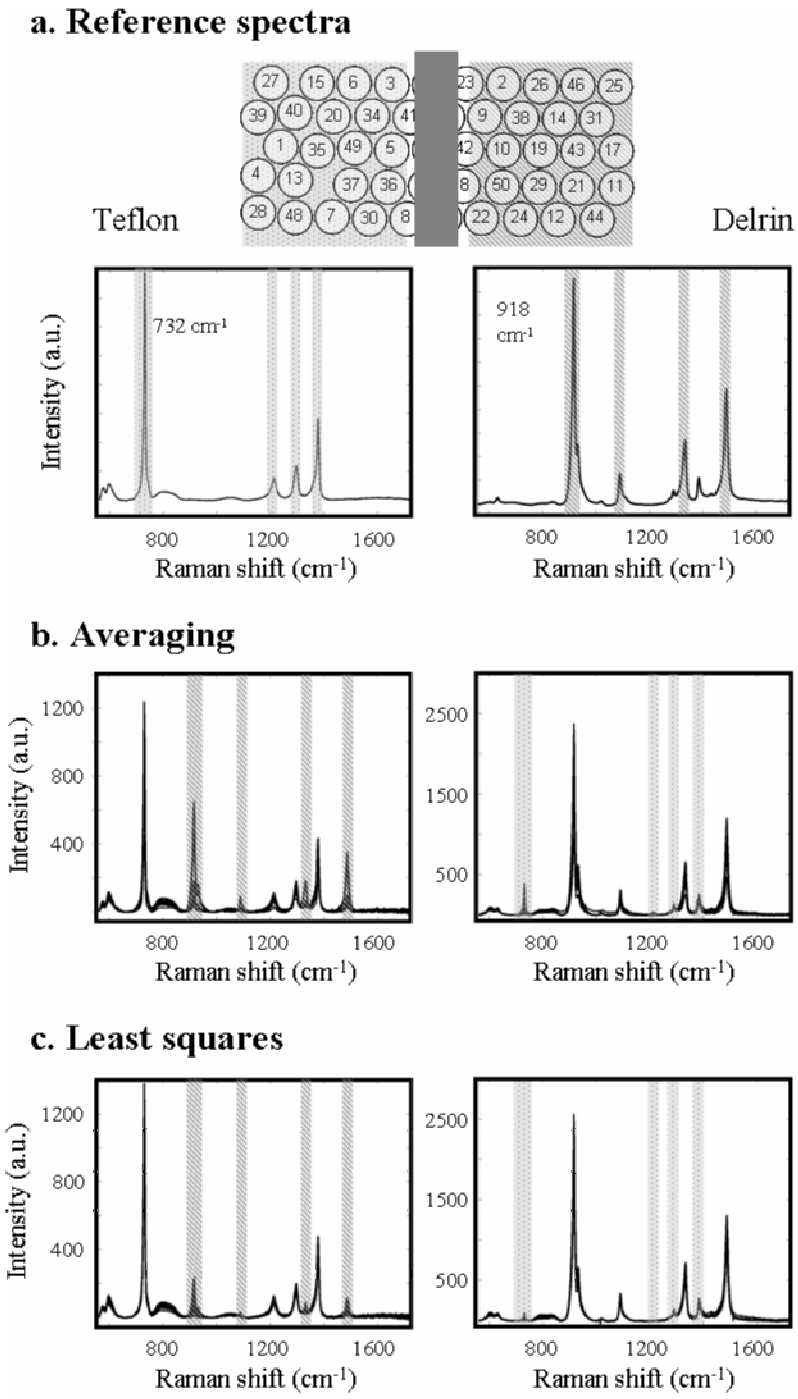

Figure 5.7. Method comparison. (a) The position of the 5x10 fiber array over the intersection of Teflon and Delrin is shown, along with reference Raman spectra for the two polymers. (b and c) Spectra from Teflon-interrogating and Delrin-interrogating fibers are plotted on the left and right, respectively, with bands from the contaminating polymer highlighted. In general, the least squares method increases the intensity of the desired polymer bands and decreases the intensity of the contaminating polymer bands.

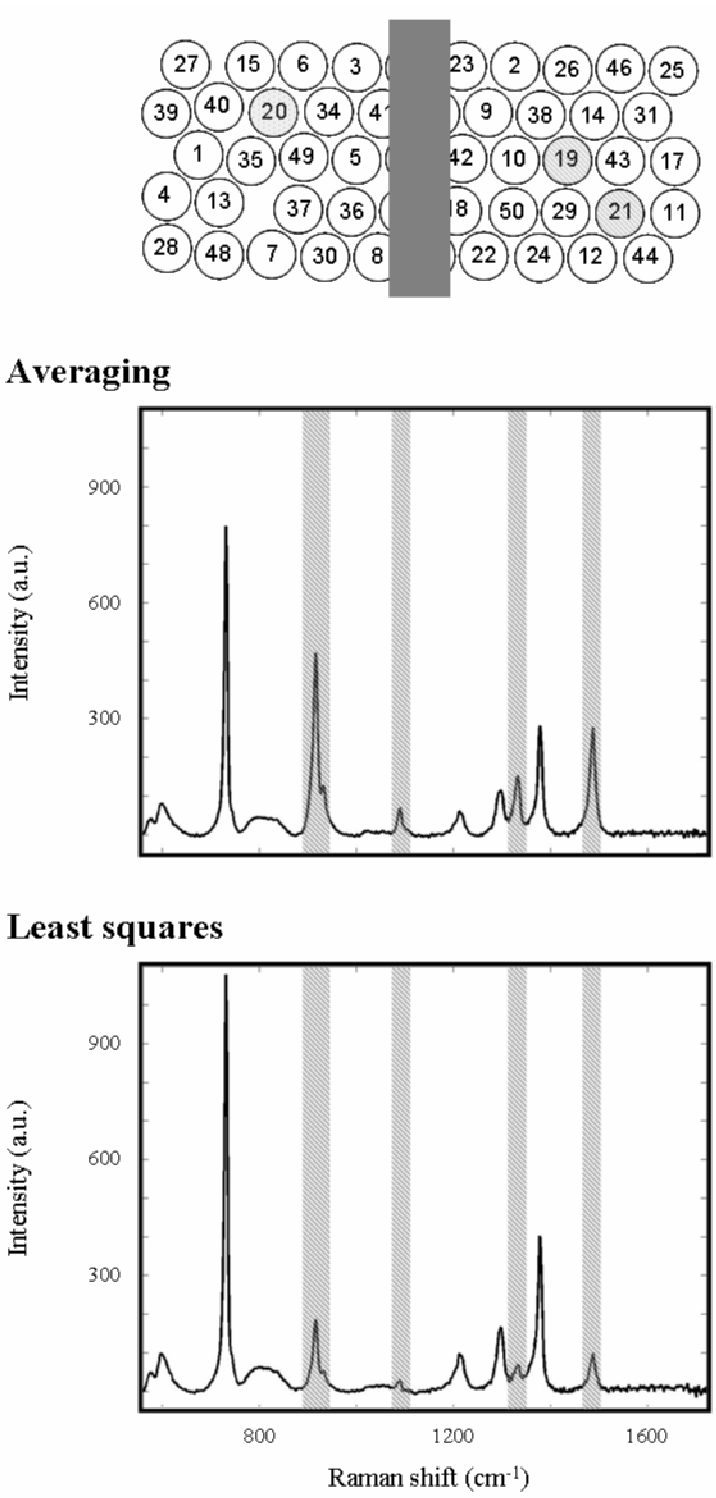

Figure 5.8. Teflon fiber 20. When compared to averaging, the least squares method increased the 732 cm^{-1} Teflon band from ~800 to 1080, and decreased the 918 cm^{-1} Delrin band from ~470 to 190.

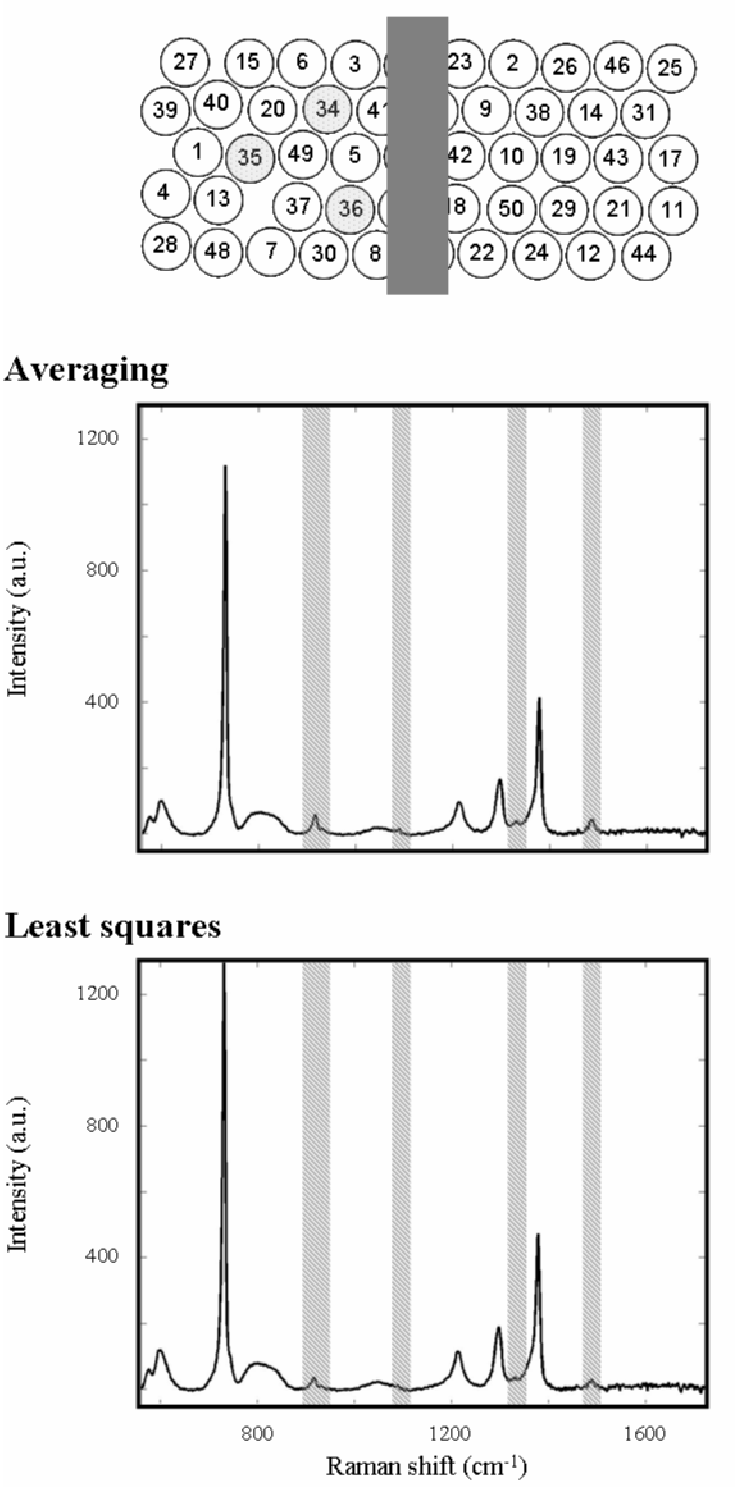

Figure 5.9. Teflon fiber 35. For minimal contamination, the least squares method still increased the 732 cm^{-1} Teflon band from ~1120 to 1300, and decreased the contaminating 918 cm^{-1} band from ~60 to 35.

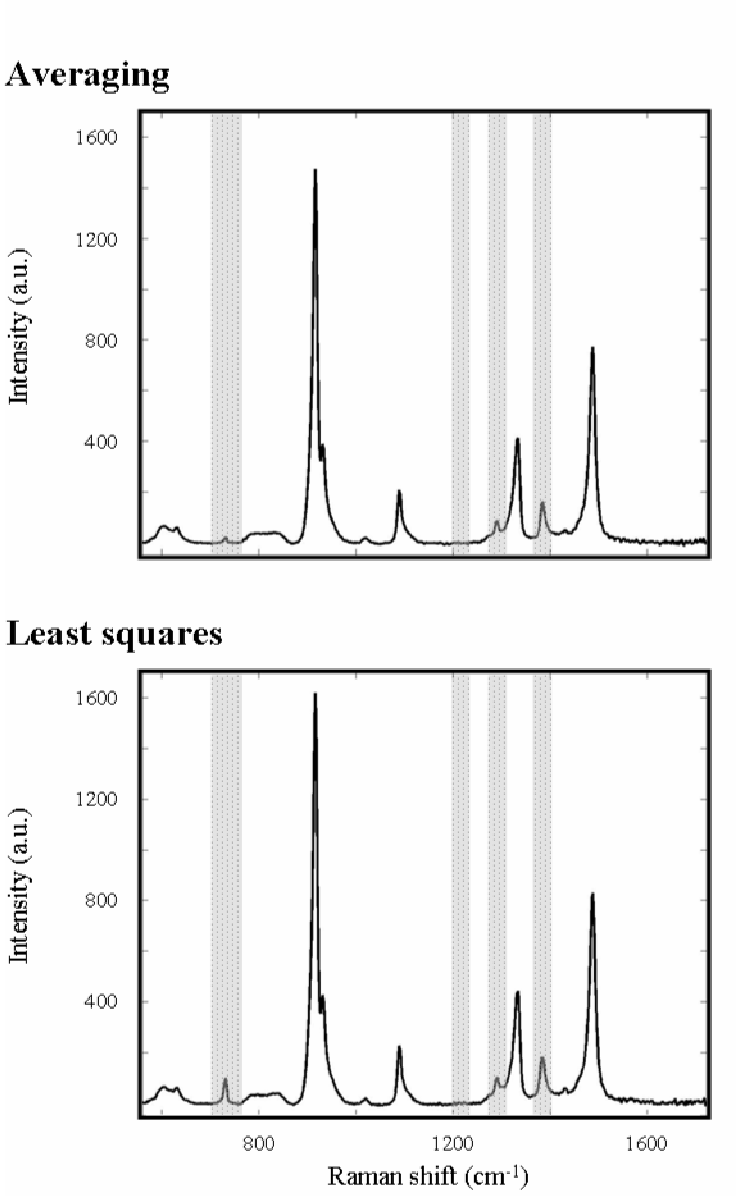

Figure 5.10. Least squares discrepancy. For four fibers, including Delrin fiber 26 shown above, the averaging method reduced contamination more than least squares. Least squares still increased the intensity of the major Delrin band from ~1470 to 1620, but also increased the intensity of the contaminating 732 cm^{-1} Teflon band from ~20 to 100.

References

1. N. Stone, R. Baker, K. Rogers, A. W. Parker, and P. Matousek, "Subsurface probing of calcifications with spatially offset Raman spectroscopy (SORS): Future possibilities for the diagnosis of breast cancer," *Analyst* **132**(9), 899-905 (2007).

2. P. Matousek and N. Stone, "Prospects for the diagnosis of breast cancer by noninvasive probing of calcifications using transmission Raman spectroscopy," *J. Biomed. Opt.* **12**(2), 024008 (2007).

3. M. V. Schulmerich, J. H. Cole, J. M. Kreider, F. Esmonde-White, K. A. Dooley, S. A. Goldstein, and M. D. Morris, "Transcutaneous Raman spectroscopy of murine bone in vivo," *Appl. Spectrosc.* **63**(3), 286-295 (2009).

4. A. M. K. Enejder, T. G. Scecina, J. Oh, M. Hunter, W.-C. Shih, S. Sasic, G. L. Horowitz, and M. S. Feld, "Raman spectroscopy for noninvasive glucose measurements," *J. Biomed. Opt.* **10**(3), 031114 (2005).

5. P. Matousek and A. W. Parker, "Bulk Raman analysis of pharmaceutical tablets," *Appl. Spectrosc.* **60**(12), 1353-1357 (2006).

6. C. Eliasson and P. Matousek, "Noninvasive authentication of pharmaceutical products through packaging using spatially offset Raman spectroscopy," *Anal. Chem.* **79**(4), 1696-1701 (2007).

7. P. Matousek, "Inverse spatially offset Raman spectroscopy for deep noninvasive probing of turbid media," *Appl. Spectrosc.* **60**(11), 1341-1347 (2006).

8. P. Matousek, "Deep non-invasive Raman spectroscopy of living tissue and powders," *Chem. Soc. Rev.* **36**(8), 1292-1304 (2007).

9. R. F. Bonner, R. Nossal, S. Havlin, and G. H. Weiss, "Model for photon migration in turbid biological media," *J. Opt. Soc. Am. A* **4**(3), 423-432 (1987).

10. N. Everall, T. Hahn, P. Matousek, A. W. Parker, and M. Towrie, "Photon migration in Raman spectroscopy," *Appl. Spectrosc.* **58**(5), 591-597 (2004).

11. T. Vo-Dinh, Ed., Biomedical Photonics Handbook, CRC Press, Boca Raton (2003).

12. R. R. Anderson and J. A. Parrish, "The optics of human skin," *J. Invest. Dermatol.* **77**(1), 13-19 (1981).

13. Z. Huang, H. Zeng, I. Hamzavi, A. Alajlan, E. Tan, D. I. McLean, and H. Lui, "Cutaneous melanin exhibiting fluorescence emission under near-infrared light excitation," *J. Biomed. Opt.* **11**(3), 034010 (2006).

14. D. Zhang, J. D. Hanna, Y. Jiang, and D. Ben-Amotz, "Influence of laser illumination geometry on the power distribution advantage," *Appl. Spectrosc.* **55**(1), 61-65 (2001).

15. U. Utzinger and R. R. Richards-Kortum, "Fiber optic probes for biomedical optical spectroscopy," *J. Biomed. Opt.* **8**(1), 121-147 (2003).

16. P. Matousek, I. P. Clark, E. R. C. Draper, M. D. Morris, A. E. Goodship, N. Everall, M. Towrie, W. F. Finney, and A. W. Parker, "Subsurface probing in diffusely scattering media using spatially offset Raman spectroscopy," *Appl. Spectrosc.* **59**(4), 393-400 (2005).

17. P. Matousek, M. D. Morris, N. Everall, I. P. Clark, M. Towrie, E. Draper, A. Goodship, and A. W. Parker, "Numerical simulations of subsurface probing in diffusely scattering media using spatially offset Raman spectroscopy," *Appl. Spectrosc.* **59**(12), 1485-1492 (2005).

18. M. V. Schulmerich, K. A. Dooley, M. D. Morris, T. M. Vanasse, and S. A. Goldstein, "Transcutaneous fiber optic Raman spectroscopy of bone using annular illumination and a circular array of collection fibers," *J. Biomed. Opt.* **11**(6), 060502 (2006).

19. M. V. Schulmerich, K. A. Dooley, T. M. Vanasse, S. A. Goldstein, and M. D. Morris, "Subsurface and transcutaneous Raman spectroscopy and mapping using concentric illumination rings and collection with a circular fiber-optic array," *Appl. Spectrosc.* **61**(7), 671-678 (2007).

20. V. V. Tuchin, *Optical Clearing of Tissues and Blood*, SPIE, Bellingham, WA (2006).

21. A. T. Yeh and J. Hirshburg, "Molecular interactions of exogenous chemical agents with collagen - implications for tissue optical clearing," *J. Biomed. Opt.* **11**(1), 014003 (2006).

22. C. A. Lieber and A. Mahadevan-Jansen, "Automated method for subtraction of fluorescence from biological Raman spectra," *Appl. Spectrosc.* **57**(11), 1363-1367 (2003).

23. W. Chew, E. Widjaja, and M. Garland, "Band-target entropy minimization (BTEM): An advanced method for recovering unknown pure component spectra. Application to the FTIR spectra of unstable organometallic mixtures," *Organometallics* **21**(9), 1982-1990 (2002).

24. E. Widjaja, C. Li, and M. Garland, "Semi-batch homogeneous catalytic in-situ spectroscopic data. FTIR spectral reconstructions using band-target entropy minimization (BTEM) without spectral preconditioning," *Organometallics* **21**(9), 1991-1997 (2002).

25. E. Widjaja, N. Crane, T. C. Chen, M. D. Morris, M. A. Ignelzi, and B. R. McCreadie, "Band-target entropy minimization (BTEM) applied to hyperspectral Raman image data," *Appl. Spectrosc.* **57**(11), 1353-1362 (2003).

26. B. R. McCreadie, M. D. Morris, T.-c. Chen, D. S. Rao, W. F. Finney, E. Widjaja, and S. A. Goldstein, "Bone tissue compositional differences in women with and without osteoporotic fracture," *Bone* **39**(6), 1190-1195 (2006).

27. T. J. Muldoon, M. C. Pierce, D. L. Nida, M. D. Williams, A. Gillenwater, and R. Richards-Kortum, "Subcellular-resolution molecular imaging within living tissue by fiber microendoscopy," *Opt. Express* **15**(25), 16413-16423 (2007).

28. M. J. Aernecke and D. R. Walt, "Optical-fiber arrays for vapor sensing," *Sensor. Actuat. B-Chem.* **142**(2), 464-469 (2009).

29. Y.-H. Liu, T. H. Dam, and P. Pantano, "A pH-sensitive nanotip array imaging sensor," *Anal. Chim. Acta* **419**(2), 215-225 (2000).

30. C. DiCesare, I. Biran, and D. Walt, "Individual cell migration analysis using fiber-optic bundles," *Anal. Bioanal. Chem.* **382**(1), 37-43 (2005).

31. Y. Lavi, A. Millo, and A. Katzir, "Thin ordered bundles of infrared-transmitting silver halide fibers," *Appl. Phys. Lett.* **87**(24), 241122-241123 (2005).

32. E. Rave and A. Katzir, "Ordered bundles of infrared transmitting silver halide fibers: attenuation, resolution and crosstalk in long and flexible bundles," *Opt. Eng.* **41**(7), 1467-1468 (2002).

33. M. E. Hankus, H. Li, G. J. Gibson, and B. M. Cullum, "Surface-enhanced Raman scattering-based nanoprobe for high-resolution, non-scanning chemical imaging," *Anal. Chem.* **78**(21), 7535-7546 (2006).

34. X. Chen, K. L. Reichenbach, and C. Xu, "Experimental and theoretical analysis of core-to-core coupling on fiber bundle imaging," *Opt. Express* **16**(26), 21598-21607 (2008).

35. J. Y. Ma and D. Ben-Amotz, "Rapid micro-Raman imaging using fiber-bundle image compression," *Appl. Spectrosc.* **51**(12), 1845-1848 (1997).

36. M. V. Schulmerich, W. F. Finney, R. A. Fredricks, and M. D. Morris, "Subsurface Raman spectroscopy and mapping using a globally illuminated non-confocal fiber-optic array probe in the presence of Raman photon migration," *Appl. Spectrosc.* **60**(2), 109-114 (2006).

37. L. Huang and U. Osterberg, "Measurement of cross talk in order-packed image fiber bundles," *Proc. SPIE* **2536**(1), 480-488 (1995).

38. D. Pysz, L. Kociszewski, and R. Stepien, "Technological aspects of fiber optic image guides for needle endoscopes manufacturing," *Proc. SPIE* **4158**(1), 137-143 (2001).

39. F. W. L. Esmonde-White, M. V. Schulmerich, K. A. Esmonde-White, and M. D. Morris, "Automated Raman spectral preprocessing of bone and other musculoskeletal tissues," *Proc. SPIE* **7166**(1), 716605 (2009).

40. A. Cao, A. K. Pandya, G. K. Serhatkulu, R. E. Weber, H. Dai, J. S. Thakur, V. M. Naik, R. Naik, G. W. Auner, R. Rabah, and D. C. Freeman, "A robust method for automated background subtraction of tissue fluorescence," *J. Raman Spectrosc.* **38**(9), 1199-1205 (2007).

41. S. Banerjee and D. Li, "Interpreting multicomponent infrared spectra by derivative minimization," *Appl. Spectrosc.* **45**(6), 1047-1049 (1991).

CHAPTER VI

CONCLUSIONS

Raman spectra can be recorded of bone tissue from different animal models, providing compositional and structural information about adaptations resulting from normal growth and development, mechanical stimuli, bone disorders, and pharmaceutical interventions. Raman spectroscopy is compatible with biological specimens because of its low sensitivity to water. The technique also provides a wealth of information because Raman bands are sensitive to composition of both the mineral and matrix phases of bone and to microstructure. In this dissertation, the majority of the work has focused on examining bone tissue from various animal models in order to further understanding about bone biomechanical function and normal bone development.

Raman imaging of equine bone was performed to map stress distribution in a model for the early stages of bone fracture and to map composition in a model for an extreme athlete, as described in chapter II. In the bone fracture model, residual stress in the loaded bone tissue was measured by analyzing band shifts in phosphate ν_1. These mineral band shifts were a consequence of changes in spacing between cations and anions of the mineral. Stresses were significantly higher in strained regions and locations near the edge of fracture than in control regions. Raman imaging enabled determination of the spatial variation of the stress. The pattern of stresses calculated from Raman

images was in agreement with the predicted stresses from a linear finite element analysis model of the fracture specimen. An interesting future study would be examination of the stress response of the matrix. In fractured regions, collagen cross-links are ruptured, but the fate of cross-links just before bone fails is not known, even though the rupture of cross-links is thought to be one of the last processes to occur before bone failure.

In the extreme athlete model, the third metacarpal bone from a racehorse was compared to that of a nonathletic horse. The third metacarpal bone was used because it is a common site of fracture in racehorses because of their high activity levels. The mineral-to-matrix ratio, an indicator of tissue mineralization, was increased in the racehorse specimen, suggesting that the addition of more mineral may be an adaptive mechanism that allows the bone to perform under the large loads it experiences.

In chapters III and IV, Raman spectroscopy of the long bones from genetically-modified mice was used to study normal bone development and the disease osteogenesis imperfecta, respectively. The Sprouty2 (Spry2) gene influences the development of many types of tissues, including bone. We investigated how the Spry2 gene affects bone composition in normal bone development by examining the cross-section of tibiae from Spry2 knock-out mice ($Spry2^{-/-}$) and wild-type mice using Raman spectroscopy. A significantly lower collagen cross-link ratio was found in $Spry2^{-/-}$ specimens, suggesting that cross-linking is occurring earlier in those specimens. The mineral-to-matrix ratio (when calculated with phosphate ν_2 or phosphate ν_4 as the mineral component) was also lower in the knock-out mice. Based on the observed differences in band ratios, Spry2 appears to regulate cross-link formation and accrual of mineral during normal bone development. Orientation effects in phosphate ν_1 were also

seen in this study. Phosphate ν_1 band intensity depends on composition and orientation of the mineral, and mineral orientation is more variable across the cross-section of a tibia. In this experiment, the orientation effects confounded trends in the mineral-to-matrix ratios calculated using three different phosphate bands as the mineral component. However, this property can also be exploited to obtain information about the molecular orientation of components, as was done in the study on Brittle (Brtl) mice.

Chapter IV described studies on the $Brtl^{+/-}$ mouse, a knock-in model for osteogenesis imperfecta. In this model, an amino acid point substitution in one of the α1(I) chains of the collagen molecule prevents proper folding of the collagen triple helix. Polarized Raman spectroscopy was used to assess the relative molecular orientations of bone mineral and collagen fibrils in $Brtl^{+/-}$ and wild-type mice. Although no changes in the degree of alignment of mineral and collagen fibrils between genotypes was detected, it is known that the folding of the triple helix is disrupted in Brtl mice. Local, but not overall, systematic disruptions to the triple-helical folding of collagen may be present, but the spatial resolution of our Raman system may not be high enough to detect small perturbations.

Finally, research utilizing fiber-based Raman systems was addressed in chapter V. Improvements to ex vivo, through-the-skin bone measurements on animal tissue were presented, including accurate recovery of mineral band height ratios through thick overlying tissue layers and the introduction of a probe geometry to reduce fluorescence and noise in measurements of murine tissue. Also, improvements to individual fiber spectra through the implementation of software corrections for fiber coupling errors and signal mixing were demonstrated in a polymer test system. Mathematical correction for

fiber coupling enables the use of a tightly-packed fiber bundle, thus overcoming the fiber spacing/signal mixing trade-off. Continual improvements in probe design, including different illumination/collection geometries, and the move towards tomographic measurements, where illumination and collection fibers are placed directly on the skin, will lead to more accurate measurements of bone tissue through the skin. With these advances, accurate transcutaneous measurements of the bone matrix, rather than just the bone mineral, may be possible.

In summary, Raman spectroscopy is a versatile technique for studying multiple aspects of bone health. Raman bands are sensitive to the composition and structural orientation of the material and to external mechanical forces. The applications described in this dissertation demonstrate the utility of Raman spectroscopy for advancing knowledge of bone development and biomechanical function: Raman spectroscopy has been used to map stress distribution in a model for the early stages of bone fracture, map composition in an extreme athlete model, evaluate composition in a murine model for normal bone development, and determine the relative orientation of mineral and collagen components in a murine model for osteogenesis imperfecta. In addition, an improved methodology for recovering spectra collected with fiber-optic arrays was demonstrated. The technique allows use of tightly-packed arrays with minimal signal mixing among fibers.

APPENDIX I

MATLAB PROCESSING CODE

%This is the typical Matlab code used to preprocess the data and work up calibrations, baseline, and then save the data as a .prn file to be imported into GRAMS for peak fitting.

```
%%%%%%%%%%%%%%%%%%%%
%LOAD DATA AND CALIBRATION FILES

%load data
filenames=dir('*.asc');
j=0;
for i=1:numel(filenames);
   if any([strfind(filenames(i).name,'idxxx_60s')]) %select all datafiles whose name
      %contains 'idxxx_60s' and load into one 3-dimensional matrix called 'data'
      tmp=francisandor(filenames(i).name);
      if ndims(tmp)>2
        k=j+size(tmp,1);
        j=j+1;
      else
```

```
        j=j+1;
        k=j;
      end
      data(j:k,:,:)=tmp;
      for iter=j:k;
        origin(iter).name=filenames(i).name;
      end
      j=k;
    end
end
clear filenames i iter j k tmp
disp('variable "data" contains:');
for i=1:numel(origin); disp(origin(i).name); end %origin.name contains the names of the
%individual datafiles contained within the 3-dimensional matrix 'data'

%load calibration files
neon= francisandor('neon_3s_20x75na_25umslit.asc');
darkn = francisandor('dark_3s_20x75na_25umslit.asc');
teflon = francisandor('teflon_60s_20x75na_25umslit.asc');
darktef = francisandor('dark_60s_20x75na_25umslit.asc');
wdc = francisandor('white_10s_20x75na_25umslit.asc');
darkw = francisandor('dark_10s_20x75na_25umslit.asc');
dark = francisandor('dark_300s_20x75na_25umslit.asc'); %'dark' is for data
```

```
save raw_data



%%%%%%%%%%%%%%%%%%%%
%UNSPIKE DATA AND CALIBRATION FILES

load raw_data
visispike('data')
visispike('dark') %etc.



%%%%%%%%%%%%%%%%%%%%
%CALIBRATION PREPROCESSING
%Apply the image transforms to all the calibration data

disp('Loading TFORM.');
[filename, pathname] = uigetfile( {'*.mat';'*.*'}, 'Select most recent TFORM
(1:1024,1:128).', 'MultiSelect', 'off');
load([pathname,filename],'TFORM')

%DEAL WITH NEON
disp('Apply the image transform to all the calibration data (neon, teflon, white)');
```

```
coefficient=max(wdc(:)-darkw(:));
neon = (neon-darkn).*(coefficient.*((wdc-darkw)));
%multiplying by coef takes care of efficiency of camera vs. wavelength, only multiply
%by coef *before* NIST Intensity Correction
neon = imtransform(neon.',TFORM,'bilinear','FillValues',NaN);

%find the transform boundaries and remove the edges
RemoveBounds=true;
FirstRow=1;
LastRow=size(neon,1);
FirstColumn=1;
LastColumn=size(neon,2);
while RemoveBounds
   RemoveBounds=false;
   %check if the first row should be removed
   if sum(isnan(neon(1,:)))>sum(isnan(neon(2,:)))
       FirstRow=FirstRow+1;
       neon=neon(2:end,:);
       RemoveBounds=true;
   end
   %check if the last row should be removed
   if sum(isnan(neon(end,:)))>sum(isnan(neon(end-1,:)))
       LastRow=LastRow-1;
```

```
        neon=neon(1:(end-1),:);
        RemoveBounds=true;
    end
    %check if the first column should be removed
    if sum(isnan(neon(:,1)))>sum(isnan(neon(:,2)))
        FirstColumn=FirstColumn+1;
        neon=neon(:,2:end);
        RemoveBounds=true;
    end
    %check if the last column should be removed
    if sum(isnan(neon(:,end)))>sum(isnan(neon(:,end-1)))
        LastColumn=LastColumn-1;
        neon=neon(:,1:(end-1));
        RemoveBounds=true;
    end
end


ne = sum(neon(20:110,:));
%find the neon peaks
[maxy,maxi] = findmaxima(ne);
%load the known wavelength values
cal_vector = xlsread('C:\MATLAB7\toolbox\morris lab\kate\red1\red1_excel_calibration.
xls');
```

```
%split the loaded values into wavelengths and pixels
wavelen = cal_vector(1,:);
est_pix = cal_vector(2,:);
wavelen(est_pix<5)=[];
est_pix(est_pix<5)=[];
%find the closest pixels
for i=1:numel(est_pix);
   [y,j] = min(abs(est_pix(i)-maxi));
   known_pix(i) = maxi(j);
end
%calculate the rshift coefficients
coef = wavelen/[known_pix.^3;known_pix.^2;known_pix;ones(size(known_pix))];

%DEAL WITH TEFLON
teflon = (teflon-darktef).*(coefficient.*((wdc-darkw)));
teflon = imtransform(teflon.',TFORM,'bilinear','FillValues',NaN);
teflon = teflon(FirstRow:LastRow,FirstColumn:LastColumn);
tef = sum(teflon(20:110,:));
%initial laser wavelength estimate
laser_wl=784.79;
%iteratively find a better laser wavelength
cm=rshift(1:size(neon,2),[coef],laser_wl);
[interp_data,interp_axis]=FEW_interpolate(tef,cm,50);
```

```
%[y,i]=max(interp_data); %only use on sub-images where laser portion of spectrum has
%been truncated out
%pos=interp_axis(i);
[y,i]=max(interp_data(14000:20000)); %use on full resolution images to choose teflon
%732 cm^-1 band over intense laser band
pos=interp_axis(13999+i);
oldl=nan;
while abs(pos-732)>0.01
    grandl=oldl;
    oldl=laser_wl;
    if (pos<732)
        %make laser wl bigger
        laser_wl = laser_wl - 0.005;
    else
        %make laser wl smaller
        laser_wl = laser_wl + 0.005;
    end
    if (grandl==laser_wl) %it is jittering around the same point.
        break;
    end
    %iteratively find a better laser wavelength
    cm=rshift(1:size(neon,2),[coef],laser_wl);
    [interp_data,interp_axis]=FEW_interpolate(tef,cm,50);
```

```
    %[y,i]=max(interp_data);
    %pos=interp_axis(i);
    [y,i]=max(interp_data(14000:20000));
    pos=interp_axis(13999+i);
end


wavenumber_axis = cm;


%DEAL WITH INTENSITY CALIBRATION
whitespec = (wdc-darkw);
whitespec = imtransform(whitespec.',TFORM,'bilinear','FillValues',NaN);
whitespec = whitespec(FirstRow:LastRow,FirstColumn:LastColumn);


%NIST Intensity Calibration Section
%Select which HCA was used:
cal_axis=dlmread('C:\Kate\HCACals\HCARed1\090520AI.prn');
%cal_axis=dlmread('C:\Kate\HCACals\HCARed4\080926AI.PRN');
WavelengthAxis=polyval(coef,1:length(ne));
NISTWhite=spline(cal_axis(:,1),cal_axis(:,2),WavelengthAxis);
IntensityCalibration=zeros(size(whitespec));
for spatialdim=1:size(whitespec,1)
   IntensityCalibration(spatialdim,:)=whitespec(spatialdim,:)./NISTWhite;
```

```
  IntensityCalibration(spatialdim,:)=IntensityCalibration(spatialdim,:)/max(IntensityCali
  bration(spatialdim,:));
end

%DEAL WITH DATA
dat=nan(size(data,1),size(whitespec,2),size(whitespec,1));
%for each frame in the data images, do the following:
for i=1:size(data,1);
   dat_tmp = (squeeze(data(i,:,:))-dark);
   dat_tmp2 = imtransform(dat_tmp.',TFORM,'bilinear','FillValues',NaN);
   dat_tmp2 = dat_tmp2(FirstRow:LastRow,FirstColumn:LastColumn);
   dat(i,:,:)=dat_tmp2.'./IntensityCalibration.';
end

save samplecal.mat wavenumber_axis cm coef laser_wl pos neon teflon whitespec
IntensityCalibration dark TFORM
save cm.mat cm
save preprocessed_data.mat dat %dat is 3-dimensional if more than one datafile was
%loaded



%%%%%%%%%%%%%%%%%%%%
%BASELINING
```

```
%baselining procedure is based on following journal article:
%A. Cao, et al, "A robust method for automated background subtraction of tissue
%fluorescence," J. Raman Spectrosc 38, 1199-1205 (2007).

load preprocessed_data
%select active region of CCD
truncdat = dat(:,100:813,10:120); %100:813 is spectral dimension; 10:120 is spatial
%dimension
truncdat = shiftdim(truncdat,1);
for i = 1:size(truncdat,3) %size(truncdat,3) is equal to number of transects
   bsln_data(:,:,i)=BGminmax(truncdat(:,:,i),3);
end
save baselined_data.mat bsln_data



%%%%%%%%%%%%%%%%%%%%
%SAVING .PRN FILES TO IMPORT INTO GRAMS

load cm
load baselined_data
load raw_data origin
origin.name %retrieve names of individual datafiles
```

```
%save transects in baselined data as individual datafiles;
%idxxx_60s_location1 = bsln_data(:,:,1); idxxx_60s_location2 = bsln_data(:,:,2); etc.
b = [cm.', datafile.'];
csvwrite('grams_datafile.prn', b);

%Import into GRAMS using ASCIIXYS non-even X spacing.  This step converts
%the .prn datafiles into .spc files.  Open the files in GRAMS.
```

APPENDIX II

MATLAB CODE FOR 3-D PLOTS

% For the images presented in Chapter II, where the laser line was stepped across the x-axis, and the y-axis of the images corresponded with the length of the laser line.

```
load filename
xvals = 0:3.125:500;      %3.125 is step size in μm; 500 is size of image (along x-axis) in
%μm
xvals = xvals(1:160);     %160 is # of steps (i.e. 3.125 x 160 = 500 μm)
yarray = repmat([1:98]',1,160);     %98 is the # of pixels in the spatial dimension
xarray = repmat(xvals, [98,1]);
surf(xarray, yarray, filename);     %creates a surface mesh
view(0,90)     %sets view from above
shading interp     %interpolating between values
set(gca,'PlotBoxAspectRatio', [x y z]);     %scale x- and y- dimensions among all images,
%where x and y are scaled from 0 to 1 and z = 1
set(gca, 'YTick', [fill in #s], 'YTickLabel', [fill in #s]);     %allows y-axis to be labeled in
%μm rather than pixels; YTick is pixel value and YTickLabel is value in μm
```

%caxis command scales colorbar for image (i.e. caxis([10 60]) scales image from values %10 to 60)

%once images are plotted and scaled, in the Matlab figure window: File→ Export Setup %→ set width and height of image manually and then export image

APPENDIX III

LIST OF PUBLICATIONS

[1] K. A. Dooley, F. W. L. Esmonde-White, M. D. Morris, "Mathematical correction for coupling errors in fiber optic spectroscopy," *In preparation*.

[2] K. A. Dooley, F. W. L. Esmonde-White, M. D. Morris, "Optical fiber bundle coupling errors in Raman spectra: correction via data processing," *Proc. SPIE* **7560**, 75600O (2010).

[3] K. A. Dooley, J. McCormack, D. P. Fyhrie, M. D. Morris, "Stress mapping of undamaged, strained, and failed regions of bone using Raman spectroscopy," *J. Biomed. Opt.* **14**(4), 044018 (2009).

[4] M. D. Morris, M. V. Schulmerich, K. A. Dooley, K. A. Esmonde-White, "Vibrational Spectroscopic Imaging of Hard Tissue," *Infrared and Raman Spectroscopic Imaging*. Eds. Salzer and Siesler. Weinheim: WILEY-VCH, 149-171 (2009).

[5] M. V. Schulmerich, J. H. Cole, J. M. Kreider, F. Esmonde-White, K. A. Dooley, S. A. Goldstein, M. D. Morris, "Transcutaneous Raman spectroscopy of murine bone *in vivo*," *Appl. Spectrosc.* **63**(3), 286-295 (2009).

[6] S. Srinivasan, M. V. Schulmerich, J. H. Cole, K. A. Dooley, J. M. Kreider, B. W. Pogue, M. D. Morris, S. A. Goldstein, "Image-guided Raman spectroscopic recovery of canine cortical bone contrast *in situ*," *Opt. Express.* **16**(16), 12190 (2008).

[7] M. V. Schulmerich, J. H. Cole, K. A. Dooley, M. D. Morris, J. M. Kreider, S. A. Goldstein, S. Srinivasan, B. W. Pogue, "Noninvasive Raman tomographic imaging of canine bone tissue," *J. Biomed. Opt.* **13**(2), 020506 (2008).

[8] M. V. Schulmerich, J. H. Cole, K. A. Dooley, J. M. Kreider, S. A. Goldstein, M. D. Morris, "Optical clearing in transcutaneous Raman spectroscopy of murine cortical bone tissue," *J. Biomed. Opt.* **13**(2), 021108 (2008).

[9] K. A. Dooley, J. McCormack, D. P. Fyhrie, M. D. Morris, "Compositional differences among undamaged, strained, and failed regions of bone using Raman spectroscopy," *Proc. SPIE* **6853**, 68530Z (2008).

[10] M. V. Schulmerich, K. A. Dooley, T. M. Vanasse, S. A. Goldstein, M. D. Morris, "Subsurface and transcutaneous Raman spectroscopy and mapping using concentric illumination rings and collection with a circular fiber-optic array," *Appl. Spectrosc.* **61**(7), 671-678 (2007).

[11] M. V. Schulmerich, K. A. Dooley, T. M. Vanasse, S. A. Goldstein, M. D. Morris, "Transcutaneous fiber optic Raman spectroscopy of bone using annular illumination and a circular array of collection fibers," *J. Biomed. Opt.* **11**(6), 060502 (2006).